Threshold Switching and Self-Oscillation in Niobium Oxide

Shuai Li

A thesis submitted for the degree of
Doctor of Philosophy of
The Australian National University

May, 2018

To my loved ones…

Declaration

This thesis contains no material which has been accepted for the award of any other degree or diploma in any university. To the best of the author's knowledge, it contains no material previously published or written by another person, except where due reference is made in the text.

Shuai Li

30 May 2018

Acknowledgements

First and foremost, my sincere gratitude goes to the members of my supervisory panel. I would like to thank the panel chair Prof. Robert Elliman for offering me this PhD opportunity and his continuous support. I am grateful for his passion, encouragement, patience and guidance throughout the journey. I appreciate the freedom that he offered me in exploring a diverse range of topics while ensuring the overall research stayed focused to form this coherent thesis. I want to express my appreciation to A/Prof. Xinjun Liu for many stimulating discussions, new ideas and insightful suggestions on experiments and modelling. I would like to thank Dr. Dinesh Kumar Venkatachalam for his assistance and valuable input into my research.

My appreciation is extended to my fellow colleagues at Department of Electronic Materials Engineering (EME) for providing a supportive and collaborative research environment. I would like to give my thanks to Dr. Sanjoy Kumar Nandi for helping me develop skills on device fabrication, Dr. Kidane Belay and David Llewellyn for assisting me in preparing TEM samples and Dr. Felipe Kremer for providing his time and expertise in TEM characterisation. I appreciate the valuable advice from Prof. Hoe Tan, Prof. Mark Ridgway and Emeritus Prof. Neville Fletcher. I want to acknowledge the technical staff, Chris Kafer, Dane Kelly and Joshua Carr, for their help and the administrative staff, Julie Arnold, Liudmila Mangos and Karen Nulty for their support. I also want to sincerely thank EME graduate students, especially Pablo, Dipankar, James and Shimul for their help and friendship.

I thank the staff members of Australian National Fabrication Facility, Dr. Fouad Karouta, Dr. Kaushal Vora, Dr. Naeem Shahid, Dr. Li Li and Dr. Mark Lockrey, for their assistance in using the research equipment and valu-

able discussions. Moreover, I would like to extend my thanks to the staff members of the Electronics Unit, especially Dennis Gibson, David Anderson, Daniel Tempra and Paul Redman, for their help in developing electrical equipments and useful discussions.

I'd like to acknowledge the financial support of the Research Training Program Fee-Offset Scholarship from the Australian Government and the Postgraduate Research Scholarship from the Australian National University. Research work and travel during my studies were made possible by funding from the Australian Research Council and National Research Infrastructure for Australia.

Finally, I would like to give my deepest gratitude to my family and friends for their love, sacrifice and support. Words cannot express how grateful I am.

Publications

Refereed Journal Articles

The following articles contain results included in this thesis. # notes for equal contribution to the work.

1. S. K. Nandi#, **S. Li**#, X. Liu, D. K. Venkatachalam, R. G. Elliman,"Temperature dependent frequency tuning of NbO_x relaxation oscillators", Applied Physics Letters **111**, 202901 (2017).

2. **S. Li**, X. Liu, S. K. Nandi, D. K. Venkatachalam, R. G. Elliman, "Coupling dynamics of Nb/Nb_2O_5 relaxation oscillators", Nanotechnology **28**, 125201 (2017).

3. X. Liu, **S. Li**, S. K. Nandi, D. K. Venkatachalam, R. G. Elliman, "Threshold switching and electrical self-oscillation in niobium oxide films", Journal of Applied Physics **120**, 124102 (2016).

4. **S. Li**, X. Liu, S. K. Nandi, D. K. Venkatachalam, R. G. Elliman, "High-endurance megahertz electrical self-oscillation in Ti/NbO_x bilayer structures", Applied Physics Letters **106**, 212902 (2015).

Unpublished Article

1. **S. Li**, X. Liu, S. K. Nandi, D. K. Venkatachalam, R. G. Elliman, "Anatomy of filamentary threshold switching in amorphous niobium oxide", finalised for publication.

Conference Proceedings

1. **S. Li**, X. Liu, S. K. Nandi, D. K. Venkatachalam, R. G. Elliman, "Temperature dependence of threshold switching in NbO_x thin films", Conference on Optoelectronic and Microelectronic Materials and Devices 138-140 (2014).

2. X. Liu, S. K. Nandi, D. K. Venkatachalam, **S. Li**, K. Belay, R. G. Elliman, "Finite element modeling of resistive switching in Nb_2O_5-based memory device", Conference on Optoelectronic and Microelectronic Materials and Devices 280-283 (2014).

3. S. K. Nandi, X. Liu, **S. Li**, D. K. Venkatachalam, K. Belay, R. G. Elliman, "Resistive switching behavior in HfO_2 with Nb as an oxygen exchange layer", Conference on Optoelectronic and Microelectronic Materials and Devices 290-294 (2014).

Abstract

Volatile threshold switching, or current controlled negative differential resistance (CC-NDR), has been observed in a range of transition metal oxides. Threshold switching devices exhibit a large non-linear change in electrical conductivity, switching from an insulating to a metallic state under external stimuli. Compact, scalable and low power threshold switching devices are of significant interest for use in existing and emerging technologies, including as a selector element in high-density memory arrays and as solid-state oscillators for hardware-based neuromorphic computing.

This thesis explores the threshold switching in amorphous NbO_x and the properties of individual and coupled oscillators based on this response. The study begins with an investigation of threshold switching in Pt/NbO_x/TiN devices as a function device area, NbO_x film thickness and temperature, which provides important insight into the structure of the self-assembled switching region. The devices exhibit combined threshold-memory behaviour after an initial voltage-controlled forming process, but exhibit symmetric threshold switching when the RESET and SET currents are kept below a critical value. In this mode, the threshold and hold voltages are shown to be independent of the device area and film thickness, and the threshold power, while independent of device area, is shown to decrease with increasing film thickness. These results are shown to be consistent with a structure in which the threshold switching volume is confined, both laterally and vertically, to the region between the residual memory filament and the electrode, and where the memory filament has a core-shell structure comprising a metallic core and a semiconducting shell. The veracity of this structure is demonstrated by comparing experimental results with the predictions of a resistor network model, and detailed finite element

simulations.

The next study focuses on electrical self-oscillation of an NbO_x threshold switching device incorporated into a Pearson-Anson circuit configuration. Measurements confirm stable operation of the oscillator at source voltages as low as 1.06 V, and demonstrate frequency control in the range from 2.5 to 20.5 MHz with maximum frequency tuning range of 18 MHz/V. The oscillator exhibit three distinct oscillation regimes: sporadic spiking, stable oscillation and damped oscillation. The oscillation frequency, peak-to-peak amplitude and frequency are shown to be temperature and voltage dependent with stable oscillation achieved for temperatures up to $\sim$380 K. A physics-based threshold switching model with inclusion of device and circuit parameters is shown to explain the oscillation waveform and characteristic.

The final study explores the oscillation dynamics of capacitively coupled Nb/Nb_2O_5 relaxation oscillators. The coupled system exhibits rich collective behaviour, from weak coupling to synchronisation, depending on the negative differential resistance response of the individual devices, the operating voltage and the coupling capacitance. These coupled oscillators are shown to exhibit stable frequency and phase locking states at source voltages as low as 2.2 V with MHz frequency tunable range. The numerical simulation of the coupled system highlights the role of source voltage, and circuit and device capacitance in controlling the coupling modes and dynamics.

Contents

Chapter 1

Motivation and Outline

1.1 Motivation

Conventional digital computing is fundamentally based on the von Neumann architecture which requires a basic sequential cycle of fetching instructions from memory, decoding instructions, executing instructions and storing results. Despite rapid progress in improving computing speed and processing complexity, the most advanced supercomputer is still unable to compete on the same level of adaptability, error-tolerance, space and power efficiency as the brain. This has been demonstrated by IBM using the Blue Gene supercomputer to simulate the cortical activity if a cat's brain. Even when the cortical activity was simulated with neuron firing rate 100 times slower than real time, it still required 147, 456 processors, 144 TB of memory and 1.4 MW power to perform the task [1]. In contrast, the human brain, which has higher biological complexity than the cat brain, uses only 20 W of power. That is, for massively parallel computing, the human brain is over six orders of magnitude more energy efficient than the Blue Gene supercomputer [2].

The configuration of the biological brain is fundamentally different from the von Neumann architecture where neurons are interconnected via synapses to form highly complex and parallel three dimensional neural networks [2]. Therefore, there has been growing research interest in developing alternative brain-inspired computing architectures. Solid-state neural networks are particularly suitable for application in a complex real-world environment, such as spatio-temporal recognition and processing video data, where inputs and outputs are not clearly defined.

Within the central nervous system, a typical neuron comprises three main parts: a soma, dendrites and an axon [2]. Each neuron receives input signals from other neurons and electrical spikes (action potential) is generated by the soma if the sum of the integrated stimuli exceeds a certain threshold value. The generated spikes travel down the axon and activate the synaptic terminals to transmit electrical or chemical signals to other neurons. The connectivity of biological neural networks is complex as one neuron has 10^3 to 10^4 synapses that interconnect with other neurons [3]. The effectiveness of communication among neurons depends on the synaptic strength. The ability of synapses to modify their connection strength is known as synaptic plasticity which is considered to be the principal mechanism responsible for learning and memory [4]. Spike-timing dependent plasticity (STDP) is an asymmetric form of synaptic modification where the connection strength is enhanced or depressed by the order and precise temporal difference between the pre- and postsynaptic spikes [5]. The synaptic connection is strengthened when the presynaptic cell repeatedly fires spikes before the postsynaptic spikes. This phenomenon is known as long-term potentiation (LTP). The opposite of LTP is long-term depression (LTD) where synaptic efficacy is weakened due to arrival of presynaptic input after postsynaptic spikes [2].

Recently, two-terminal non-volatile resistive switching devices have been proposed to mimic important synaptic functions such as STDP. An artificial synaptic device based on ReRAM can emulate the strengthening and weakening behaviour between pre- and postsynaptic cells by continuous modification of device resistance states with electrical stimuli due to their dynamic switching characteristics [6,7]. Synaptic devices based on binary oxides, including NbO_x, HfO_x, WO_x, AlO_x and TiO_x, have been reported [8–12]. Individual two-terminal synaptic devices can be implemented in an integrated synapse-neuron circuit with a crossbar structure to achieve high connectivity and density. Such hybrid artificial neural networks have demonstrated robust tolerance to synaptic device variation and adaptive learning capability in both experimental realisation and simulation [13, 14].

An action potential pulse is initiated due to significant conductance modulation of voltage-gated sodium and potassium ion channels when a neuron cell body is sufficiently stimulated by the summation of inputs from other neurons [2, 15]. The neuron spike is considered to be a fundamental means of communication in the central nervous system. The generation and propagation of action potentials is captured in the Hodgkin-Huxley model which describes conductance of these two channels by a set of four nonlinear differential equations with four state variables [16]. The concept of a neuristor was proposed in 1960 to emulate the biological neural functions of the Hodgkin-Huxley model using hardware [17].

A recent study by Pickett et al. experimentally demonstrated a highly scalable solid-state neuristor based on two locally-active NbO_x memristors that exhibited threshold switching behaviour [18]. The studied neuristor circuit, as shown in Fig. 1.1(c), includes two distinct memristors with a parallel capacitor for each device which are mathematically equivalent to the two ion channels of the Hodgkin-Huxley axon circuit model from a circuit-theoretic perspective [19]. The theoretical study by Chua introduced the local activity principle, which can explain the ability of a nonlinear dynamical system to amplify signal fluctuations [21, 23]. Local acitvity forms a fundamental basis for emergence of complex phenomena. In the Hodgkin-Huxley model, the emergence of the nonlinear behaviour of action potential is associated with the edge of chaos, which serves as a small subset of the local

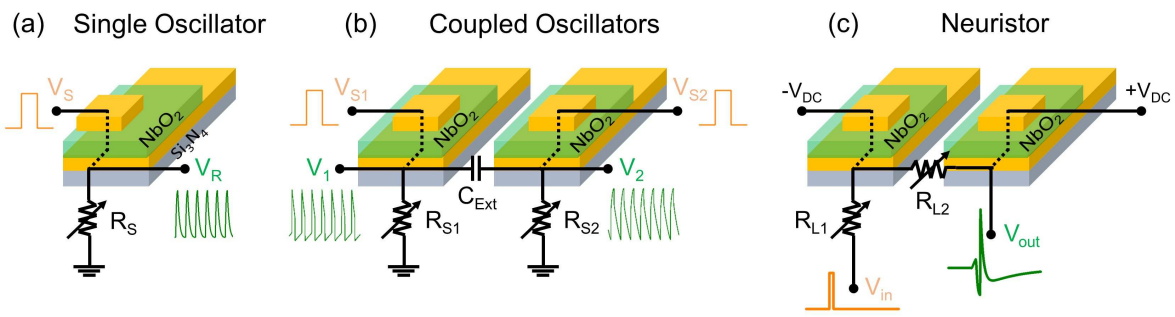

Figure 1.1: Schematic circuit diagram of single, coupled and neuristor models.

activity [20–22].

As shown in Fig. 1.1(c), the resting potential of each ion channel is represented by a DC voltage with opposite polarities. The input voltage pulse imitates the total stimulus from other neurons. The device parallel capacitors start charging when an excitation signal is received. If the excitation reaches the switching threshold, the devices will transit from an insulating state to a metallic state. Subsequently, the parallel capacitors discharge due to the drop in device resistance. The dynamical changes of device conductance are analogous to the opening and closing of ion channels in the Hodgkin-Huxley model. An electrical spike, akin to an action potential, is generated as an output signal. If the input signal is sub-threshold, the neuristor generates an attenuated output. The interval between spikes and the width of each spike can be modulated by tuning the parallel capacitors. Identical neuristors can be connected in series to behave like an axon to transmit the action potential pulse.

Synchronisation of coupled dynamic systems is a collective rhythmic response of individual elements in a small or large complex environment. Synchronous oscillatory systems exhibit rich coupling dynamics that have attracted consistent scientific interest for understanding the main mechanisms responsible for such kinds of nonlinear response [24–26]. In the brain, neurons form a network of coupled oscillators where they can achieve frequency or phase synchronization [27–29]. The process of neural oscillations and synchronization is believed to link to important cognitive functions, such as information processing, conscious awareness, memory or learning [28–32].

The neural oscillatory system motivates the development of biologically inspired solid-state coupled oscillator arrays for applications in non-Boolean computing. It has been demonstrated that assemblies of synchronous oscillator arrays werer capable of performing associative processing, such as pattern recognition and image restoration [33,34]. A single self-sustained oscillator acts as an oscillator neuron that forms the basis of oscillation as shown in Fig. 1.1(a). Conventional CMOS oscillators require a cluster of active components which sets challenges for integration due to

the approaching limits, such as device downscaling and high power dissipation [35].

Transition metal oxide based volatile threshold switching devices have been proposed for a wide range of applications, including as selector devices in a crossbar memory and a random number generator, due to their simple MIM device structure, high scalability, fast switching time and low energy consumption [36–38]. Under a current source excitation, the quasi-static current-voltage characteristics of such device exhibit a negative differential resistance region (CC-NDR) as the occurrence of local activity that underlies the threshold switching effect [39]. The CC-NDR device is capable of sustaining self-oscillation with a series resistor and can be easily controlled by tuning the resistive and/or capacitive components. The single and coupled systems of such relaxation oscillators is an important fundamental building block for developing alternative computing methods.

There are two examples of hardware implementations that have been recently demonstrated by using oxide-based CC-NDR driven oscillators as solutions for NP-hard (non-deterministic polynomial-time hard) problems, specifically solving the vertex colouring and travelling salesman problems [40, 41]. The first approach, proposed by Parihar et al., used a system of capacitively coupled VO_2 based relaxation oscillators to offer an approximate solution for graph colouring by leveraging the combined repelling effect in a stable state [40]. Such effect is a result when two directly connected oscillators are in frequency synchronisation, but showing anti-phase locking. Graph coloring can be used in a number of specific applications, including register allocation and scheduling [42]. The second approach, reported by Kumar et al., proposed to integrate NbO_2 chaotic oscillators into the Hopfield networks to enhance the computational efficiency and accuracy for solving global optimization problems [41]. Since firstly introduced by John Hopfield in 1982 [43], the Hopfield networks have been applied to solve a broad range of optimisation problems [44, 45]. However, one of common issues is that the networks are likely trapped in sub-optimal local minima. This underlying issue can be mitigated by computing the threshold function with incorporation of the chaotic behaviours in NbO_2 memristor

for convergence to a global minimum.

Fig. 1.1(b) shows a schematic of coupled oscillator circuit configuration where two oxide based CC-NDR devices are in series with a resistor each and coupled via a mutual external capacitor. The devices are initially in a high-resistance state. When a sufficient electrical input is applied, one device is able to switch from a high-resistance state to a low-resistance state. Concurrently, a voltage potential difference across the coupling capacitor is created and results in a current flow through the counterpart device and the associated series resistor. This induces voltage changes across the devices. The coupling strength is controlled via the variable coupling capacitor. The experimental realization of such compact and scalable coupled oscillation systems has been demonstrated in NbO_x and VO_x based relaxation oscillators and is of particular significance for design and implementation of large oscillator arrays for applications in non-Boolean computing [46, 47].

1.2 Thesis outline

This study aims to investigate the nature of threshold switching (current-controlled negative differential resistance) behaviour in amorphous niobium oxide and understand oscillation dynamics of isolated and coupled devices for applications in non-Boolean computing.

This dissertation is structured in seven chapters. Chapter 1 introduces basic concepts for the balance of the thesis. The chapter starts with reviewing the fundamental conduction mechanism in dielectric films and an overview of two types of metal-insulator transitions. We then proceed to cover fundamental knowledge on the general operations and switching mechanisms of resistive random access memory. With a specific research focus on niobium oxide, we review material properties and switching behaviour in niobium-oxygen systems. The chapter concludes with a review of recent progress in transition metal oxide based single and coupled oscillators.

In Chapter 2 we provide a brief description of experimental techniques used for

device fabrication and characterisation, and numerical modelling methods. Evolution of the numerical models are discussed. The characterised physical and electrical properties of NbO_x thin films are discussed in Chapter 3. The explored physical properties include surface morphology, physical structures and stoichiometry. From the electrical characterisation, we demonstrate that a diverse range of switching behaviours are observed in NbO_x.

Chapter 4 investigates the threshold switching anatomy within a self-assembled threshold-memory device as a function of device area and NbO_x layer thickness. The invariance of the threshold and hold voltages with area and thickness was shown to be consistent with the formation of a localized threshold switching volume at the residual conductive filament/electrode interface. The reduction in threshold power with increasing film thickness suggests the existence of a semiconducting shell around a filamentary core. A physical model based on the core/shell structure is developed and the veracity is demonstrated by comparing experimental results with the predictions of a resistor network model and more complex finite element simulations. The sub-threshold conduction mechanism is subsequently studied as a function of temperature.

Understanding the self-oscillation behaviour of NbO_x threshold switching devices is the focus of Chapter 5. We show that the NbO_x based oscillator exhibit low power operation, large frequency tunable range, high endurance and high temperature tolerance. The effects of source voltage and load resistance on oscillation frequency and tunability can be predicted with the Schimdt model and load-line analysis. Finally, we demonstrate that a finite element model that accounts for threshold switching behaviour can provide the basis for studying the interdependence between the switching response and oscillation characteristics.

In Chapter 6, we demonstrate the experimental realisation of compact, scalable and low power coupled oscillator systems. The coupled oscillators show rich collective dynamics, from weak to strongly coupling with phase locking and synchronised frequency. Three distinct coupling regions are identified. We show that the coup-

ling dynamics and modes can be captured with a physics-based finite element model with inclusion of circuit parameters.

The thesis is concluded with a summary of the experimental and simulation results, significance of the findings and discussions on future research directions.

Chapter 2

Background

This chapter begins by introducing the basic concepts of volatile threshold switching and non-volatile resistive switching in transition metal oxides, conduction mechanism in dielectric thin films, and the basics of metal-insulator transitions. It follows with a discussion of the switching phenomena in niobium oxides and reviews the recent progress of electrical self-oscillation in transition metal oxides.

2.1 Volatile threshold switching in transition metal oxides

Electrical switching in dielectric films has attracted research interest for more than half a century. The phenomenon can be classified into two types: volatile threshold switching and non-volatile resistive switching. Both result from a nonlinear change in electrical conductivity where the material transits from a high-resistance insulating state to a low-resistance metallic state [48–52]. In general, the transitions can be triggered by various external stimuli, including electrical, thermal, magnetic and mechanical excitations [53]. The low resistance state of volatile threshold switching devices is only sustained while sufficient power is applied and reverts back to the initial high resistance state when the excitation source is removed. Two terminal devices can be considered a memristor if it displays either volatile threshold switching or non-volatile resistive switching [54,55].

Historically, Morin was one of the first researchers to report volatile threshold switching in polycrystalline and single crystal forms of vanadium and titanium oxide systems [56]. A wider range of binary oxide systems (e.g. NbO_x, TaO_x, FeO_x) have been subsequently shown to exhibit volatile threshold switching behaviour in both amorphous and crystalline forms [57–65]. The transition temperature of such materials ranges from ∼70 K to ∼1070 K with a change of electrical conductivity up to seven orders of magnitude. Within these materials, crystalline NbO_2 is well known for a relatively high transition temperature, ∼1070 K, with up to three orders magnitude change in electrical conductivity [66–68]. It is worth mentioning that threshold switching has also been reported in amorphous NbO_x (x = 2 to 2.5) with or without an electroforming process [69].

Despite prolonged experimental and theoretical study, the physical origin of threshold switching in NbO_x thin films remains uncertain. A wide range of methods have been employed to synthesize crystalline or amorphous NbO_x that exhibit threshold switching response, including: sputtering, reactive bias target ion beam deposition, thermal oxidation and pulsed laser deposition [51, 70–72]. The unclear switching mechanism and its highly non-linear switching response make NbO_x of great scientific and technological interests.

2.2 Electrical transport properties of thin films

The conduction mechanisms in MIM structures can be broadly classified into interface/electrode dominated and bulk dominated conduction. Electrode-dominated conduction mechanisms include Schottky emission, Fowler-Nordheim tunnelling and direct tunnelling, while bulk dominated conduction mechanism include Poole-Frenkel emission, hopping conduction, ohmic conduction, space-charge-limited conduction and ionic conduction.

2.2.1 Electrode-limited conduction

Schottky emission

Schottky emission is a thermally-activated conduction mechanism in which electrons from the metal electrode can be emitted into the dielectric layer over a Schottky barrier. The schematic energy band diagram of the Schottky emission is shown in Fig. 2.1. The current density, J, from the Schottky emission in relation to temperature, T, electric field, E_{ox}, and the Schottky barrier height, $q\Phi_B$, can be expressed as the following [73]:

$$J_S = AT^2 exp\left[\frac{-q\Phi_b + \sqrt{qE_{ox}/4\pi\xi_r\xi_0}}{kT}\right] \tag{2.1}$$

where A is the Richardson constant expressed as $A = 4\pi qk^2m^*/h^3$, E is the electric field across the dielectric layer, T is the temperature. The current density of the Schottky emission has a dependence on both temperature and electric field.

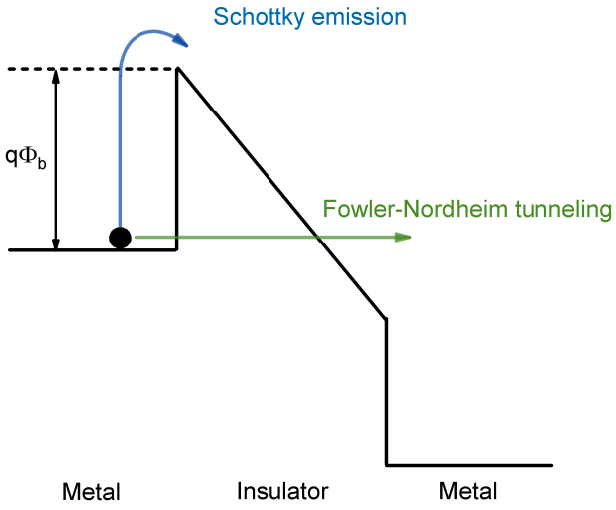

Figure 2.1: Schematic energy band diagram of Schottky emission and Fowler-Nordheim tunneling in a metal-insulator-metal structure.

Fowler-Nordheim tunnelling

Fowler-Nordheim (F-N) tunnelling is a conduction process that occurs in thin oxides, electric field reduced tunnelling barrier with schematic energy band diagram as shown in Fig. 2.1. Electrons from the metal electrode tunnel through the potential triangular barrier to the conduction band of the dielectric subject to the presence of applied high electric field [74]. The basic expression of F-N tunnelling current density can be represented as the following [75]:

$$J_{FN} = \alpha {E_{ox}}^2 exp\left(\frac{-\beta}{E_{ox}}\right) \tag{2.2}$$

where

$$\alpha = \frac{q^3}{8\pi h \Phi_b} \qquad \beta = \frac{8\pi\sqrt{2qm^*{\Phi_b}^3}}{3qh}$$

Behaviour of the F-N tunnelling current as a function of voltage can be measured at low temperature as the field-driven emission will be dominant due to suppression of the thermally-driven emission.

Direct tunnelling

Direct tunnelling only becomes dominant in ultra-thin dielectric where electrons directly tunnel through the films [76]. The tunnelling can be approximated as [73]:

$$J_{DT} \approx exp\left(-\frac{8\pi\sqrt{2qm^*\Phi_b}}{3h}\kappa \cdot t_{ox,eq}\right) \tag{2.3}$$

where the tunnelling current J_{DT} is dependent on the κ value of the dielectric material, equivalent oxide thickness, $t_{ox,eq}$, and the tunnelling barrier height, Φ_b.

2.2.2 Bulk-limited conduction

Poole-Frenkel emission

Poole-Frenkel (P-F) emission is due to electrons under an electric field emitted from traps into the conduction band of the dielectric. When an electric field is applied across the insulator, the field-induced barrier lowering increases the probability of electron emission as illustrated in Fig. 2.2 [77]. The current density has the form of [73]:

$$J_{PF} = q\mu N_C E_{ox} exp\left[-\frac{q\Phi_T - \sqrt{qE_{ox}/\pi\xi_r\xi_0}}{k_B T}\right] \tag{2.4}$$

where μ is the electron mobility, N_c is the density of allowed states in the conduction band, Φ_T is the level of trap energy.

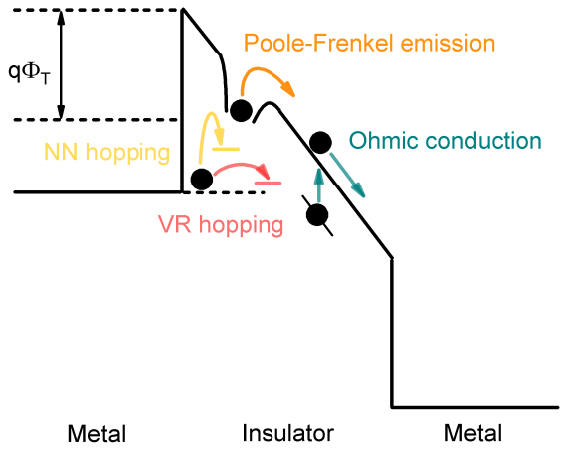

Figure 2.2: Schematic energy band diagram of Poole-Frenkel emission, nearest-neighbour (NN) hopping, variable-range (VR) hopping and Ohmic conduction in a metal-insulator-metal structure.

Hopping conduction

Hopping conduction occurs when trapped electrons hop from one trap site to another within a dielectric layer. There are two types of hopping mechanisms, including nearest-neighbour hopping (NNH) [78,79] and variable-range hopping (VRH) [80,81] as shown in the schematic energy band diagram of Fig. 2.2. In the NNH scheme, electron hopping occurs between nearest neighbours and the the current density exhibits as Arrhenius-like temperature dependence as shown in Equation (2.5), where E_a is the activation energy. For the VRH conduction, electrons can hop to trap sites that are further away with lower trap energy. Equation (2.6) shows the temperature dependence of the current density, where T_0 is the characteristic temperature.

$$J_{NNH} = J_0 exp\left(-\frac{E_a}{k_B T}\right) \tag{2.5}$$

$$J_{VRH} = J_0 exp\left(-\frac{T_0}{T}\right)^{1/4} \tag{2.6}$$

Ohmic conduction

Despite the relatively large energy band gap of the dielectrics, a small concentration of thermally-induced mobile electrons can generate a current that is linearly proportional to the applied electric field. The schematic energy band diagram of Ohmic emission is shown in Fig. 2.2. For Ohmic conduction, the current density can be expressed as:

$$J_O = q\mu N_C E_{ox} exp\left[-\frac{E_a}{k_B T}\right] \tag{2.7}$$

Space-charge-limited conduction

Space-charge-limited (SCL) conduction occurs when the current is dominated by electron injection from electrodes [82, 83]. At low field, the rate of electron injection is relatively low and the current is largely determined by the intrinsic free electron density. The low-field current and voltage exhibit an Ohmic relation. With increasing electric field, the density of mobile carriers injected from the electrode increases and eventually dominates the conduction. At high field, trap-free current voltage characteristics may apply as all traps are filled up and injected mobile carriers are able to freely move within the dielectric. In the absence of traps and only considering a single type of carriers, the current density can be described by the Mott-Gurney relation as shown in Eq. 2.8 [84]:

$$J_{SCLC} = \frac{9}{8}\mu\xi_0\xi_r\frac{V^2}{d^3} \tag{2.8}$$

where d is the dielectric film thickness. Eq. 2.9 is the modified form of Eq. 2.8 which includes the case of a single set of traps with energy level below the conduction band. θ is the ratio between free and total charge densities.

$$J_{SCLC} = \frac{9}{8}\mu\xi_0\xi_r\theta\frac{V^2}{d^3} \tag{2.9}$$

Ionic conduction

Ionic conduction is due to movement of ions under the influence of an electric field. The movement arises through field-induced potential barrier lowering and lattice defects. The ionic conduction current density can be expressed as [73]:

$$J_I = J_0 exp\left[-\frac{2q\Phi_T - Eqd}{2k_BT}\right] \tag{2.10}$$

where J_0 is the pre-exponential factor and d is the distance between two adjacent lattice sites. At low field, the current density has a linear dependence with electric field and an exponential relation is shown at high field.

2.3 Metal-insulator transition

Metal-insulator transitions (MIT) can arise from electron-ion interaction or electron-electron interaction. In the first category, the MIT triggered by electron-ion interaction comprise the Anderson transition and Peierls transition. The second category constitute Mott or Mott-Hubbard transition where the MIT is dominated by electron-correlation effects.

Anderson transition shows a continuous MIT between metallic and insulating states induced by disorder. Several decades ago, Anderson reported that electron localisations can be induced by randomly distributed lattice defects or impurities in which results in an insulating state [85–87]. The localised electrons lead to the rise of a mobility edge that has the energy to set apart the localized and non-localised states [87]. Insulating state generally occurs when the Fermi energy underlies within a band and its associated mobility edge [87]. The Anderson transition commonly exists in strongly disordered material systems, such as phosphorus-doped silicon (Si:P) or selenium-doped germanium (Ge:Se) [87].

Peierls transition or Peierls instability is an electron-phonon (electron-lattice) induced structural transformation of a material between a periodic crystal lattice and a distorted phase [88,89]. The symmetry breaking of the original lattice occurs at a critical transition temperature and is accompanied by the formation of new periodic potential which changes the electronic band structure. This consequently gives rise to modifications of material intrinsic properties, such as electrical conductivity and bandgap. $K_{0.3}MoO_3$ and $(TaSe_4)_2I$ are two classical examples of Peierls insulators [87]. The electrical resistivity of these two materials increases exponentially with reduced temperature and undergo MIT, accompanied by structural change, at 181

K for $K_{0.3}MoO_3$ and 265 K for $(TaSe_4)_2I$. The Peierls instability is also believed to be responsible for the MIT in crystalline NbO_2 which exhibits an abrupt increase in electricity conductivity at ∼1070 K. More details on the transition mechanisms will be discussed further.

In addition to the electron-ion interaction (single particle), MIT phenomenon can also arise from many-body effect that includes the electron-electron interactions. Mott proposed a model to describe the electron correlation effect several decades ago. In the simplest scenario, a material exhibits insulating behaviour with a sufficiently large lattice constant where electrons are bound by the nuclei [90, 91]. As the spacing between atoms decreases, the electron density increases and screened Coulomb (Yukawa) potentials appear. With the carrier density higher than a critical value, the material transits to metallic conduction as bound states no longer exist for the outer electrons which leads to generation of delocalized electrons for electrical conduction. The criterion for Mott transition is given by $n_c{}^{1/3}/a_0 \propto 0.2$, where n_c is the critical carrier density and a_0 is the Bohr radius [90, 91]. The insulators formed by strong electron correlations are categorized as Mott or Mott-Hubbard insulators. A classical and well-studied example that exhibits metal-Mott insulator transition is V_2O_3 [90, 92]. The material undergoes a first-order transition from a low-temperature antiferromagnetic insulating phase to a paramagnetic metallic phase when the temperature exceeds ∼160 K.

2.4 Resistive random access memory in oxides

Consumers' ever-growing demand for information in electronic devices requires fast information processing and high-density data storage. This drives continuing improvement of computing performance which leads to rapid advancement of memory technologies. Non-volatile memory (NVM) is one of the most important sub-systems within computer chips and secondary information storage that is partially responsible for computing speed, reliability and energy consumption.

Currently, FLASH memory is the most widely-adopted NVM technologies due to its fast innovation and competitive device scability. FLASH memory consists of an array of memory cells. The basic operation of each cell involves a floating gate transistor where the electrically isolated floating gate allows charge to be trapped or removed. The current FLASH memory devices have been scaled down to ∼15 nm in pursuit of lower power consumption, faster program time and higher device density [93]. Further downscaling will soon approach a bottleneck due to the rise of a number of significant issues, such as charge leak and voltage stress induced defect formation. The potential challenges can reduce device reliability, endurance and impose a physical limit on device density.

Due to the upcoming challenges associated with FLASH memory, several emerging non-volatile memory technologies have been explored and proposed as future solutions. These candidates include ferroelectric random access memory (FeRAM), magnetoresistive RAM (MRAM) [94], phase change RAM (PCRAM) [49], and resistive RAM (ReRAM) [95].

Among these emerging memory technologies, ReRAM has been shown to be one of the promising emerging non-volatile memory technologies due to excellent switching performance, including low energy consumption, fast programming speed, excellent scalability, long retention time and endurance [95]. ReRAM devices based on transition metal oxides are based on a simple metal-insulator-metal (MIM) structure that can be switched between a high resistance state (HRS) and a low resistance state (LRS). The broad taxonomy of the ReRAM conduction and switching mechanisms is highlighted in the recent reviews by Wong *et al.* [96], Waser *et al.* [97], Sawa *et al.* [98] and Akinaga *et al.* [99]. Thermochemical memory (TCM) and valence change memory (VCM) are the two types of ReRAM presented and discussed in this section. In addition to the practical interest of replacing the current FLASH memory technology, recent studies have also investigated the emerging application of ReRAM as artificial synapses for neuromorphic computing [6, 7].

Prior to operation, the binary oxide ReRAM devices are typically in a highly

insulating state and an electroforming process is required to initiate non-volatile resistive switching. This is realised by applying a sufficiently high voltage across the top and bottom electrodes and device resistance will be modified by several orders of magnitude due to a dielectric soft-breakdown process [99]. During the forming process, a current compliance is generally applied to prevent the ReRAM devices from permanent breakdown. A localised conduction filament is created with oxygen vacancies [100–102]. Device resistance remains in its current state without external electrical power. The resistance of the device can be changed with applied voltage in the same or opposite polarity. The transition from LRS to HRS is known as "RESET" process and the device is in "OFF" state. Conversely, the switching from HRS to LRS is described as a "SET" operation. The SET and RESET processes correspond to the formation and rupture of a localised conduction filament.

ReRAM devices can generally be classified into two types of resistive modes, unipolar and bipolar [95]. Unipolar switching is independent of voltage polarity which means that devices can be SET and RESET by applying the same voltage polarity to control the type of operation [95]. Fig. 2.3(a) shows the typical unipolar switching I-V characteristics. The underlying switching mechanism in unipolar switching is be-

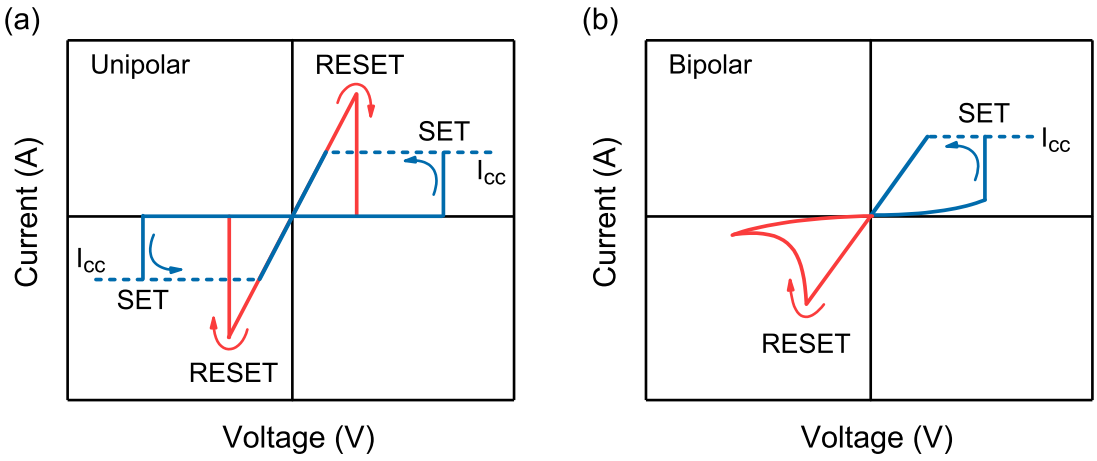

Figure 2.3: Typical current-voltage characteristics of (a) unipolar switching and (b) bipolar switching.

lieved to predominantly result from the TCM mechanism. During the SET process, a metal-rich conductive filament is formed by local oxide reduction [103, 104]. For the RESET process, the conduction filament is partially dissolved due to local Joule-heating induced thermal oxidation [105]. The typical RESET process in unipolar switching has an abrupt change in current-voltage characteristic. For the VCM-type bipolar switching, the SET and RESET operations are dependent on the polarity of the applied voltage. As shown in Fig. 2.3(b), a device is SET with a positive bias, but can only be RESET by applying a negative bias. The SET process involves formation of an oxygen-deficient filamentary conduction path where a valence change of cation sublattice occurs. For the RESET process, an opposite electric field is required to assist the migration of oxygen ions and vacancies and a gap is opened within the conductive filament [106].

The type of switching mode in ReRAM devices can be determined by several factors, including nature of the binary oxide systems, fabrication process, active or inert electrode materials, and operating voltage and current. In the subsequent section, a general overview of non-volatile resistive switching in the niobium-oxygen systems will be discussed.

2.5 Switching phenomena in niobium oxides

2.5.1 Niobium-oxygen system

The properties of the niobium-oxygen (Nb-O) system have been extensively studied since the 1940s. There are three main stable niobium oxides: niobium monoxide (NbO) [107–111], niobium dioxide (NbO_2) [112–117] and niobium pentoxide (Nb_2O_5) [118–121]. Fig. 2.4 shows the phase diagram for the Nb-O system proposed by Elliot. A range of metastable NbO_x ($0<x<1$ and $2<x<2.5$) have also been reported by a number of independent studies [122–128]. An overview of the stable oxides and pure niobium metal characteristics with technological implications are

presented in the subsequent sections.

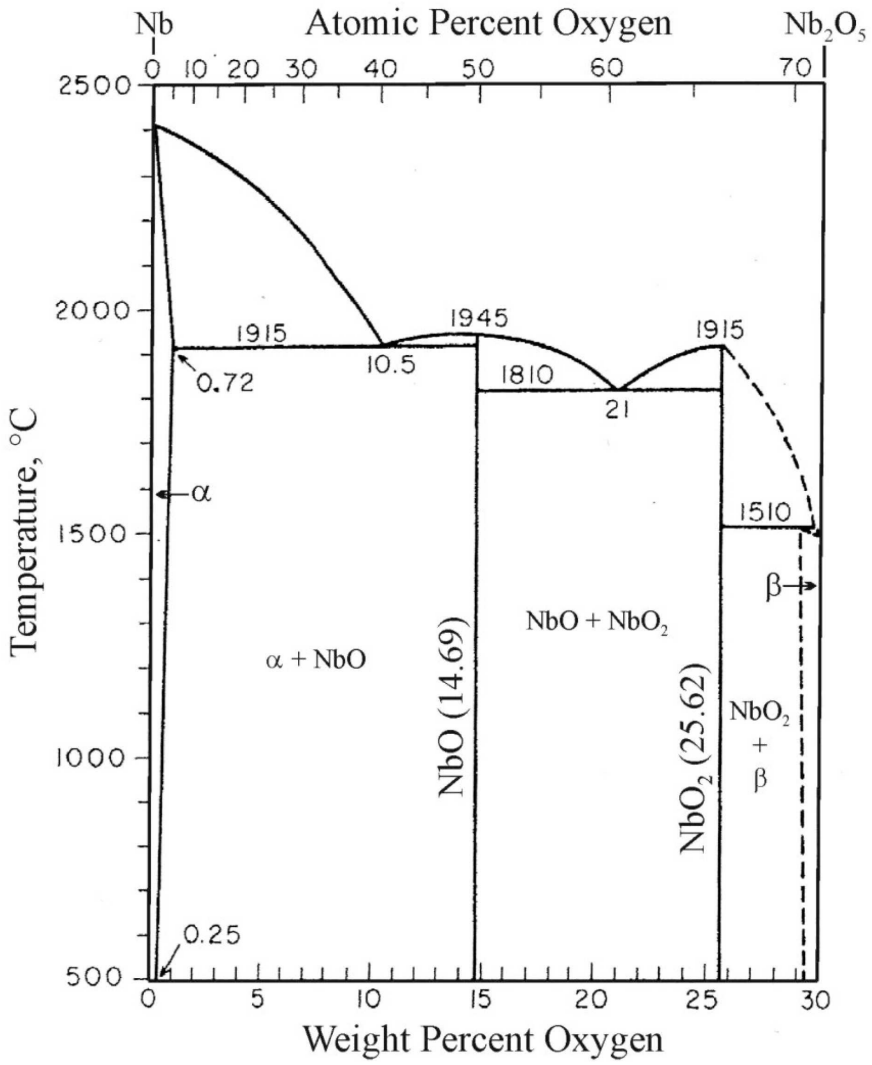

Figure 2.4: Phase diagram of Niobium-Oxygen system [129].

Niobium is one of the group 5 elements in the periodic table, along with vanadium and tantalum. Pure niobium metal has a body-centred cubic crystal structure and a density of ∼8.57 g/cm^3 [130]. Niobium is highly conductive with electrical conductivity reported between 2.5×10^6 and 5.9×10^7 S/m [131, 132] and a relatively high thermal conductivity of ∼52 W m^{-1} K^{-1} [131]. With exposure to oxygen, a niobium oxide layer is inevitably formed due to the high affinity and binding energy for oxygen [126, 133, 134]. Niobium has been used in numerous technological

areas, including as an element to optimise the steel properties, a wear and corrosion resistance coating layer and niobium based superconducting applications.

Stable niobium monoxide (NbO) has a defective rocksalt structure which contains up to a quarter of ordered vacancies on both niobium and oxygen sublattices [109, 110, 122]. Despite a decrease in electron density, NbO presents highly conductive metallic behaviour with reported electrical conductivity of $\sim 4.8 \times 10^6$ S/m at room temperature [135]. Stoichiometric NbO exhibits superconducting characteristics at $\sim$1.4 K [135]. Apart from being used as superconductor, NbO has been used as a gate electrode in n-channel metal-oxide-semiconductor field-effect transistor [136].

Niobium dioxide (NbO_2) is an n-type semiconducting material that can exist in the form of either an amorphous or crystalline structure [137–139]. Single crystal NbO_2 has a density of ~ 5.9 g/cm^3 [68,140] with a deformed tetragonal rutile lattice at room temperature and a band gap $\sim$0.5 eV [141]. At room temperature, the electrical conductivity has a range between 1.25×10^5 and 5×10^5 S/m [142]. The unit cell consists of edge-sharing pairs of distorted octahedral NbO_6 that are cross-linked by corner-sharing. Stoichiometric crystalline NbO_2 exhibits a metal-insulator transition at approximately 1070 K with an abrupt change in electrical conductivity [68, 115]. The MIT mechanism is generally understood as the Mott-Peierls transitions where a concurrent change of crystal structure occurs from a distorted rutile structure to a regular rutile structure. NbO_2 has been of great interest in current and emerging technologies, including voltage-controlled oscillators, optical modulation and neuromorphic computing applications [18, 143, 144].

Stoichiometric niobium pentoxide (Nb_2O_5) is generally considered to be an insulating oxide, and exists in amorphous and numerous crystalline forms. Nb_2O_5 is the most thermodynamically stable oxide within the Nb-O system due to the largest negative Gibbs free energy of formation [145]. Nb_2O_5 is optically transparent due to its large band gap, between 3.3 eV and 3.9 eV [146–148], and has a reported density ~ 4.5 g/cm^3 [140]. The polymorphism of Nb_2O_5 results from collective effects, including synthesis methods, annealing temperature and sample substrate. Approx-

imately 15 Nb_2O_5 polymorphs have been reported. Four frequently observed forms of crystal phases are identified as tetragonal (M-Nb_2O_5), monoclinic (H-Nb_2O_5), orthorhombic (T-Nb_2O_5) and pseudohexagonal (TT-Nb_2O_5) [118–121, 149, 150]. Each crystalline phase can be obtained at different temperatures from amorphous Nb_2O_5. At temperature of approximately 500 ^oC, the amorphous phase crystallizes into TT or T phases. As temperature increases to ~800 ^oC, Nb_2O_5 transforms into the M phase, and for temperatures above 1000 ^oC, it stabilizes into the H phase. The H-Nb_2O_5 structure is composed of a chain of blocks where each block consists of 4×3 or 5×3 groups of corner-linked NbO_6 octahedron. The medium temperature M phase incorporates 4×4 groups of NbO_6 octahedron within each block. The low temperature TT and T phase comprises corner or edge-sharing NbO_6 and NbO_7 polyhedra in each lattice. The physical properties of Nb_2O_5 are strongly affected by the precise stoichiometry and structure, with the electrical conductivity of Nb_2O_5 varying over 7 orders of magnitude from 10^{-13} to 10^{-6} S/m, with small deviations in stoichiometry [151–155]. Nb_2O_5 is of technological interest as a memristor, sensor and MIM capacitor [156–158].

2.5.2 Non-volatile resistive switching in NbO_x

Within the Nb-O system, the non-volatile switching in Nb_2O_5 is the most well studied and exploited due to its high thermodynamic stability and commonly observed memory switching effect. The other two stable forms of oxides, NbO and NbO_2 are dominated by their metallic conduction and volatile threshold switching characteristics. Memory effect of Nb_2O_5 was discovered in the 1960s and subsequent studies have investigated the switching characteristics and the underlying switching mechanisms [159–162]. Both unipolar switching and bipolar switching have been observed in Nb_2O_5 based MIM devices. Bipolar resistive switching is generally achieved when an oxygen gradient occurs within the device stacks. This requires at least one reactive metal at the top or bottom electrode to reduce oxygen concentration at

the metal-oxide interface by forming a sub-stoichiometric oxide layer [163,164]. The oxygen deficiency at the interface enriches defect concentration. The inhomogeneous oxygen concentration throughout the oxide layer enhances the device switching to be dominated by electric field dependent mechanism. Unipolar switching is commonly realised with inert top and bottom electrodes [163–166].

2.5.3 Volatile threshold switching in NbO_x

Thermal and electric field induced threshold switching have been observed in NbO_2 and nonstoichiometric NbO_x phases. The highly nonlinear change of electrical conductivity was first observed in the 1960s by Geppert [167]. NbO_2 exhibits a thermally-induced threshold switching at ∼1070 K which is associated with a spontaneous structural transformation from a low-temperature distorted rutile structure (space group $I4_1/a$) to a rutile structure with a body-centered tetragonal lattice (space group $P4_2/mnm$) at high-temperature [66,67,137–139,168] as shown in Fig. 2.5. The transition has been reported for electrical stimulation and thermal excitation, with up to three orders of magnitude change in electrical conductivity and sub-nanosecond switch time [37,114]. With electrical stimulation, the transition occurs when the input power exceeds a certain threshold point. While the precise underlying mechanism remains uncertain, there is growing consensus that the abrupt transition in crystalline NbO_2 results from Mott-Peierls transition type where dimerization occurs between pairs of niobium atoms during the structural change [67,168].

Threshold switching has also been observed in amorphous NbO_x thin films with a MIM device structure from micro- to nano-scale. An electroforming step is generally required for pristine thin films in order to initiate the nonlinear response. However, reports on necessity of a soft-breakdown process is mixed with dependence on stoichiometry and thickness of the oxide layer [69,170]. Several filamentary based switching models have been studied and these can be categorised into two

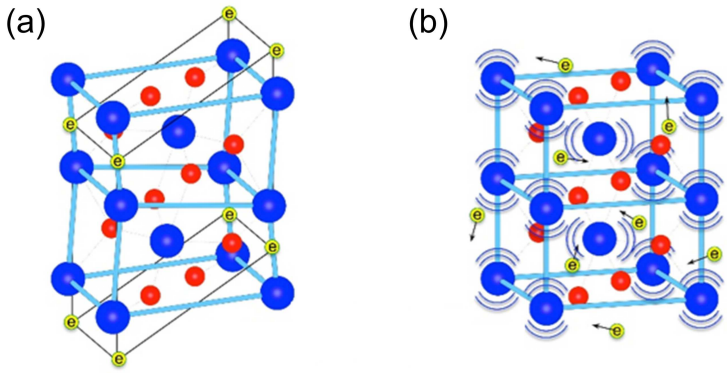

Figure 2.5: (a) Unit cell of NbO_2 at the low-temperature distorted rutile structure. (b) Unit cell of NbO_2 at the high-temperature rutile structure. [169].

main mechanisms. The first model was proposed by Pickett *et al.* based on localised Joule heating induced filamentary phase transformation [37]. In this interpretation, an electroforming process is required to form a cylindrical NbO_2 volume. As current flows through this volume, an inner metallic core is formed when the internal temperature is Joule heated above the MIT (∼1070 K) transition temperature [37]. The metallic core is then surrounded by a cooler NbO_2 insulating channel. As higher current flows through the metallic filament, more heat will be generated for the expansion of the filament so as to reduce the overall device resistance.

The Poole-Frenkel assisted thermal runaway process with a combination of self-heating and exponential temperature and electric field dependence was recently proposed as an alternative switching mechanism [69, 171–173]. At low electric fields, Joule heating is relatively low. With further increases in field, the device current increases exponentially and is associated with a reduction in device resistance and a significant increase in the filament temperature due to a Joule-heating induced thermal runaway. The PF dominated threshold switching occurs in the range between 400 K and 450 K which is substantially below the 1070 K MIT transition temperature and the minimum crystallization temperature of niobium oxides [69, 170, 172]. The reported transition ON/OFF ratio is smaller than observed in single crystal and polycrystalline NbO_2 samples [115]. The difference can be at-

tributed to various factors, including quality of as-deposited material and deviations from stoichiometry.

2.6 Electrical self-oscillation in transition metal oxides

2.6.1 Single oscillator

Electrical self-sustained oscillations have been observed in a broad range of transition metal oxides that exhibit S-type current-controlled negative differential resistance (CC-NDR), including VO_x, NbO_x, TaO_x and TiO_x [58, 144, 174–176]. Under particular electrical excitation, two terminal metal-insulator-metal (MIM) device structures based on such materials are capable of sustaining self-oscillation between their bistable resistance states with a passive element (e.g. a load resistor). The properties of these CC-NDR driven oscillators make them suitable for applications such as voltage-controlled oscillators, electronic switches, neuristors, and oscillator neurons [18, 177–180]. Among these oxides, vanadium dioxide (VO_2) is one of the most well studied materials for the CC-NDR element in relaxation oscillators [174, 175, 178, 181] and has been shown to operate at frequencies in the range from 1 kHz to 9 MHz [174, 175, 178, 181–183]. However, its relatively low transition temperature (∼340 K) precludes its use in many microelectronics applications, where the expectation is that devices will operate at temperatures approaching 400 K. Recent interest has focussed on other oxides with higher operating temperatures, including NbO_x and TaO_x. TaO_x has been reported with higher operating frequencies and tunable range, but it requires integration with a pMOS transistor which limits the oscillator scalability [176].

Self-oscillations were first demonstrated in bulk niobium oxide based two terminal devices by Geppert in 1963 [167]. Subsequent follow-up studies by Lalevic and Chopra reported stable and periodic oscillations up to ∼600 kHz in polycrys-

talline and single-crystal NbO_2 thin films. However, the oscillators presented in the earlier studies required high operating voltage and current. Although recent studies by Pickett *et al.* [37] have been able to show significant reduction in device operating power and increase in oscillation frequency with downscale in device area, it still requires more systemic and in-depth study on understanding the general oscillation characteristics and exploring the suitability of NbO_x threshold switching devices as self-sustained oscillators. The oscillator circuit set-up used in this study will be discussed with details in the subsequent chapters.

2.6.2 Coupled oscillators

Coupled oscillator networks stimulate the advancement of understanding the computational capability of the nervous system and developing biologically inspired solid-state coupled oscillator arrays for applications in non-Boolean computing [33, 34]. Coupled systems based on CC-NDR driven oscillators in transition metal oxides have attracted recent research interest as an emerging technology to replace CMOS integrated oscillatory networks due to its compact network structures, flexible device scalability and low power consumption [18, 46]. The earlier work in coupled oscillators have mainly focused on theoretical understanding [34, 184]. Recent studies have experimentally investigated the coupling dynamics and demonstrated the potential of CC-NDR devices in VO_2 for use as coupled oscillators [46, 185, 186]. However, experimental study on coupling dynamics of NbO_x based CC-NDR driven oscillators have received far less attention despite its low power operation, broad frequency tunability, higher operating frequency and tolerance to higher operating temperature [144, 187]. The experimental realisation of such compact, scalable and low power coupled-oscillator systems is of particular significance for development and implementation of large oscillatory network for neuromorphic computing applications.

Chapter 3

Experimental and Modelling Methods

This chapter presents a brief overview of the device fabrication procedures, characterisation techniques and numerical modelling methods which were used for the studies in the subsequent chapters. The studied thin films were prepared by using DC and RF sputtering. The methods of Rutherford back scattering (RBS), transmission electron microscopy (TEM), X-ray diffraction (XRD), and atomic force microscopy (AFM) were deployed to analyse the stoichiometry, thickness, crystallinity and roughness of the materials. The electrical response and underlying switching mechanisms were characterised using a semiconductor device analyser and detailed numerical modelling.

3.1 Device fabrication

3.1.1 Microscale device structure

Microscale devices (15 to 200 μm in diameter) used in this research were fabricated by successive layer deposition that consisted of metal-insulator-metal (MIM) capacitor structures. A thin insulating layer was firstly prepared on a Si substrate by either thermal oxidation (SiO_2) or plasma-enhanced chemical vapour deposition (PECVD) of Si_3N_4 as shown in Fig. 3.1(a). Prior to the deposition of bottom electrode, a Ti wetting layer was required in certain device structures to provide good adhesion between the electrode and the insulating layer. In the case of metals de-

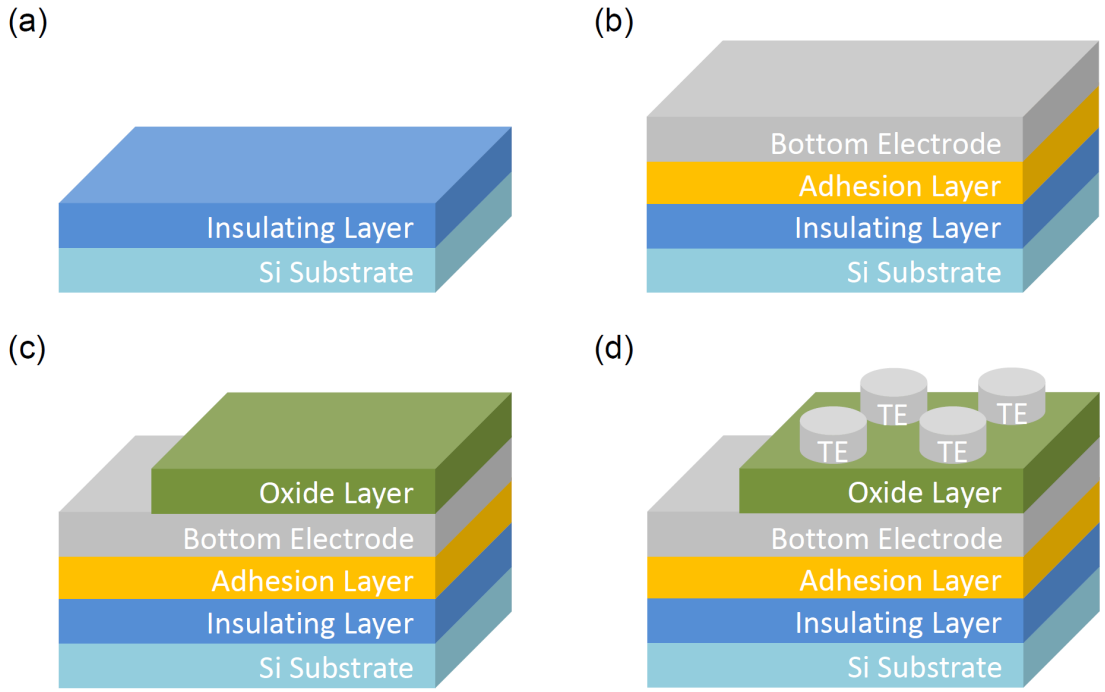

Figure 3.1: Schematics of micro-scale device fabrication procedures: (a) thermal oxidation or deposition of Si_3N_4 insulating layer (b) subsequent deposition of adhesion layer and bottom electrode (c) NbO_x thin films by sputtering deposition and (d) deposition of top electrode (TE) deposited with shadow mask.

posited onto Si_3N_4, sufficient adhesion was obtained by using in-situ cleaning with Ar-ion bombardment in the electron beam evaporation system. The bottom electrode was subsequently deposited by electron beam evaporation as bottom electrode, as illustrated in Fig. 3.1(b). NbO_x films were then sputtered onto the bottom electrode with part of the area masked for bottom electrode access as shown in Fig. 3.1(c). Fig. 3.1(d) shows that the devices were completed by depositing the circular top electrode through a shadow mask by electron-beam evaporation.

3.1.2 Nanoscale device structure

Nanoscale MIM devices were fabricated with nanovia bottom electrode as shown in Fig. 3.2. The TiN bottom electrode was sputtered onto thermally oxidized wafers with oxide thickness of 500 nm (supplied by Hionix). An insulating layer of 65 nm

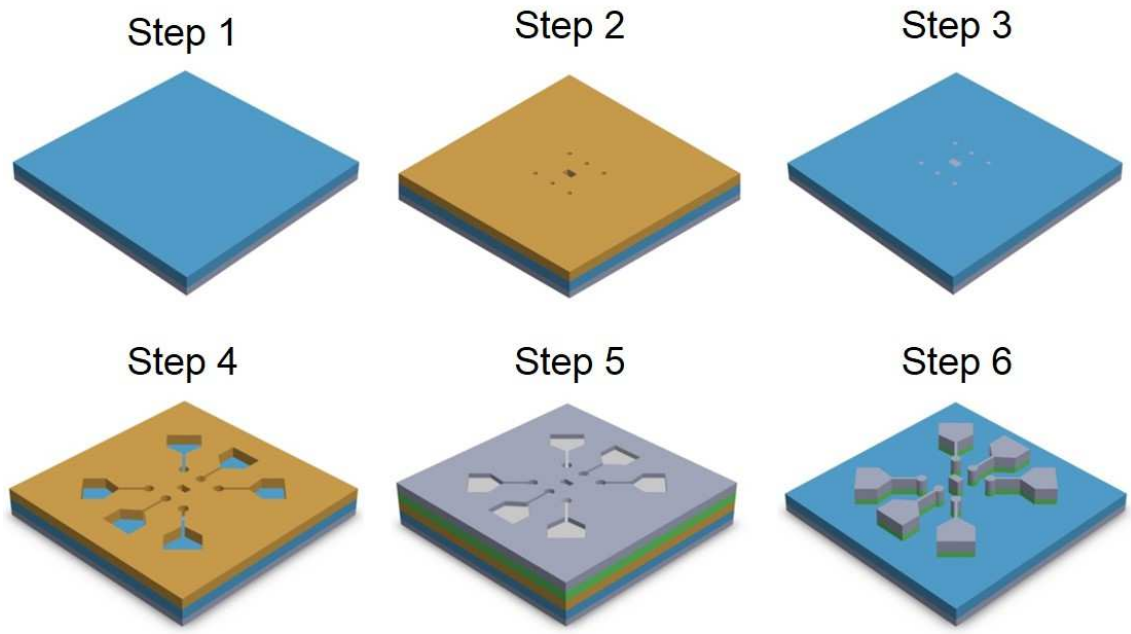

Figure 3.2: Schematic illustration of fabrication process for nanovia devices.

Si_3N_4 was then sputter deposited on TiN with an area masked for bottom electrode access (Step 1). Patterns of nanovia holes with a diameter of 400 nm were defined in photoresist by electron-beam (e-beam) lithography and etched through the Si_3N_4 layer by reactive ion etching to the TiN bottom electrode layer (Step 2). Radio frequency sputtered TiN was subsequently deposited and the TiN nanovia bottom electrodes were completed after the lift-off process (Step 3).

Top electrode patterns were directly written onto the the Si_3N_4 and TiN nanovia layer with e-beam lithography (Step 4). 50 nm thick films of NbO_x oxide were deposited onto the developed top-electrode patterns by reactive sputter deposition with a metallic Nb source and an Ar/O_2 gas mixture in the ratio of 17.5/2.5. A 50 nm Pt layer was then deposited on the oxide (Step 5). The nanovia devices were completed after the photoresist and the undesired NbO_x and Pt were removed in acetone at 60 ^{o}C (Step 6). Fig. 3.3(a) shows a top viewed SEM image for a block of 6 nanovia devices. A zoom-in view of top electrode and nanovia hole for an individual device is shown in Fig. 3.3(b).

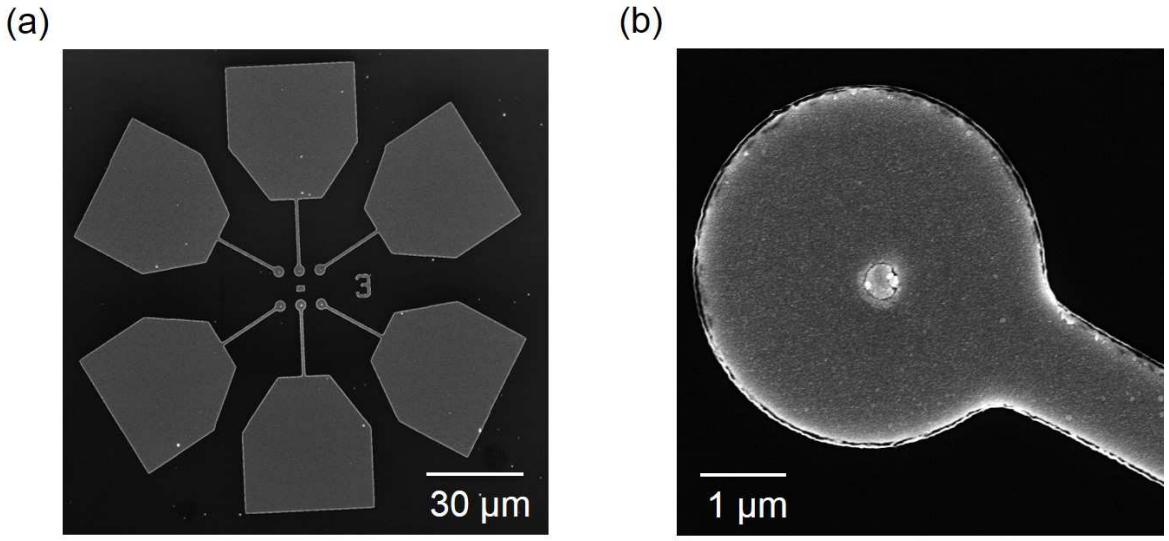

Figure 3.3: (a) Top-view SEM image of representative NbO_x devices. (b) Zoom-in SEM image of top electrode area for a single nanovia device.

3.2 Thin film synthesis and characterisations

3.2.1 Sputter deposition

The sputtering system used in this research was a commercial deposition system, AJA ATC 2400 UHV. NbO_x thin-film layer was prepared by using reactive sputtering with a Nb metal target (99.99% purity) and a DC power source. The deposition was performed at room temperature with processing pressure sustained at 4 mTorr and constant sputtering power of 150 W. The stoichiometry was controlled by the ratio of argon to oxygen between 18/2 and 17.5/2.5 with total flow rate at 20 standard cubic centimeters per minute. Stoichiometric Nb_2O_5 thin films were deposited at room temperature by radio frequency sputtering with Nb_2O_5 target (99.993% purity) under Ar gas flow.

3.2.2 Electron beam deposition

The top and bottom electrode metals (Pt, Nb and Ti) were deposited using electron-beam physical evaporation, Temescal BJD-2000. During the deposition process, a concentrated electron beam, generated from the electron gun, is directed towards the targeted material. The desired material is struck and vaporised by the beam with a base pressure of mid 10^{-6} Torr and working pressure of $\sim 10^{-5}$ Torr. The depositions were performed with a substrate temperature between 296.15 and 333.15 K.

3.2.3 Stoichiometry analysis

The composition of the NbO_x thin films were determined by Rutherford backscattering spectrometry (RBS) which is a widely adopted technique. The thin films with a typical thickness between (100 to 200 nm) were prepared on a carbon substrate and bombarded with high-energy (2 MeV) helium ions. A profile of energy versus yield of the backscattered ions at a given angle was recorded for each element contained in the sample. The stoichiometry was confirmed by simulating and fitting the RBS spectra in RUMP software [188].

3.2.4 Electrical measurement

Electrical characterisation of the NbO_x devices was performed using a Keysight B1500A Semiconductor Device Parameter Analyzer and Measurement Modules. The standard Source Monitor Unit (SMU) supports voltage-controlled and current-controlled sweeps and quasi-static capacitance-voltage measurements. Pulse/dynamic measurements were conducted with an embedded waveform generator/fast measurement unit (WGFMU). The electrical and temperature dependent measurements were performed in conjunction with a Signatone s-1060 thermal probing system with heated sample stage.

3.2.5 Surface morphology

The roughness of the NbO_x thin films was measured by using atomic force microscopy (AFM). The scans were taken over 1×1 μm^2 area at 1 Hz in tapping mode and the thickness of the thin-film samples was between 20 and 60 nm. In the tapping mode, the oscillating cantilever probe tip only touches the sample surface lightly to minimise the effect of lateral forces and drags on the surface. Morphology was imaged with a Bruker Multimode VIII AFM and the Gwyddion modular program was used to analyse the measurements and calculate the root-mean-squared roughness.

3.2.6 Crystallinity of thin films

The crystalline structures of the as-deposited and thermally-annealed samples were examined using grazing incident X-ray diffraction (GIXRD) with conventional $\theta/2\theta$ scanning methods. The NbO_x thin films were deposited on a $Pt/Si_3N_4/Si$ substrate. The X-ray (CuKα radition = 1.545 Å) strikes at the sample with a fixed grazing angle of 0.6 ^{o}C to avoid intense signal from the substrate. The measurements were carried out in a Hi-Resolution PANalytical X$'$Pert PRO MRD system. The X$'$Pert HighScore software was used to analyse the measured spectra and compare them with the known material crystalline phases.

3.3 Numerical modelling

Finite element simulations of the threshold switching behaviour in NbO_x devices were performed using the COMSOL Multiphysics software package by coupling electric current and heat transfer in the solids physics modules. DC switching characteristics were calculated by assuming an increasing voltage/current sweep for the nonlinear change in electrical conductivity from high-resistance insulating state to low-resistance metallic state. The two dimensional (2D) axisymmetric model was further coupled with the electrical circuit module included with the DC supply,

load resistor, and capacitor to model the self-oscillation characteristics and coupling dynamics in NbO_x devices.

A threshold switching model based on a thermally-driven and filamentary insulator-to-metal phase transition in NbO_2 was first established by Pickett and Willams in 2012 [37]. The analytical model assumes a NbO_2 volume is formed after the initial electroforming process. A metallic core with high conductivity is formed once a fraction of the NbO_2 volume is Joule-heated above the MIT transition temperature of ∼1070 K which lead to an abrupt reduction in device resistance. Although the analytical simulation in SPICE shows good agreement with the general non-linear behaviour of the experimental data, it is unable to adequately describe the threshold switching characteristics of our measurements. Therefore, a finite element model based the thermally-driven MIT was developed to address these limitations.

Recently, an alternative conduction mechanism based on the bulk-limited Poole-Frenkel (P-F) emission with a combination of exponential electric field and temperature dependence has been proposed to explain the threshold switching effect in NbO_x [69, 172, 173]. The threshold switching response is attributed to a localised thermal runaway process which is associated with a significant increase in filament current and temperature. There is growing concensus that P-F conduction can account for the switching behaviour, but the recent direct-temperature mapping study has demonstrated the switching process is more complicated. The existence of two distinct negative differential resistance regions was observed with one attributed to a P-F conduction (∼400 K) and the other to a Mott MIT (∼1000 K) [170]. The findings suggest that while both mechanisms can result in threshold switching, the P-F conduction with transition temperature ∼400 K is of primary interest for low-temperature threshold switching. A P-F type numerical model based on the finite element method was also explored.

Chapter 4

Physical and Electrical Characterisations of NbO_x Thin Films

4.1 Introduction

This chapter reports the physical properties of NbO_x thin films and illustrate the range of electrical behaviour of interest in this thesis. NbO_x samples were characterised using atomic force microscopy (AFM) and grazing incident X-ray diffraction (GIXRD) was deployed to characterise the physical structures with increasing annealing temperature. The structures and materials of the devices were confirmed with transmission electron microscopy (TEM). Diverse switching responses, including unipolar switching, bipolar switching, self-assembled selector-memory switching, S-type and snap-back current-controlled negative differential resistance (CC-NDR) were observed.

4.2 Experimental details

Two types of NbO_x thin films were prepared in this study. The first set was fabricated by dc reactive sputtering from a Nb metallic target at room temperature with fixed argon-to-oxygen gas mixture in the ratio range between 19/1 (5 % O_2) and 17.5/2.5 (12.5 % O_2). The total gas flow was maintained at 20 sccm and the deposition was

performed with a constant DC power of 150 W and a working chamber pressure of 4 mTorr. The second set was deposited using RF magnetron sputtering from a Nb_2O_5 target with 20 sccm Ar gas flow and rf power of 300 W. Different substrate and device structures were fabricated for testing purposes and the specific fabrication details are described in each Section. All depositions were performed with the substrate at room temperature.

4.3 Microstructure analysis

4.3.1 Surface morphology

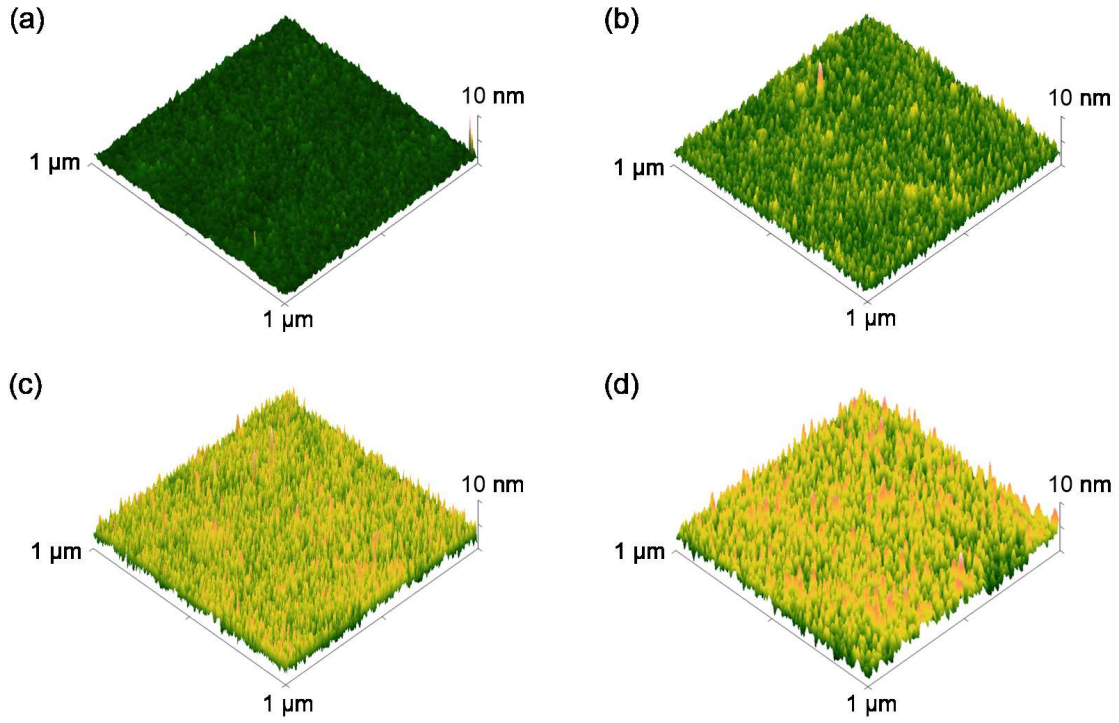

Figure 4.1: 3D AFM topography maps of (a) 20 nm (b) 30 nm (c) 40 nm (d) 50 nm as-deposited NbO_x thin films on $TiN/SiO_2/Si$ substrate.

Surface roughness is an important parameter in device fabrication and can have a direct impact on the oxide breakdown and switching characteristics [189]. The surface topography of DC reactive sputtered (Ar/O_2:17.5/2.5) NbO_x thin films on

TiN/Si substrate was characterised using an atomic force microscopy (AFM). The AFM topography scans were performed as a function of oxide thickness over 1 μm^2 selected areas in different locations. The quantitative analysis of the oxide surface topography is illustrated in Fig. 4.1 from the thinnest 20 nm layer (Fig. 4.1(a)) to the thickest 50 nm (Fig. 4.1(d)). It is observed that the oxide becomes rougher with increasing film thickness. The dependence between the roughness and the oxide thickness of NbO_x films is confirmed and more clearly illustrated in Fig. 4.2(a). The plot shows the root mean square (RMS) roughness as a function of NbO_x thin-film thickness and benchmarked with the TiN bottom electrode RMS roughness. The NbO_x film is observed to undergo a 40% increase from 0.75 nm (20 nm thickness) to 1.05 nm (50 nm thickness) in RMS roughness. In comparison, the TiN bottom electrode was measured to have a mean RMS roughness of 0.68 nm. The measured peak height distribution of the NbO_x film surface is shown in Fig. 4.2(b). The peak height is calculated between the lowest and the highest points on the surface. The results show that the peak height distribution is broadened with the increasing film thickness.

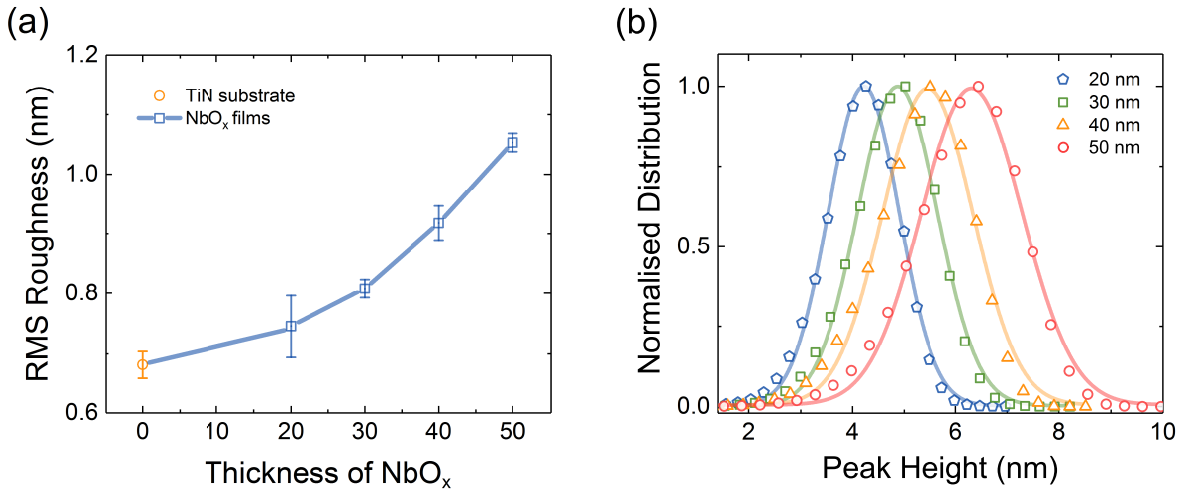

Figure 4.2: (a) RMS roughness of the TiN bottom electrode and NbO_x thin films as a function of thickness. The error bars represent the standard deviation from scans of 3 different locations for each film thickness. (b) Peak height distribution for each film thickness.

4.3.2 X-ray diffraction

The structural analysis and thermal stability of the sub-stoichiometric NbO_x and stoichiometric Nb_2O_5 thin films at different annealing temperature was investigated by using a grazing incidence X-ray diffraction (GIXRD) as shown in Fig. 4.3. The DC reactive sputtered (Ar/O_2:18/2) NbO_x and RF sputtered Nb_2O_5 films were deposited on a (100) oriented silicon substrates at room temperature. Samples were subjected to a rapid thermal anneal at a temperature from 300 ^{o}C to 600 ^{o}C for 5 minutes under 500 sccm Ar gas flow. For the as-deposited films, the films exhibit a broad peak. The absence of diffraction peaks from the samples confirms the amorphous nature of the films. After thermal anneal at 300 ^{o}C, 400 ^{o}C and 500 ^{o}C, the NbO_x films remained amorphous as no distinct diffraction peaks were noted. Crystallisation in the NbO_x and Nb_2O_5 films was observed at 600 ^{o}C with diffraction peaks corresponding to the formation of pseudohexagonal TT-Nb_2O_5. A weak diffraction peak is observed in the GIXRD patterns of the Nb_2O_5 films as shown in Fig. 4.3(b). This peak corresponds to the Si (100) phase from the substrate due to the thinner Nb_2O_5 films.

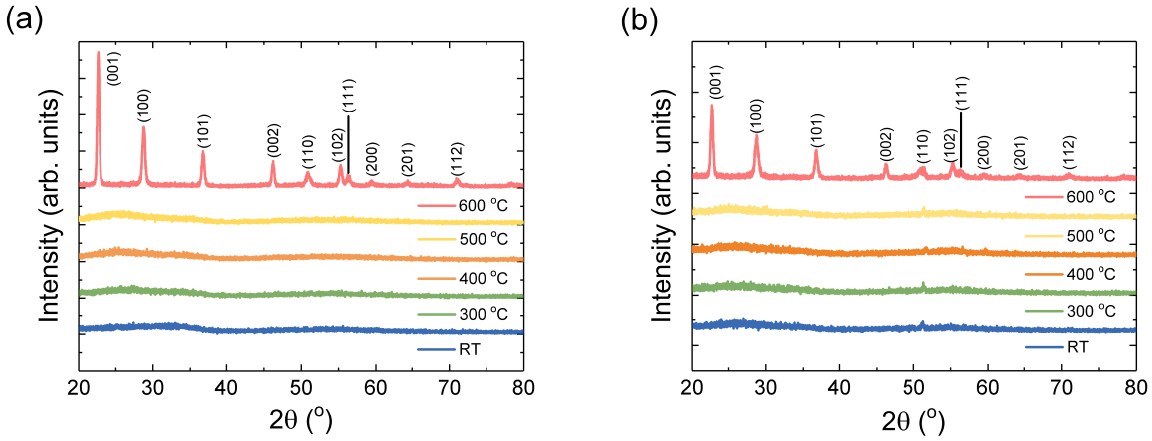

Figure 4.3: (a) GIXRD patterns of the DC reactively sputtered NbO_x thin films as a function of temperature. (b) GIXRD patterns of the RF sputtered Nb_2O_5 thin films as a function of temperature.

4.3.3 Stoichiometry analysis

Rutherford backscattering spectrometry (RBS) measurements were performed by 2 MeV He^+ ions for the NbO_x thin film samples deposited on carbon substrates. Two types of samples were prepared for the stoichiometric measurements. The first set were grown by DC reactive sputtering from a Nb metallic target with O_2 flow ratio varied between 6.25 % and 12.5 %. The second series used RF sputtering from a stoichiometric Nb_2O_5 target. Films were deposited onto carbon substrates which enables direct analysis of O and Nb ratios. The backscattered ions were detected at a scattering angle of 165 ^{o} in high vacuum with a base pressure of 2×10^{-7} Torr.

Fig. 4.4 displays the representative measured (black) and simulated (red) RBS spectra for NbO_x films DC reactively sputtered at different argon-oxygen ratios. The front edges of the oxygen and niobium peaks are marked with blue arrows. The simulated curves in the RUMP software shows good agreement with the experimental results. The NbO_x composition (O/Nb) is plotted as a function of the oxygen content as shown in Fig. 4.5. An increase in oxygen content from 6.25 % to 12.5 % leads to a rise in O/Nb ratio from 2.05±0.02 to 2.87±0.03. The results show that

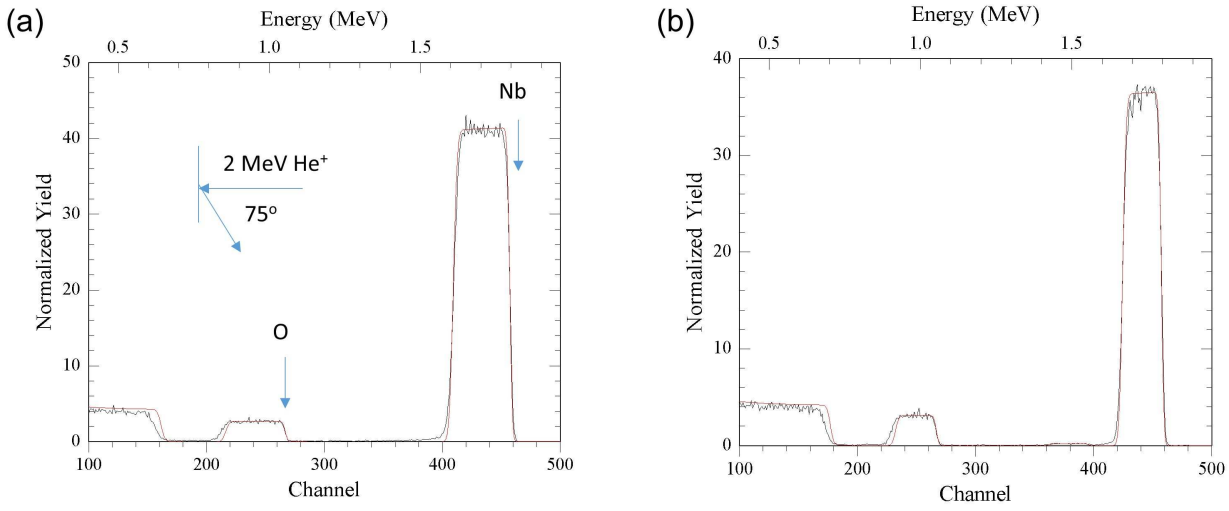

Figure 4.4: Representative RBS spectra obtained from the DC reactively sputtered NbO_x thin film samples with different oxygen content: (a) 6.25 % (b) 12.5 %.

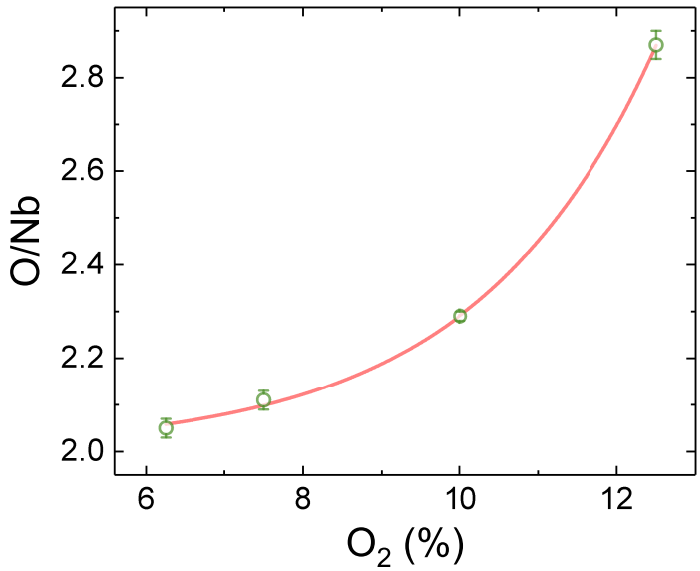

Figure 4.5: Niobium to oxygen ratio as a function of oxygen content.

the NbO_x stoichiometry is very sensitive to the available oxygen during the deposition process and has an exponential dependence to the oxygen content within the examined percentage. The RF sputtered NbO_x sample was analysed and obtained with O/Nb ratio of 2.54±0.02 which is near-stoichiometric composition to Nb_2O_5.

4.3.4 Transmission electron microscopy

Three devices structures, including Pt/Ti/NbO_x/Pt, Pt/NbO_x/TiN, and Pt/Nb_2O_5/Nb/Pt, employed in this study for TEM cross section characterisation to confirm the device layers and physical structure of the oxide.

Fig. 4.6(a) shows a Pt/Ti/NbO_x/Pt structure fabricated on plasma-enhanced chemical vapour deposited (PECVD) Si_3N_4. The thickness of the NbO_x thin films were confirmed in TEM to be ∼75 nm and deposited by reactive dc magnetron sputtering from a Nb metallic target with stoichiometry controlled by the ratio of argon to oxygen (18/2 sccm). The 50 nm Pt bottom electrode (Pt) and Ti (∼10 nm)/Pt (50 nm) top electrode were prepared by electron-beam (e-beam) evapor-

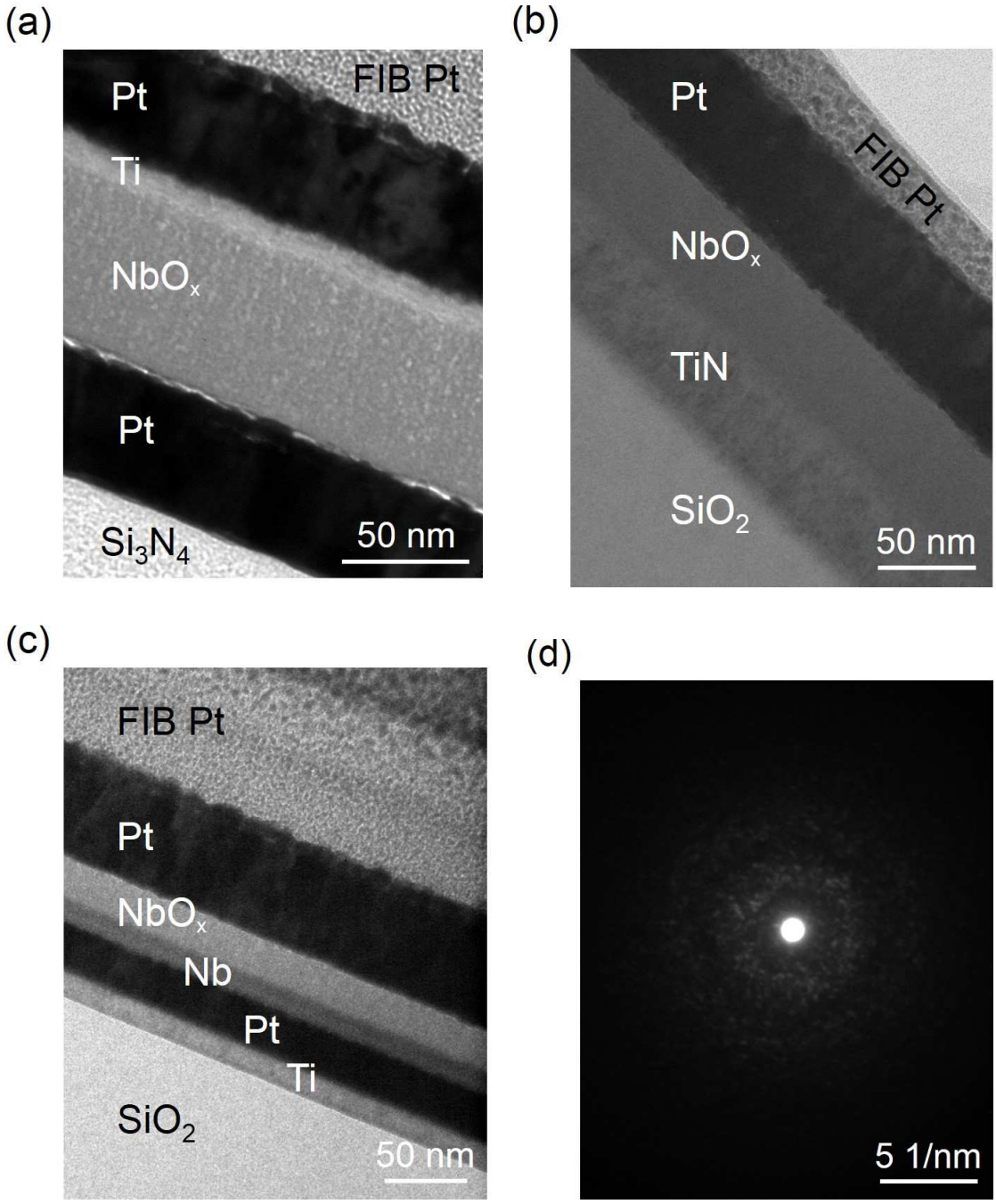

Figure 4.6: Representative bright-field TEM images of NbO_x device cross sections with different test structures (a) Device with $Pt/Ti/NbO_x/Pt$ structures on Si/Si_3N_4 substrate. (b) TEM bright field image of $Pt/NbO_x/TiN$ device structures on Si/SiO_2 substrate. (c) Cross sectional TEM bright field image of $Pt/Nb_2O_5/Nb/Pt$ structures with a Ti adhesion layer on Si/Si_3N_4 substrate. (d) Electron diffraction of NbO_x thin films within the device structures.

ator. The fabricated devices were subject to a rapid thermal annealing at 300 ^{o}C for 5 min before electrical measurements were performed and the annealed NbO_x films confirmed to be amorphous by XRD in Section 4.3.2.

The TEM image of Fig. 4.6(b) was taken from a cross section of a Pt/NbO_x/TiN device structure on thermally oxidized Si wafer. The DC reactive sputtered NbO_x layer (Ar/O_2:17.5/2.5) has stoichiometry near Nb_2O_5, with sputtered TiN (50 nm) bottom electrode and e-beam deposited Pt (50 nm) top electrode. The NbO_x layer was confirmed to be amorphous by selected area diffraction as shown in Fig. 4.6(d).

Devices with a multi-stack structure of Pt/Nb_2O_5/Nb/Pt were fabricated on thermally oxidized Si wafer with a 10 nm Ti wetting layer as shown in Fig. 4.6(c). The Nb_2O_5 thin films were rf sputtered from a stoichiometric Nb_2O_5 oxide target under 20 sccm Ar gas flow. A Si_3N_4 encapsulation layer was deposited on the room-temperature-fabricated devices at 300^{o}C for 2 min in a vacuum chamber to enhance layer contacts and minimise the effect of the ambient environment. In the post-annealed devices, an additional NbO_x layer with 5 nm thickness was observed at the Nb_2O_5/Nb interface. The initial Nb layer was reduced from 10 nm to 5 nm.

4.4 Switching behaviour in NbO_x

This section provides an overview of the switching behaviour observed in NbO_x based metal-insulator-metal (MIM) devices. All devices were subjected to an electroforming process before operation. The switching responses can be generally classified into six switching modes: unipolar resistive switching, bipolar resistive switching, threshold switching, self-assembled threshold-memory switching, co-existence of threshold and memory switching, and co-existence of S-type smooth and abrupt box-like NDRs in various device structures.

Unipolar switching is generally observed in NbO_x devices with inert top and bottom electrodes as used in the present study. In this case, the unipolar switching devices employed a Pt/NbO_x/Pt device structure. The 30 nm NbO_x layer was

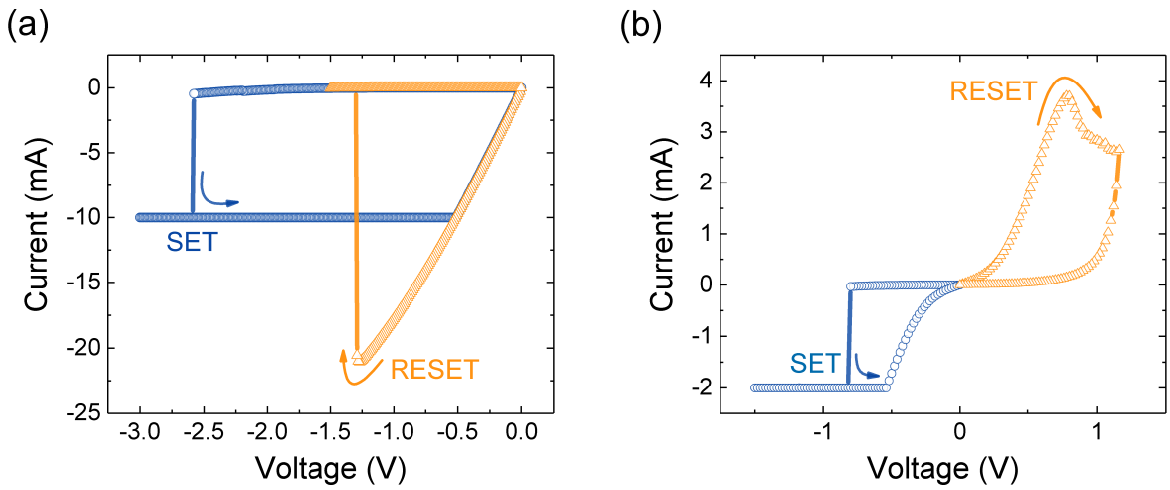

Figure 4.7: (a) I-V characteristics of unipolar switching in Pt/NbO_x/Pt device structures. (b) I-V characteristics of bipolar switching in Pt/Nb/NbO_x/Pt device structures.

dc reactively sputtered with Ar/O_2 gas ratio of 18/2. The typical switching behaviour is illustrated in Fig. 4.7(a) where the SET and RESET operations were performed independent of voltage polarity. The thermal-dominated mechanism in unipolar switching requires a larger SET voltage in comparison to RESET operation. However, a higher RESET current is needed to abruptly dissolve the conduction filament.

Fig. 4.7(b) shows typical bipolar switching characteristics with Pt/Nb/NbO_x/Pt device stacks. The NbO_x films were prepared by RF sputtering of a Nb_2O_5 target and have a thickness of 20 nm. As discussed in Section 2.5.2, bipolar switching in NbO_x can be achieved by introducing a reactive metal to create inhomogeneous oxygen concentration within the device stacks. A 10 nm Nb reactive top electrode was deposited in this case to form an oxygen exchange layer. During operation, the device was SET into the low resistance state with a negative bias and can only be RESET back to the high resistance state in the positive polarity. The polarity dependent resistive switching behaviour is attributed to an electric field driven ion migration.

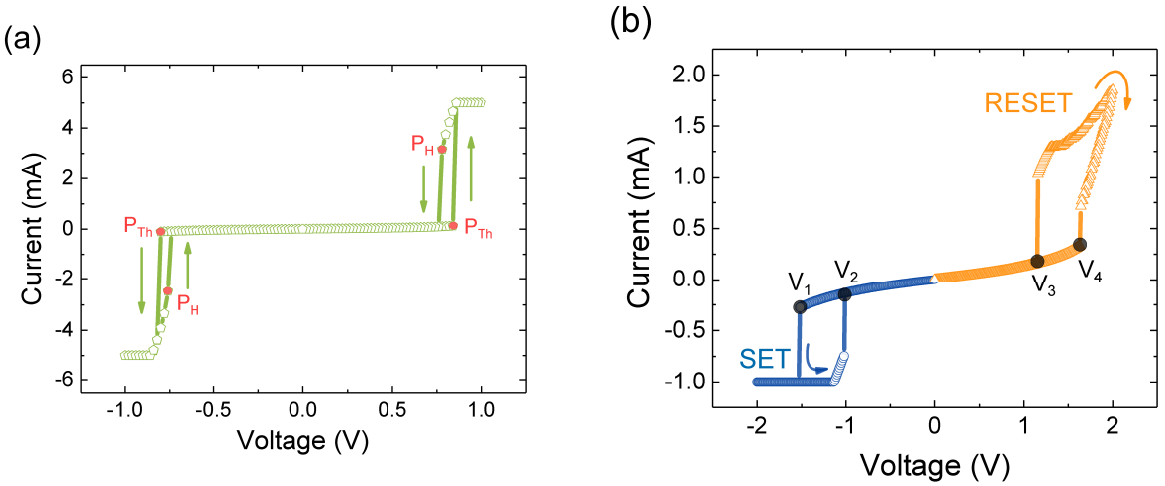

Figure 4.8: (a) Threshold switching characteristics in Pt/Ti/NbO_x/Pt device structures. (b) Self-assembled threshold-memory switching behaviour in Pt/NbO_x/TiN devices.

Volatile symmetric threshold switching was observed without any memory effect in devices with a Pt/Ti/NbO_x/Pt structure as shown in Fig. 4.8(a). In this case, the amorphous NbO_x layer was deposited by reactive sputtering of metallic Nb in gas mixture of Ar/O_2:18/2. Threshold switching was initiated by a forming process that consisted of scanning the voltage on the top electrode from 0 to -8 V with 20 mA compliance current. After the forming process, reproducible threshold switching behaviour was observed during DC voltage scans in the range -2 V to +2 V. The resistance of the device is observed to switch from a high resistance state to a low resistance state above the critical threshold point (P_{Th}). Based on the Arrhenius plot of the device resistance in Fig. 5.15(b), the high and low resistance states are referred as insulating and metallic states for the context of the studies in the remaining thesis. When the voltage is subsequently reduced below the hold point (P_H), the resistance of the device reverts back to the high resistance state. The device showed stable switching and good reliability over the course of 500 switching cycles.

A self-assembled threshold-memory switching response, which is a series combin-

ation of the threshold switching and memory elements, was found in $Pt/NbO_x/TiN$ devices as shown in Fig. 4.8(b). In this case, the NbO_x thin films were DC reactive sputtered with the argon to oxygen gas ratio of 17.5/2.5. During the initial RESET process after forming, the devices self-assemble into a hybrid threshold-memory structure. For the voltage sweep in the negative polarity, as the applied bias increases to reach V_1, the threshold switching element switches from the insulating state to the metallic state and the memory element simultaneously SET into a low resistance state. As the voltage is reduced to V_2, the threshold switching element reverts back to its insulating state, but the memory element remains in the low resistance state. In order to RESET the memory element, a subsequent voltage sweep in the positive polarity is needed. Once the voltage arrives at V_3, the threshold switch transits to a metallic state. As the voltage is further increased to V_4, the memory element RESETs back to a high resistance state while the threshold switch remains in the metallic state. Such devices also exhibit stable symmetric threshold switching when the memory element is in low resistance state. This is achieved by preventing the memory from being RESET back to a high resistance state. In this case, the

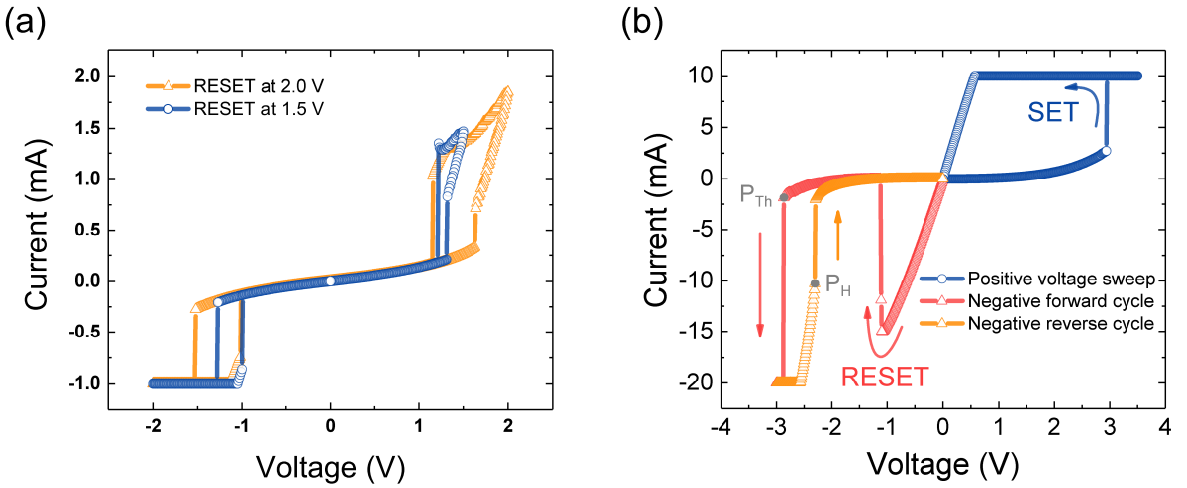

Figure 4.9: (a) I-V charactersitics of the hybrid threshold-memory structure with RESET and SET tuning. (b) Co-existence of unipolar and threshold switching in $Pt/NbO_x/Pt$ devices.

resistance state of the memory component can be tuned by using different RESET voltages as illustrated in Fig. 4.9(a). With larger reset voltages, the gap between the memory filament and the TiN electrode increases. This is reflected in a higher SET voltage immediately following the RESET. The threshold voltage stablises at ±1.0 V after limiting the RESET current to < 1.2 mA.

Fig. 4.9(b) shows a case where both threshold and memory switching behaviour that co-exists within a single device. The devices has the same structure ($Pt/NbO_x/Pt$) as described for the unipolar resistive switching, and was initially SET into a low resistance state (blue coloured) under a voltage controlled sweep. The device can be RESET back to a high resistance with a higher operating current in a lower voltage (red coloured). However, if the voltage scan was further increased after the RESET process, a volatile threshold switching cycle was observed where the device experiences an abrupt reduction in resistance the applied voltage exceeds the threshold point (P_{Th}). Once the applied voltage is reduced below the hold point (P_H), the devices revert back to a high resistance state. After the RESET and threshold switching cycle, the devices still remain in the high resistance state. This co-existence of unipolar and threshold switching can be repeated for several cycles and hasn't been reported elsewhere in the literature. The anatomy of the filament and the underlying mechanism are not still clear. Further experimental characterisations will be needed to further understand the physical origin responsible for this switching behaviour.

Threshold switching devices exhibit negative differential resistance (NDR) under current-controlled sweeps. The NDRs can be classified into two types: S-type smooth NDR and abrupt box-like NDRs. Fig. 4.10(a) shows typical S-type behaviour: the device shows a reduction in voltage once the device current exceeds the threshold point, P_{Th}. The reduction in device voltage saturates at the hold point, P_H and for higher currents the device resistance remains in the metallic resistance state. S-type NDR is commonly observed in NbO_x devices [37,69,172,173,187]. Fig. 4.10(a) shows the co-existence of smooth S-type NDR and abrupt box-like NDRs. As the device

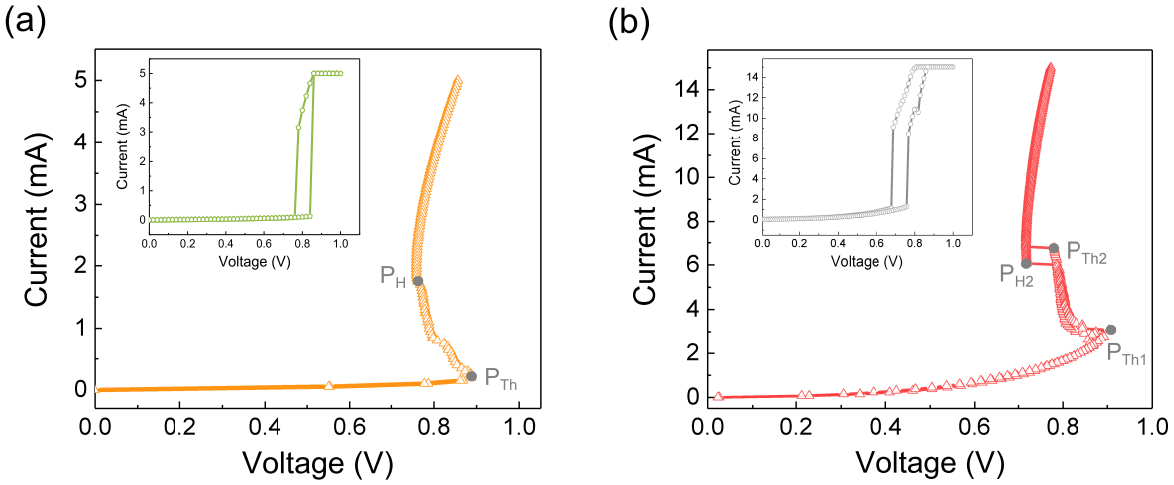

Figure 4.10: (a) A typical current-voltage curve of devices that exhibit S-type negative differential resistance (NDR) under current-controlled sweep. The inset shows the electrical response in voltage-controlled sweep mode. (b) Current-voltage curve of devices that show both S-type smooth NDR and abrupt box-like NDRs.

current increases above P_{Th1}, the voltage starts decreasing. As the device current is further increased up to the second threshold point, P_{Th2}, the voltage shows a sudden reduction and the resistance stabilises in a metallic state. When the device current is reduced below the hold point, P_{H2}, the device shows an abrupt increase in voltage and then followed the current-voltage curve of the S-type NDR back to the high resistance state. Recent direct temperature mapping demonstrated that the S-type NDR is attributed to the Poole-Frenekel conduction with transition temperature ∼400 K while the abrupt box-like NDRs correspond to temperature ∼1000 K which is attributed to a MIT [170].

4.5 Summary

In summary, we have shown that surface morphology of the sputtered NbO_x thin films is relatively smooth with a slight increase in RMS roughness with increasing oxide thickness. XRD analysis confirmed the film remain amorphous up to 500^{o}C anneal. The stoichiometry of the thin oxide films was determined by RBS and TEM

was deployed to confirm the device structures and layer thickness. Electrical response showed that devices exhibit a diverse range of switching behaviours with dependence on sample structure and testing procedure. Unipolar resistive switching is commonly observed in device structure with both inert top and bottom electrodes. Stable bipolar resistive switching, threshold switching and self-assembled threshold-memory effect generally require a reactive electrode to act as an oxygen exchange layer.

Chapter 5

Threshold Switching Anatomy

5.1 Introduction

Threshold switching, or current controlled (S-type) negative differential resistance (CC-NDR) is observed in a range of transition metal oxides (eg., NbO_x, VO_x and TiO_x) [51–53, 57–59, 61–65, 116]. Threshold switching devices exhibit a change in electrical conductivity from an insulating state to a metallic state under external stimulus. The metallic state is only sustained with sufficient current flow and reverts back to its insulating state when the external excitation is removed.

One of the technological interests in such behaviour is to utilise the nonlinear response in resistive random access memory (ReRAM) crossbar arrays. ReRAM devices with a simple MIM structure is a promising candidate for future non-volatile memory technology [95, 190, 191]. ReRAM devices exhibit excellent switching performance, but a passive array of such devices encounters a fundamental drawback called sneak-path problem. The sneak-path problem is caused by parasitic current flowing through unselected memory cells that are in low resistance state and can limit the crossbar array size and create reading and writing errors [192–194]. In order to overcome this shortcoming, one of the simplest and promising options is to integrate a ReRAM device in series with a threshold switching device, also known as selector [36, 195]. The highly nonlinear threshold switching response of the selector devices allow leakage currents in cells at subthreshold voltages to be suppressed and enable unambiguous memory cell addressing at voltages above the threshold value [50, 196, 197].

Threshold switching devices have also been shown to be an effective way to emulate certain properties of a biological neural network based on the self-oscillation behaviour. Important nerual and neural-network functions have recently been demonstrated, including synchronisation of coupled oscillatory systems, chaotic oscillations and generation of action potential in a neuristor, on a single- or coupled-device level for applications in neuromorphic computing [18,41,46,47,144]. This hardware-based approach to neuromorphic computing has the potential to provide systems with low power consumption, adaptive learning capability, high fault tolerance and massive parallel processing power.

The physical origin of threshold switching in amorphous NbO_x thin films remains under debate, with two fundamental mechanisms receiving particular attention in recent studies, namely: Poole-Frenkel (PF) conduction and a metal-insulator transition (MIT) [37,69,172,173,187]. The former relies on trap-mediated carrier transport and is applicable to both crystalline and amorphous oxides, while the latter is generally attributed to a thermally induced metal-insulator transition in NbO_2 that is associated with a specific Mott-Peierls transition, from a distorted rutile structure to a regular rutile structure, at temperatures around 1070 K [66–68]. Although this MIT is not expected in amorphous films, studies have shown that NbO_2 can nucleate within these film during electroforming at high compliance currents [69]. Direct-temperature mapping has also recently been used to identify two distinct threshold switching regimes in a single device, one corresponding to temperatures ∼400 K and attributed to PF conduction, and a second corresponding to temperature ∼1000 K and attributed to a MIT [170]. While this suggests that both mechanisms can play a role, the lower temperature PF regime is of primary interest for low current, low power device operation.

In this chapter, we investigate the threshold switching characteristics of $Pt/NbO_x/TiN$ devices as a function of device area and NbO_x layer thickness, and use these results to understand the anatomy of the switching region. To test the veracity of the deduced structure, the experimental data is compared with predic-

tions of a simple resistor network model and with more detailed finite-element simulations. The threshold switching characteristics of the microscale devices are also compared with the nanoscale devices. Furthermore, the devices' threshold switching response is subsequently studied as a function of temperature to provide insight into the dominant conduction mechanism.

5.2 Experimental details

Devices used in this study consisted of MIM capacitor structures, fabricated by successive layer deposition. Bottom electrodes consisted of 50 nm thick TiN layers, sputter deposited onto thermally oxidized (500 nm SiO_2) (100) Si wafers (supplied by Hionix). NbO_x films of various thicknesses (20 nm to 60 nm) were subsequently deposited by reactive sputter deposition. This was undertaken by DC sputtering of a Nb metal target in an Ar/O_2 ambient, using an Ar:O2 gas ratio of 17.5/2.5, a chamber pressure of 4 mTorr and 150 W power. Circular top electrodes with various diameters (15 to 150 μm diameter) were subsequently deposited by electron-beam evaporation with Pt thickness of 50 nm.

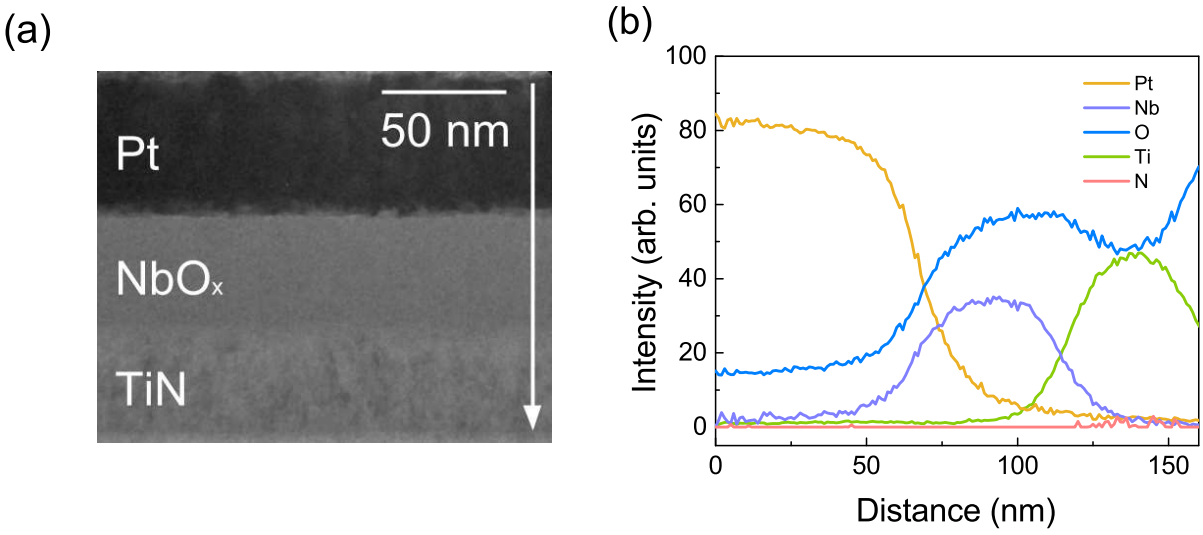

Figure 5.1: (a) A TEM cross section of the fabricated $Pt/NbO_x/TiN$ devices. (b) A representative EDX line scan of the device with corresponding element profiles.

A transmission electron microscope (TEM) image of a device with a 50 nm NbO_x film is shown in Fig. 5.1(a)(a), together with an energy dispersive X-ray spectroscopy (EDX) line scan of the structure shown in Fig. 5.1(b). The deposited NbO_x films were found to have a stoichiometry near Nb_2O_5 (i.e. x=2.5) as determined by the Rutherford backscattering spectrometry, and were amorphous, as confirmed by electron diffraction in TEM. It is important to note that the niobium-oxide system has been extensively studied and, like many other oxides, its physical properties are strongly affected by the precise stoichiometry. For example, the electrical conductivity of Nb_2O_5 have been shown to vary over 7 orders of magnitude from 10^{-13} to 10^{-6} S/m, with small deviations in stoichiometry [151–155].

5.3 Electrical switching behaviour

As-fabricated devices were initially in a high resistance state and an electroforming process was required to initiate threshold switching. This was achieved by applying a negative voltage to the top electrode, using a 2 kΩ series resistor and a current compliance of 4 mA to prevent permanent breakdown. Electroforming was observed

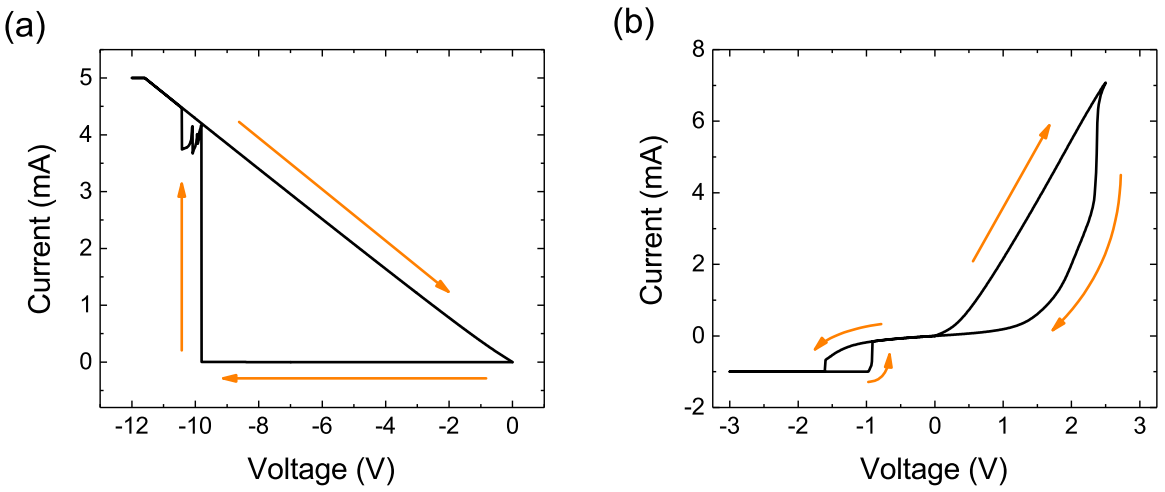

Figure 5.2: (a) Initial electroforming process for the Pt/NbO_x/TiN devices (b) The first RESET/SET cycle after forming process.

at a critical electric field of ∼2.5 MV/cm, and set devices into a non-volatile, low resistance state (LRS) with near-metallic conductivity as shown in Fig. 5.2(a). The devices can be reset back to a high resistance state by applying a voltage sweep in the opposite polarity as shown in Fig. 5.2(b). During subsequent SET/RESET cycles the devices exhibit a hybrid 1S1R response, with typical I-V characteristics as shown in Fig. 5.3(a). The forming process permanently modified the initial device resistance for an initial value of the order of $\sim 10^9$ Ω before forming to the order of $\sim 10^3$ Ω after forming and reset operations. This has previously been attributed to self-assembly of an interlayer at the oxide/electrode interface, with the filament acting as a virtual cathode for threshold switching within the interlayer [198].

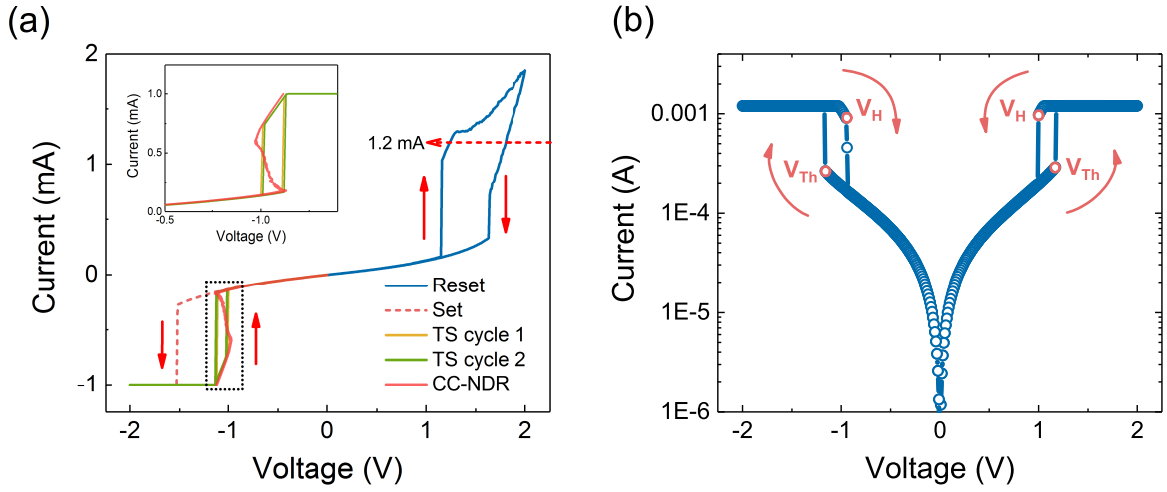

Figure 5.3: (a) Evolution of the device I-V response, from a hybrid selector-memory response to threshold switching response. Stable threshold switching (TS) and current-controlled NDR (CC-NDR) are observed in the negative polarity after the memory element is SET to a LRS. The inset shows the threshold switching response under both voltage and current controlled sweep modes. (b) Symmetric volatile threshold switching with 1.2 mA compliance current.

The RESET cycle of the 1S1R behavior is highlighted with blue colored solid line in Fig. 5.3(a). When the voltage reaches the threshold point, the threshold switching layer switches from an insulating state to a metallic state, causing a sudden increase in current. Increasing the voltage further causes the memory filament to

RESET to a HRS, the resistance of which can be finely tuned by varying the reset voltage as shown in Fig. 5.4. As the voltage is then reduced from its maximum, the device initially exhibits near-Ohmic behavior, reflecting the HRS of the memory element, before exhibiting a sudden increase in resistance (decrease in current) as the threshold element switches back to its insulating state. Significantly, the resistance at sub-threshold voltages is similar before and after the RESET event, suggesting that it is dominated by the resistance of the volatile threshold element. For a subsequent SET cycle (red colored dash line), negative voltages are applied to the top electrode. This results in a simultaneous SET and threshold switching event at around -1.5V. The volatile threshold switch then reverts to its insulating state as the voltage is reduced below the hold voltage. A detailed explanation of such 1S1R behavior can be found in our earlier study [198].

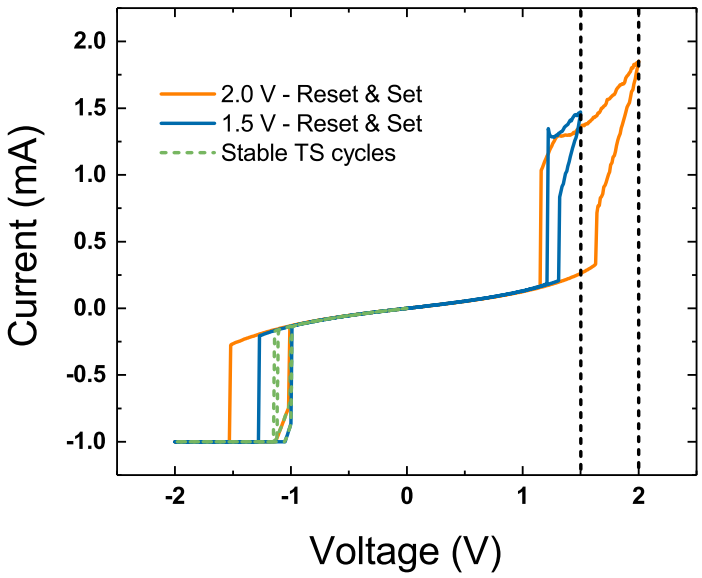

Figure 5.4: I-V charactersitics of the integrated selector-memory structure. The resistance state of the memory component can be tuned by using different reset voltages. With larger reset voltages, the gap between the memory filament and the TiN electrode increases. This is reflected in a higher set voltage immediately following the RESET. The threshold voltage stablises $\sim \pm 1.0$ V.

The devices show stable and uniform symmetric threshold switching when the

non-volatile memory element is maintained in its LRS. This is realized by applying a negative voltage sweep to SET the memory element into a LRS, and then limiting the current ≤ 1.2 mA during subsequent positive voltage sweeps to prevent the memory element from being RESET back to a HRS. The inset in Fig. 5.3(a) shows the stable threshold switching under both voltage and current controlled sweep modes, where the slight difference in hold voltage is due to the variation of sweep rate between the two modes. Fig. 5.3(b) shows typical symmetric threshold switching I-V characteristics. The devices experience a sudden reduction in resistance when the applied voltage exceeds the threshold voltage, V_{Th}, in either polarity. The metallic state is volatile, and is only sustained while the voltage exceeds the hold voltage, V_{Th}. Once the applied voltage is reduced below the hold voltage, the devices revert back to their insulating state. Since the LRS of the memory element shows metal-like conductivity, it can be regarded as a temperature-independent resistor whose value depends only on the oxide film thickness.

5.4 Device area dependence

The effect of device area on threshold switching characteristics was studied for top electrode sizes ranging from 15 μm to 150 μm diameter, and for a fixed Nb_2O_5 layer thickness of 50 nm. The initial electroforming voltage, and switching characteristics were found to be independent of device area which is consistent with a filamentary conduction mechanism. The effect of device area on the threshold voltage (V_{th}) and hold voltage (V_{th}) is summarized in Fig. 5.5(a), and shows that their mean values also remain relatively constant at -1.0 V and -0.9 V, respectively. The corresponding threshold switching power (i.e. $P_{th} = I_{th}V_{th}$) is shown in Fig. 5.5(b), and is also found to be independent of electrode area. The measured mean threshold power in our micro-size devices is ~66 µW, which is of the same order of magnitude as that reported for nano-size devices with electrode contacts of ranging from 50 to 200 nm diameter [69, 173, 199]. The independence of device area is also applied

to both the insulating- and metallic-state resistances of the device. The measured mean insulating-state resistance is ∼66 kΩ and the metallic-state resistance is ∼200 Ω. These observations confirm that threshold switching occurs within a laterally confined region of the device, and suggest that this region has dimensions $\leq 10^{-7}$ m.

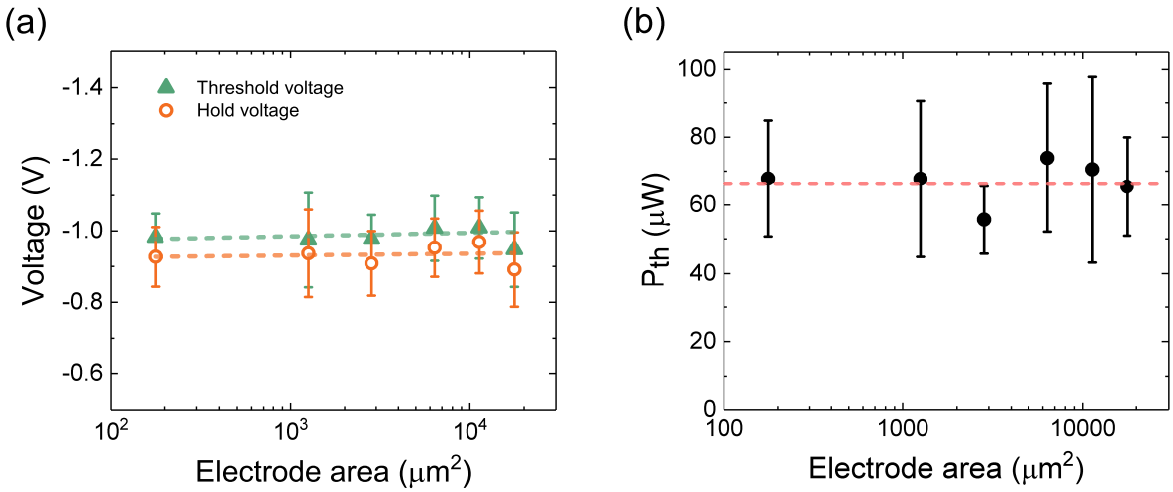

Figure 5.5: (a) Threshold voltage and hold voltages as a function of top electrode area. (b) Threshold power as a function of top electrode area. The error bar heights represent the standard deviation over >7 samples for each electrode area.

5.5 NbO_x thickness dependence

The effect of Nb_2O_5 thickness on forming and threshold switching characteristics was studied for film thicknesses in the range from 20 nm to 60 nm with a fixed top electrode diameter of 100 μm. The effect on the forming voltage is shown in Figure 4(a), which shows a linear increase in forming voltage with increasing oxide thickness. This is consistent with field-induced breakdown of the oxide layer at a critical field of 2.5 MV/cm, similar to the behaviour reported for other oxide films [200, 201]. The effect on the threshold voltage, threshold current and hold voltage, is shown in Fig. 5.6(b). These data represent the average values for ten devices of each

thickness, and show that the threshold and hold voltages remain constant with increasing film thickness, while the threshold current decreases monotonically. The invariance of the threshold and hold voltages is interesting as it implies that the thickness of the threshold switching region is independent of film thickness, and is therefore locally confined both laterally and vertically within the device. The 1S1R switching characteristics observed at higher compliance currents further suggests that this switching volume is located between the residual memory filament and the TiN electrode. Interestingly, a recent study of threshold switching in NbO_2 reported that the threshold voltage did depend on the NbO_2 layer thickness. No detailed explanation of this dependence was offered, but since no 1S1R behaviour was reported it is conceivable that threshold switching volume extended through the entire film in this case.

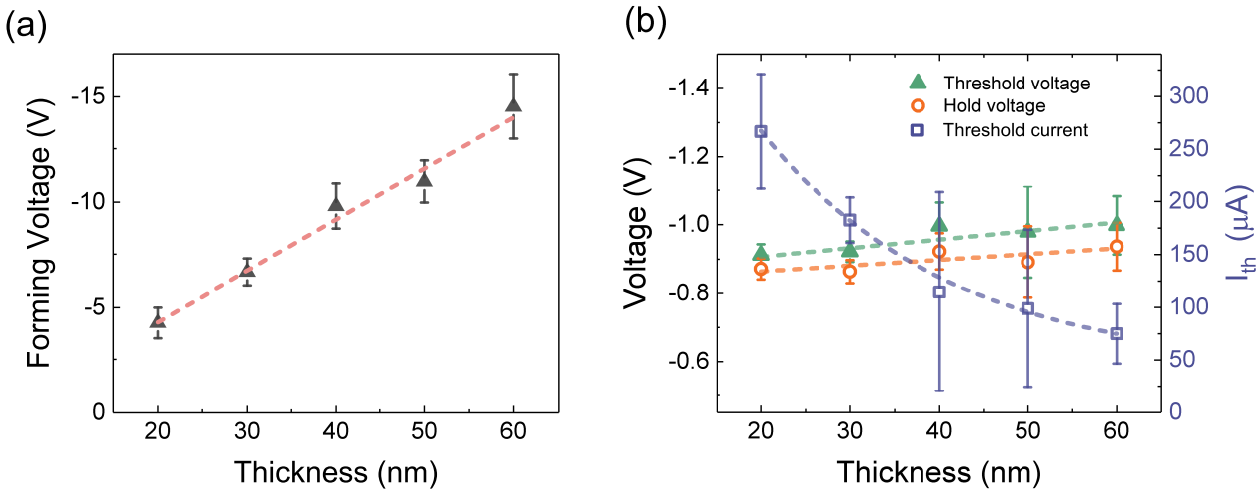

Figure 5.6: (a) Forming voltage as a function of niobium oxide film thickness. (b) Threshold and hold voltages, threshold current as a function of niobium oxide film thickness. The error bar heights represent the standard deviation over >7 samples for each film thickness.

The reduction in mean threshold current with increasing film thickness, from 267 μA for a 20 nm film to 75 μA for a 60 nm film, is particularly interesting as it implies that a significant contribution to the device resistance scales with film thickness. At first sight, this appears to contradict our proposed filamentary model in which

the resistance is dominated by a fixed threshold switching volume at the end of a conductive filament. However, given the nature of the electroforming process, it is expected that the conductive filament will have a graded composition profile with an oxygen vacancy concentration that peaks at its core and decreases radially over some distance. The filament will therefore comprise a metallic core and a semiconducting shell with a conductivity that decreases with increasing distance from the core. We speculate that this semiconducting shell provides a parallel conduction path through the oxide film, and accounts for the thickness dependence of the threshold current.

5.6 Resistor network model

The general veracity of this core/shell model can be assessed by using the simple circuit model shown in Fig. 5.7(a). This uses resistors to represent the threshold switching volume (R_{TS}), the memory core (R_C), the semiconducting shell (R_S) and the surrounding insulating matrix (R_M). From the pre-formed resistance of the device (GΩ), and the area independence of the threshold current, the resistance of the surrounding Nb_2O_5 matrix, R_M, is much higher than that of the active device region and is assumed infinite. The equivalent resistance is then given by:

$$R_{eq} = \frac{(R_{TS} + R_C)\, R_S}{R_S + R_C + R_{TS}} \tag{5.1}$$

and the threshold power by:

$$P_{TS} = \frac{V_{TS}^2\, (R_S + R_C + R_{TS})}{(R_{TS} + R_C)\, R_S} \tag{5.2}$$

To compare this with experimental data we assume that the shell resistance, R_S, varies linearly with film thickness. Based on the device resistance immediately after electroforming where the filament effectively straddles the full film thickness, the memory core resistance, R_C, is further estimated to be in the range 200-500 Ω. Using this insight, Equation (5.2) can be directly compared with the experimental

data which shows a decrease of the mean threshold power from 243 μW to 75 μW for a three-fold thickness increase from 20nm to 60nm, as shown in Fig. 5.7(b). The fitted curve (green colored dash line) assumes R_{TS} = 30 k, R_c = 500 Ω, and an R_S increasing from 4.7 kΩ to 14.1 kΩ as the film increases in thickness from 20 to 60 nm. These values are consistent with the experimental data and demonstrate the plausibility of the core/shell model.

5.7 Numerical simulation

To further test the validity of proposed model, the threshold switching characteristics of two distinct structures were compared using finite element modelling: the first (Model 1) considered a structure where the threshold switching region extended through the entire film, while the second (Model 2) considered a localized switching volume within the proposed core-shell structure. Both models were based on a 50nm Nb_2O_5 film with a 50 nm thick TiN bottom electrode and a 50 nm Pt top electrode, with threshold switching assumed to result from PF conduction due to local Joule-heating. The PF model was based on the high trap-density expression derived by Ielmini et. al. [48], which has the form:

$$J(F,T) = \alpha \exp\left(-\frac{E_a}{k_B T}\right) \sinh\left(\frac{\beta F}{2k_B T}\right) \tag{5.3}$$

where the prefactor, α, depends on the trap density, E_a is the activation energy for carrier hopping, β is a field enhancement factor, F is the local electric field, k_B denotes the Boltzmann constant and T is the temperature. This model was found to reproduce the measured temperature dependence of sub-threshold I-V characteristics of devices. For comparison, simulations were also performed for the MIT mechanisms, in which switching results from a thermally induced Mott transition. The essential simulation details for this mechanism have been discussed in earlier

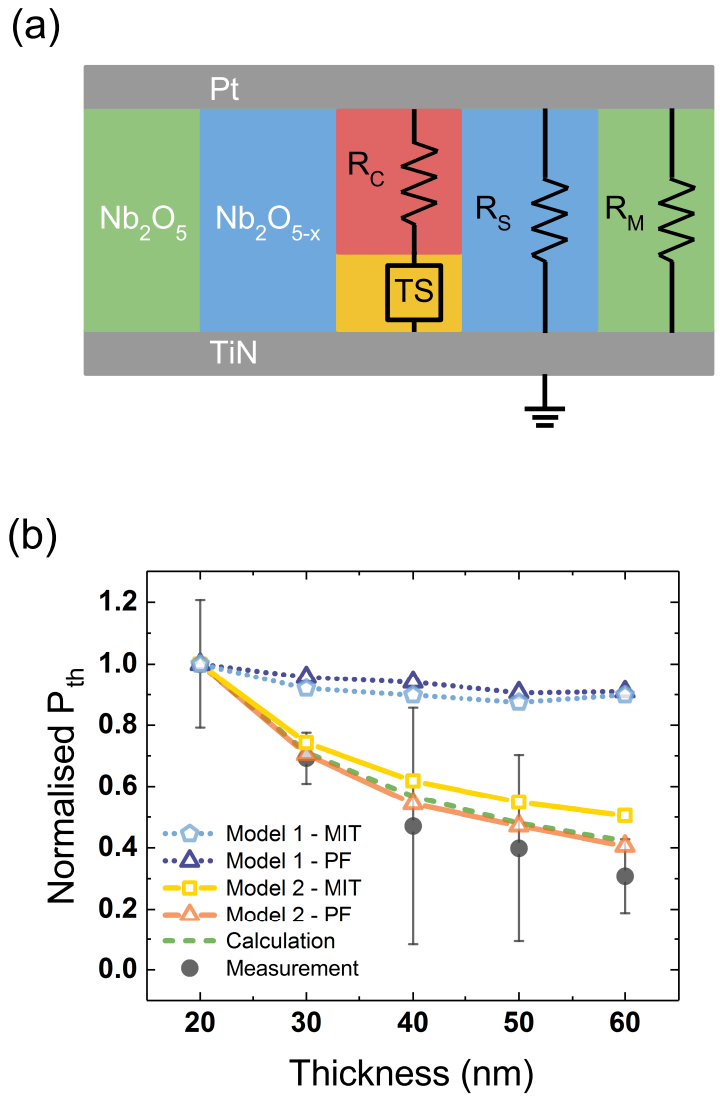

Figure 5.7: (a) Schematic of equivalent circuit model for threshold switching when memory is SET in a LRS. (b) Measured, calculated and simulated threshold power as a function of niobium oxide film thicknesses. The error bar heights represent the standard deviation over >7 measured samples for each film thickness.

work [187, 202].

The device structure for the first model (Model 1) is shown in Fig. 5.8(a), and considered a threshold switching region defined by a cylindrical filament of 50 nm diameter embedded within a surrounding insulating Nb_2O_5 matrix of 600 nm diameter. The second structure (Model 2) is shown in Fig. 5.8(b), and assumed an

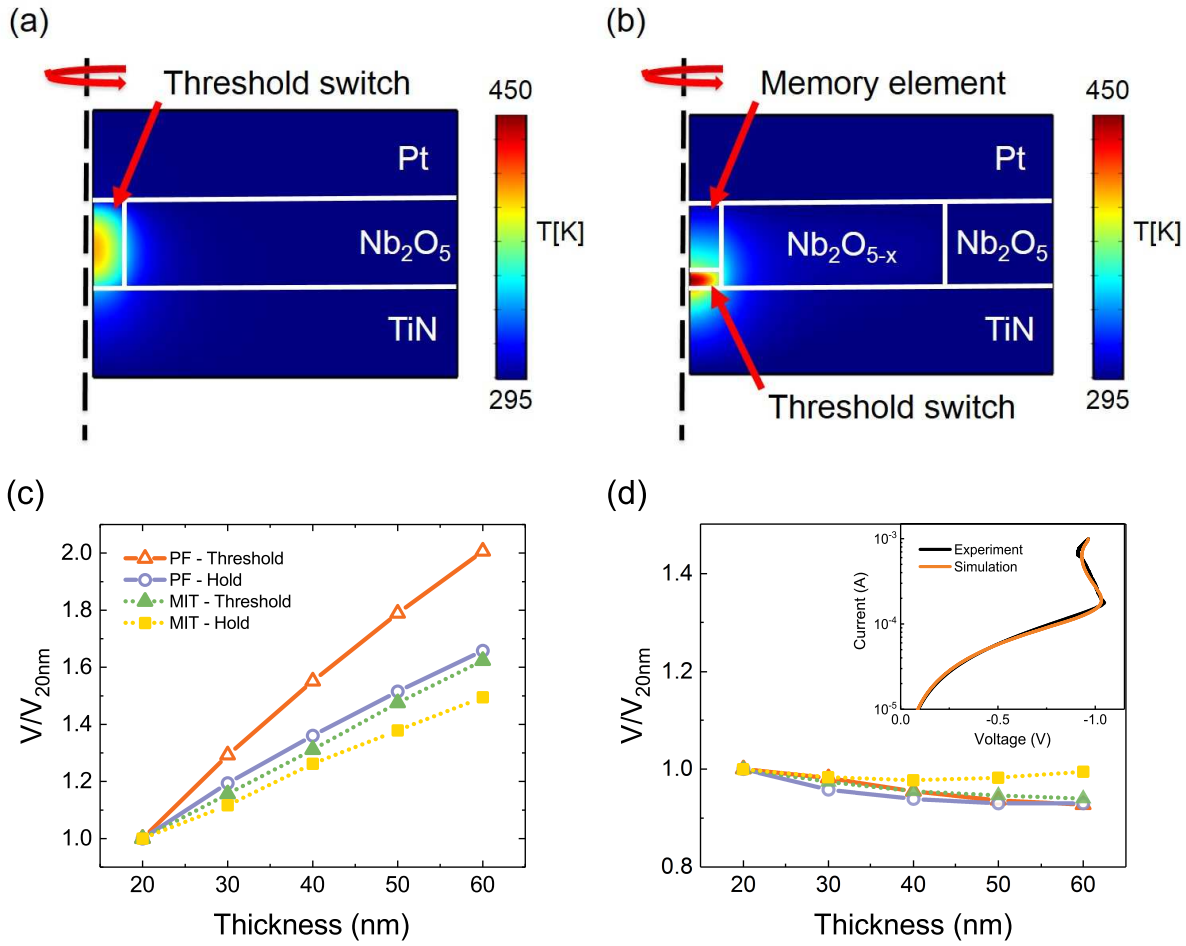

Figure 5.8: (a) Axisymmetric 2D simulation geometry for a MIM structure with a cylindrical threshold-switching volume exhibiting PF-type conduction (1S). (b) Axisymmetric 2D simulation geometry for a MIM structure with a core-shell geometry comprising a cylindrical low-resistance memory element and a fixed threshold switching volume exhibiting PF-type conduction, and a surrounding semiconducting shell also exhibiting PF-type conduction (1S1R). (c) Simulated thickness dependence of the threshold and hold voltages for the 1S model. (d) Simulated thickness dependence of the threshold and hold voltages for the 1S1R model. The inset shows the comparison between the experimental and simulated I-V curves.

integrated 1S1R structure, where the threshold switching volume is represented by a cylindrical volume of 50 nm diameter and length 10 nm, located between a residual conductive filament and the TiN bottom electrode. In addition, the 1S1R structure is surrounded by a semiconducting Nb_2O_{5-X} shell with a diameter of 420

Table 5.1: Key material parameters for the simulation models.

Parameter description	**Symbol**	**Value**
Thermal conductivity of Nb_2O_5	$\kappa_{Nb_2O_5}$	1.0 W m^{-1} K^{-1}
Electrical conductivity of Nb_2O_5	$\sigma_{Nb_2O_5}$	10^{-8} S m^{-1}
Thermal conductivity of the semiconducting shell (Nb_2O_{5-x})	$\kappa_{Nb_2O_{5-x}}$	1.2 W m^{-1} K^{-1}
Electrical conductivity of the semiconducting shell (Nb_2O_{5-x})	$\sigma_{Nb_2O_{5-x}}$	36 S m^{-1}
Thermal conductivity of the memory core (NbO)	κ_{NbO}	10.0 W m^{-1} K^{-1}
Electrical conductivity of the memory core (NbO)	σ_{NbO}	10^5 S m^{-1}
Thermal conductivity of the threshold switching layer ($Nb_2O_{5-\delta}$)	$\kappa_{Nb_2O_{5-\delta}}$	1.5 W m^{-1} K^{-1}
Minimum electrical conductivity of $NbO_{2-\delta}$	σ_{min}	36 S m^{-1}
Maximum electrical conductivity of $NbO_{2-\delta}$	σ_{max}	2×10^4 S m^{-1}
Activation energy of $NbO_{2-\delta}$	E_a	0.25 eV
Ambient temperature	T_{amb}	295 K

nm. The conductivities of the different device areas were adjusted to match measured resistances and reproduce the measured CC-NDR response of devices, as shown in inset in Fig. 5.8(d). The simulation parameters for the 1S and 1S1R models are summarised in Table 5.1.

Fig. 5.8(a) and Fig. 5.8(b) show the simulated temperature distributions within the two device structures during operation at the threshold point. These data show that Joule heating is largely confined to the threshold switching volume, and that threshold switching is initiated at a temperature in the range 400 to 450 K for PF-type conduction. Having matched the measured device characteristics for a 50 nm oxide layer, simulations were then performed for different oxide thicknesses, assuming that the threshold switching volume remained unchanged in the 1S1R

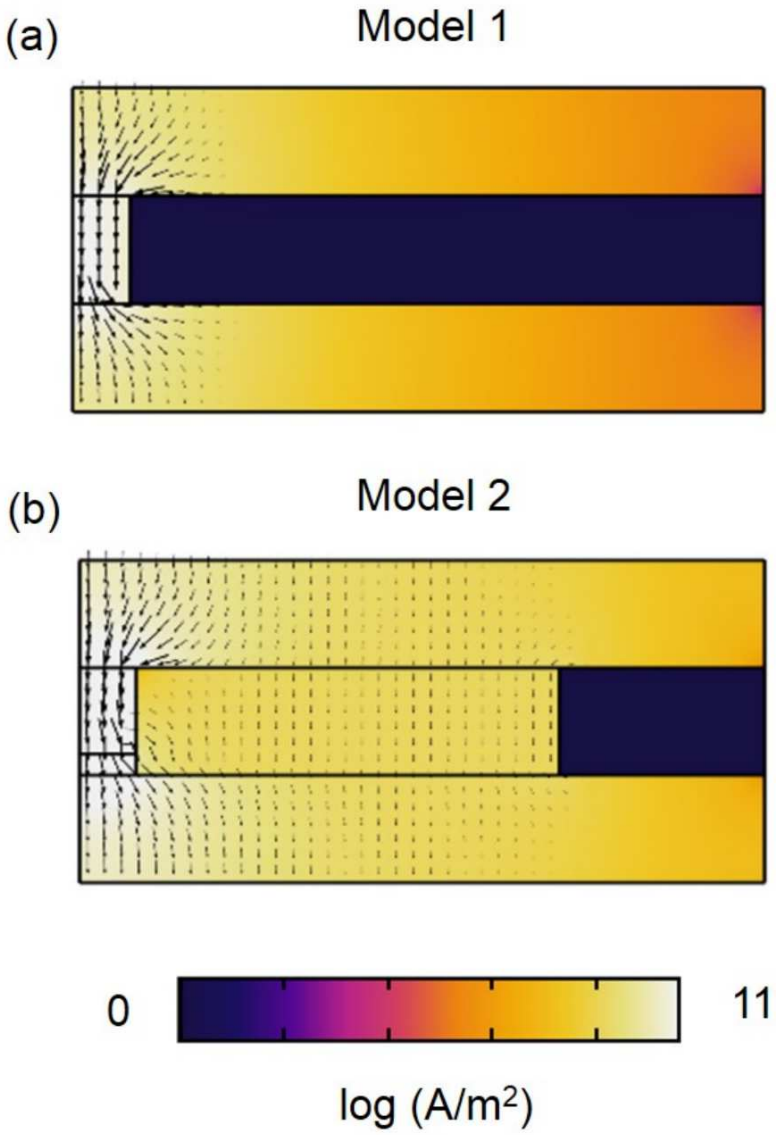

Figure 5.9: (a) Current density of Model 1 (1S structure) at the threshold point. (b) Current density of Model 2 (1S1R structure with semiconducting shell) at the threshold point.

device structure (i.e. only the memory element increased in length in this structure). Materials properties were kept the same for all simulations. The calculated changes in threshold and hold voltages are shown for the 1S (Model 1) and 1S1R (Model 2) structures in Fig. 5.8(c) and Fig. 5.8(d), respectively. Both voltages are observed to increase significantly with increasing film thickness for the 1S structure,

but to remain relatively constant for the 1S1R structures, as observed experimentally (see Fig. 5.6(b)). The simulated threshold power of the 1S structure (Model 1) and the 1S1R structure (Model 2) are shown in Fig. 5.7(b). The 1S1R structure shows a monotonic decrease in the mean threshold power that is consistent with the experimental measurements and the resistor network model. In contrast, the 1S model predicts a near constant threshold switch power. Fig. 5.9(a) and Fig. 5.9(b) shows the simulated device current density at the threshold point. It clearly illustrates the significant parallel leakage current through the semiconducting shell in Model 2 (1S1R) in comparison to Model 1 (1S). This accounts for the reduction in threshold current (power) with increasing thickness of the oxide layer. The proposed 1S1R core-shell structure clearly provides a better match to the experimental data.

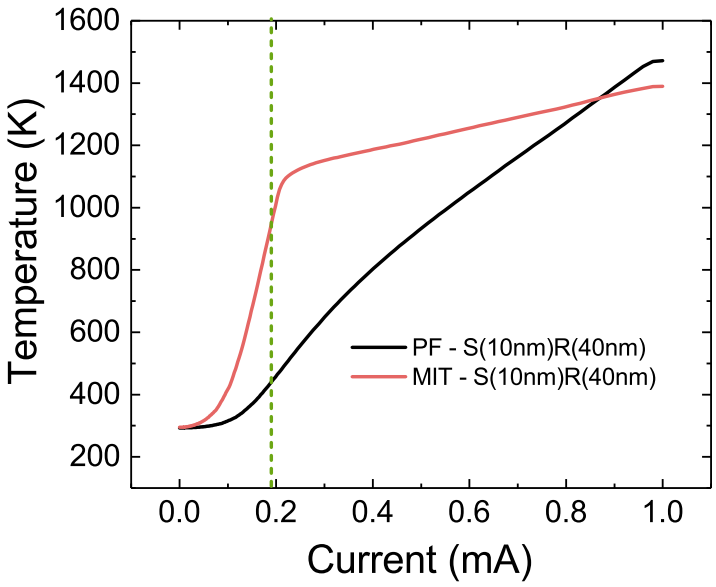

Figure 5.10: Simulated local maximum temperature as function of device current of the CC-NDR response from Model 2 compared between PF-type conduction and MIT mechanism. The structure consists of a filamentary core of 50 nm diameter with threshold switching region and memory element.

Simulations based on the MIT mechanism are included in Fig. 5.7(b) and Fig. 5.8 for comparison, and show that the general behavior is largely independent of the

switching mechanism, even though the onset temperature for the MIT mechanism (∼1070 K) is much higher than that for the PF mechanism (400-450 K). The maximum temperature of the current-controlled negative differential resistance (CC-NDR), compared between PF conduction and MIT mechanism, is shown as a function of device current in Fig. 5.10. The threshold temperature is highlighted with green colored dash line. This reflects the strong positive feedback mechanism associated with the temperature-dependent conductivity change and associated Joule heating.

5.8 Nanoscale device

Nanovia devices with effective electrode size of 400 nm diameter were fabricated in order to compare the threshold switching behaviour in micro-size devices. The devices consist of Pt/NbO_x/TiN structure with 50 nm electrodes and a 50 nm layer of amorphous NbO_x which was deposited by reactively sputtering under the same condition. Threshold switching was initiated by an electroforming process. This consisted of scanning the voltage on the top electrode from 0 to -6 V with compliance current of 300 μA to induce a soft breakdown of the NbO_x film, as shown in Fig. 5.11(a). Devices exhibit stable threshold switching after the subsequent switching cycles at a slightly higher compliance current of 500 μA as shown in Fig. 5.11(b). Repeated current-controlled and voltage-controlled sweeps were performed to confirm the device switching stability and reliability. The I-V characteristics are illustrated in Fig. 5.11(a) and Fig. 5.11(b).

In comparison to the operation of devices with electrode sizes ranging between 15 μm to 150 μm diameter, the nanovia devices require much lower forming power and operating current. The devices exhibit threshold and hold voltages at ∼1.35 V and ∼1.25 V, respectively, which are similar to the micro-size devices and confirmed the formation of a localized threshold switching volume. The nanovia devices show a significant increase in on/off ratio from 10 to 50. A reduction of threshold cur-

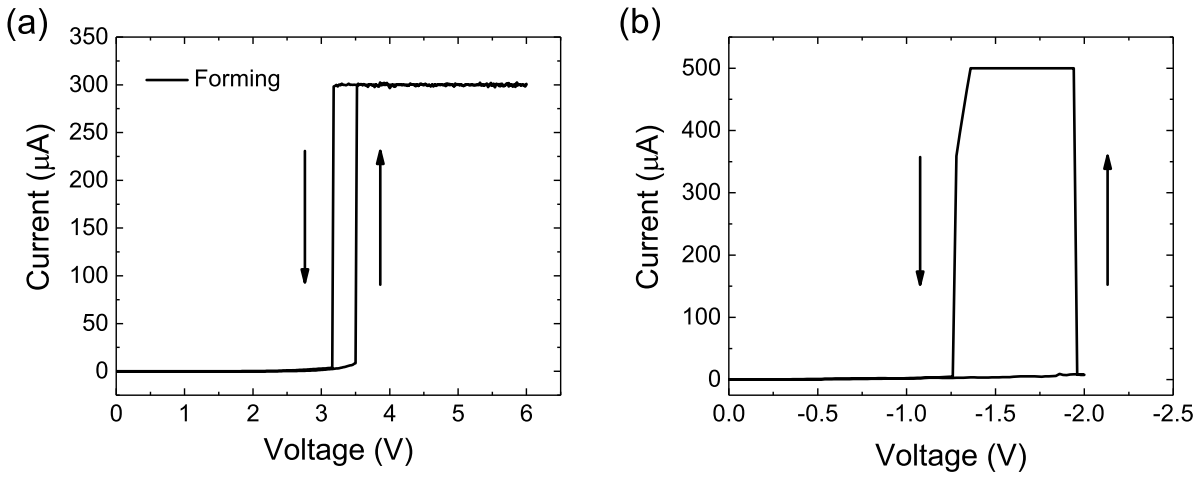

Figure 5.11: (a) Electroforming process for the Pt/NbO_x/TiN nanodevices. (b) Subsequent cycle prior to stable threshold switching.

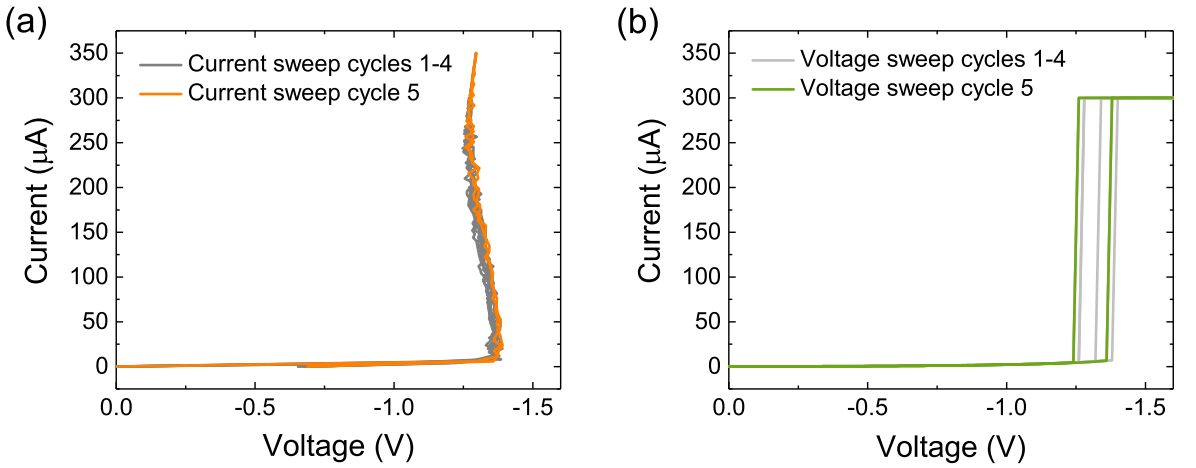

Figure 5.12: (a) I-V characteristics under current-controlled sweep. (b) I-V characteristics under voltage-controlled sweep.

rent (power) is observed with downscaling device area. The decrease in threshold current is attributed to the confinement of parallel leakage current through the semiconducting shell around a filamentary core as the comparable dimension between the nanovia device area and the shell. The nanodevices show improved switching characteristics with reduction in forming power, current and significant increase of on/off switching ratio.

5.9 Temperature dependence

The temperature dependence of the threshold switching response provides important information about device reliability and endurance, as well as providing insight into the dominant conduction mechanisms. Device characteristics were measured under voltage-controlled and current-controlled sweep as a function of temperature in the range between 296 K to 413 K. The current compliance is capped at 1 mA. Fig. 5.13 shows measured I-V characteristics as a function of temperature. With further increase in temperature, NDR is suppressed due to the rise in parallel leakage current. Both the threshold and hold voltages decrease with increasing temperature, as does the hysteresis between them as shown in Fig. 5.14. The reduction in threshold voltage is a direct result of the Joule-heating effect as a lower thermal power is required to achieve the transition temperature when the device temperature is increased. As a consequence, the CC-NDR region decreases with increasing temperature, and is effectively eliminated for temperatures above 378 K.

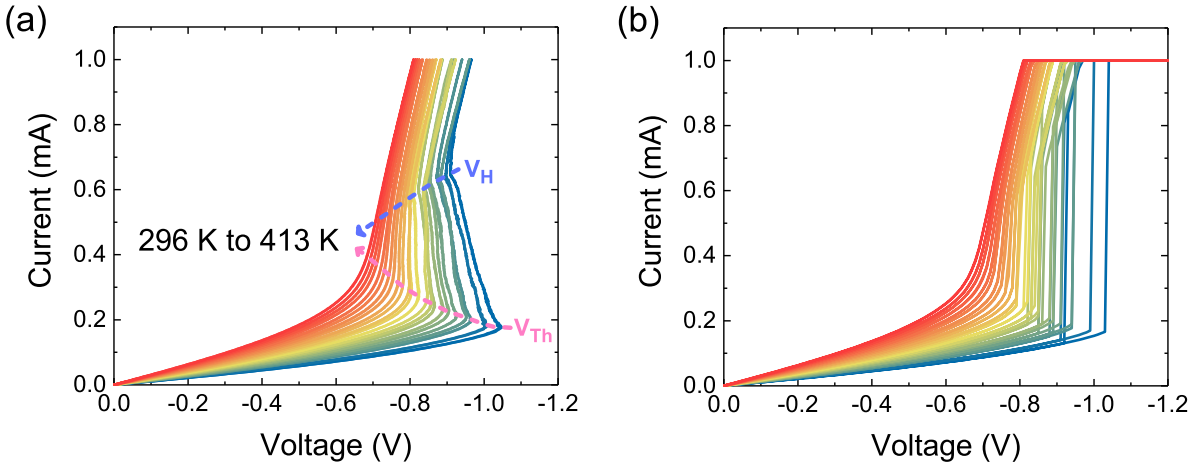

Figure 5.13: (a) I-V characteristics of CC-NDR as a function of temperature. (b) I-V characteristics under voltage-controlled sweep as a function of temperature.

Fig. 5.15(a) shows the measured and calculated I-V profiles of the devices below the critical threshold value with increasing temperature in the range from 296

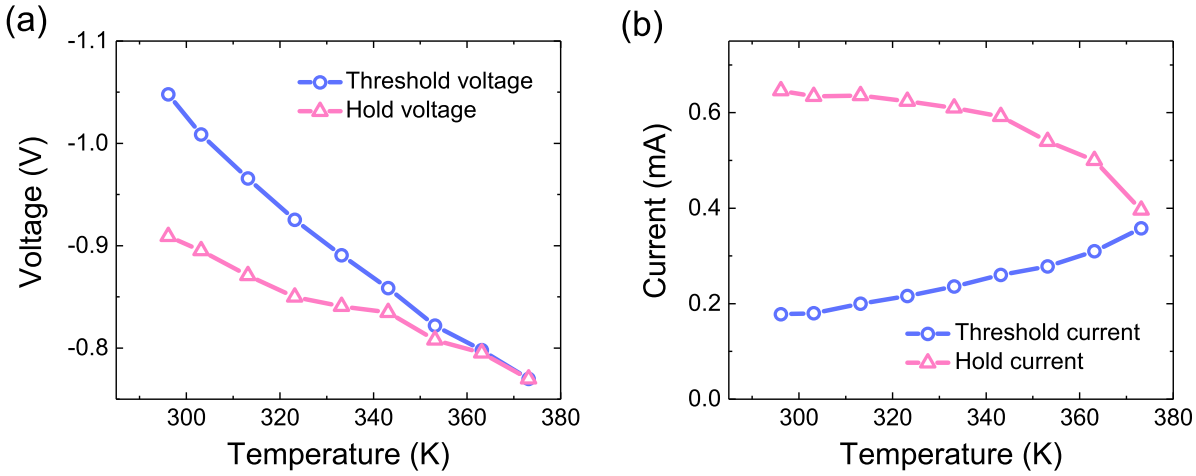

Figure 5.14: (a) Hold and threshold voltage as a function of temperature. (b) Hold and threshold current as a function of temperature.

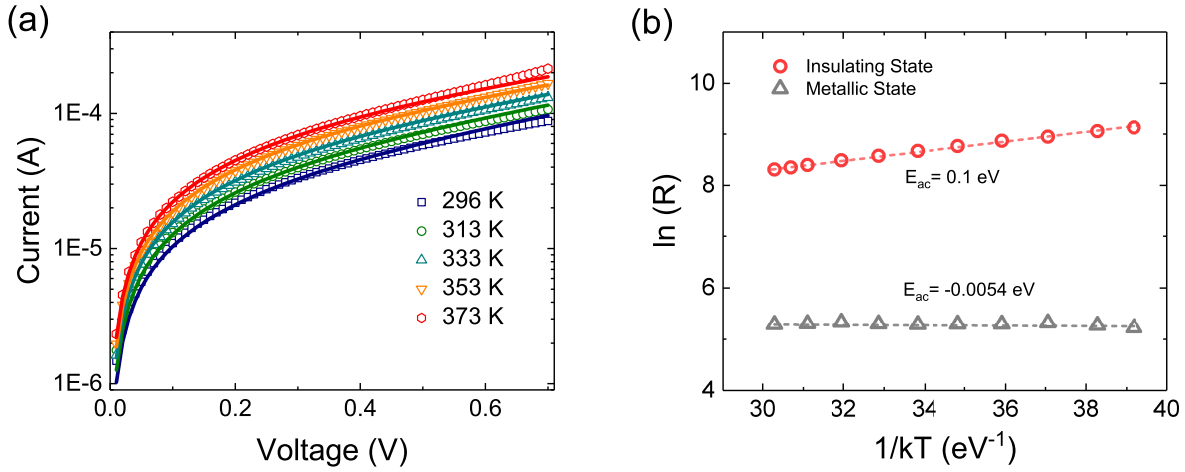

Figure 5.15: (a) Subthreshold conduction and calculated fitting with Poole-Frenkel emission. (b) Arrhenius plot of device resistance in both subthreshold and metallic states.

to 373 K. The measured temperature dependence of conduction in the insulating state shows good agreement with the analytical model based on the Poole-Frenkel emission. The activation energy of the insulating state and the metallic state are determined from the Arrhenius plot by measuring the temperature dependence of the device resistance. The resistance of the insulating state is extracted at 0.2 V and

the resistance of the metallic state is calculated from the gradient of the I-V curve. The device resistance, calculated based the local slope of the I-V curve, is plotted as a function of 1/kT as shown in Fig. 5.15(b), where k is the Boltmann constant and T is the ambient temperature. The extracted activation energy of the integrated threshold switching element and the LRS memory element is ∼0.1 eV for the insulating state and -5.4×10^{-3} eV for the metallic state which reflects the difference between the band edge relevant for carrier transport and the Fermi level. Similar activation energy measurements were conducted on other NbO_x based threshold switching devices. The measured activation energy of their insulating state (at 0.2 V) shows variation between 0.1 eV to 0.22 eV. The differences can be contributed from the forming conditions, electrode effect and film stoichiometry. Understanding the exact underlying mechanism is subject to future studies.

5.10 Summary

In summary, Pt/NbO_x/TiN thin-film structures were shown to exhibit an integrated selector-memory (1S1R) response after an initial electroforming step and successive SET/RESET operations, and to subsequently exhibit symmetric threshold switching when suitable compliance currents were employed. In the symmetric switching mode, the threshold and hold voltages were found to be independent of NbO_x thickness and device area, but the threshold current (power) was found to decrease with increasing film thickness. The independence of the threshold and hold voltages was shown to be consistent with the formation of a localized threshold switching volume at the residual conductive filament/electrode interface, while the reduction in threshold current (power) was consistent with the existence of a semiconducting shell around a filamentary core. The veracity of this proposed structure was demonstrated by comparing experimental results with the predictions of a resistor network model, and detailed finite element simulations. The comparison of switching characteristics between the nano-scale and the micro-scale devices confirms that

the threshold switching occurs within a localised volume. With area downscaling to nano-scale, devices show considerable improvements in switching properties, including reduction in switching power and increase in on/off ratio. Temperature dependence of threshold switching response was studied to show a reduction in voltage and an increase in current of threshold and hold values with increasing temperature. Temperature and field dependent conduction of the subthreshold region is well described by the Poole-Frenkel conduction which supports the finite element modelling. These results provide further insights into the design and implementation of NbO_x threshold switching devices for emerging memory and neuromorphic computing applications.

Chapter 6

NbO_x Relaxation Oscillators

6.1 Introduction

Threshold switching devices and self-sustained electrical oscillators have attracted particular attention due to their potential as selector elements in emerging non-volatile memory and as building blocks for bioinspired neuromorphic computing, respectively [18, 46, 191, 203]. Among these, devices based on metal-oxide-metal (MIM) structures offer the advantage of device simplicity and scalability, and have been used to realize systems of nano-crossbar array memory and coupled nano-oscillators [18,46,204]. The systems of particular interest in the present study display current-controlled negative differential resistance (CC-NDR), also called threshold switching. The devices are able to transit from an insulating state to a metallic state with external excitation and revert back back the insulating state when the simulation is removed.

Vanadium dioxide (VO_2) is a well studied prototypic material for the CC-NDR element in relaxation oscillators and the resulting oscillators have been shown to operate at frequencies in the range from 1 kHz to 9 MHz [174,175,178,181–183]. However, the CC-NDR in VO_2 results from a Mott-Peierls transition at a temperature of ~340 K. This precludes its use in many microelectronics applications, where the expectation is that devices will operate at temperatures approaching 400 K. To address this limitation, recent interest has been focused on NbO_x which has demonstrated higher operating temperatures [51,71,205], extending the possible temperature range

of applications.

Although there are some early reports on NbO_2 self-oscillation [167, 206], Lalevic and Shoga first reported stable and reproducible oscillations with frequency up to ~600 kHz in single crystal NbO_2 and polycrystalline NbO_2 films in 1981 [207]. Several reports have highlighted the nonlinear current–voltage (I-V) characteristics of electrically switched NbO_x thin films [196, 202, 208, 209] and the occurrence of periodic oscillation signals maintained across two-terminal devices [37, 39, 144]. A unique feature of these CC-NDR based oscillators is that they do not require any inductive elements or transistors as required in conventional electrical oscillators [37, 144]. These features are particularly attractive for making scalable, low-power devices.

In this chapter, we investigate the self-oscillation behavior of NbO_x threshold switching devices and introduce a finite element model of threshold switching that accounts for the CC-NDR response of devices and provides the basis for studying the relationship between the materials response and oscillator dynamics. The model is extended to include the effect of circuit elements in a simple Pearson–Anson electrical circuit and shown to capture the periodicity and waveform of device currents and voltages as a function of the circuit parameters. The temperature dependent oscillation dynamics were also investigated to provide insights on temperature tolerance and tuning variability. These results provide an in-depth understanding of the nature of oxide oscillators and their dependencies.

6.2 Experimental details

Pt/Ti(10 nm)/NbOx/Pt test structures were employed for this study, as shown in Fig. 6.1. To fabricate devices, a 100 nm Si_3N_4 was first deposited on a Si substrate by plasma-enhanced chemical vapour deposition (PECVD) at 300 ^oC. Pt (50 nm) bottom electrodes (BEs) were then deposited on the Si_3N_4 by electron beam

evaporation. The Si_3N_4 surface was cleaned in-situ by Ar-ion bombardment prior to Pt deposition to obtain good adhesion between Pt and Si_3N_4. 75 nm thick films of NbO_x oxide were deposited onto the Pt BEs at room temperature using DC reactive sputtering from a metallic niobium target, in which the stoichiometry was controlled by the ratio of argon to oxygen (18/2 at 20 sccm) at a constant total pressure of 4 mTorr and sputtering power of 150 W. Patterned top electrodes (150–250 μm in diameter) were then deposited through a shadow mask by e-beam evaporation in a vacuum better than 10^{-6} Torr. These comprised a ∼10 nm Ti layer followed by a 50 nm Pt layer to provide more robust contact pads and to protect the Ti from oxidation. After fabrication devices were subjected to a rapid thermal anneal at 300 ^{o}C for 5 min.

The stoichiometry of the NbO_x films were determined by the electron Rutherford backscattering (eRBS) technique [202,210] and X-ray diffraction confirmed that they were amorphous, both as-deposited and after annealing at 300 ^{o}C [51]. Electrical measurements were carried out in air using an Agilent B1500A semiconductor parameter analyser attached to a Signatone probe station.

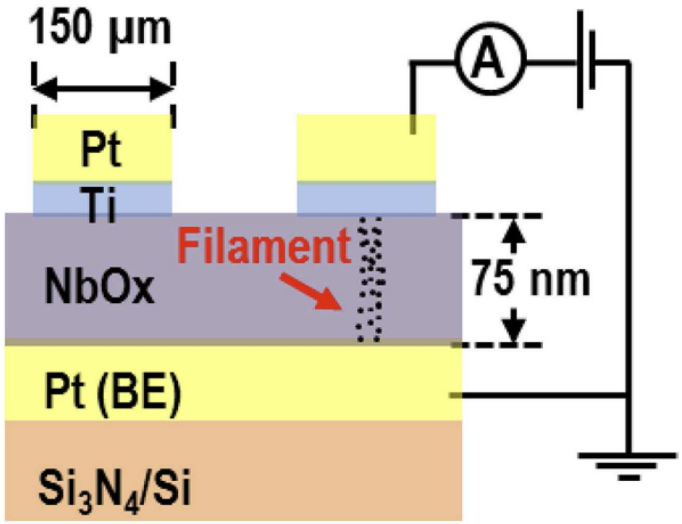

Figure 6.1: Schematic of the fabricated Pt/Ti/NbO_x/Pt test devices and the measuring conditions.

6.3 Analysis of self-sustained oscillation

6.3.1 Oscillation dynamics

Fig. 6.2 shows typical DC current-voltage (I-V) characteristics of devices during voltage-controlled (Fig. 6.2(a)) and current-controlled (Fig. 6.2(b)) sweeps. The former shows threshold switching behaviour in which the oxide layer transforms to a metallic state as the voltage is increased beyond a threshold value (P1) and returns to an insulating state as it is reduced below a critical hold point (P2). In this case the threshold switching is believed to result from Joule heating of a filamentary

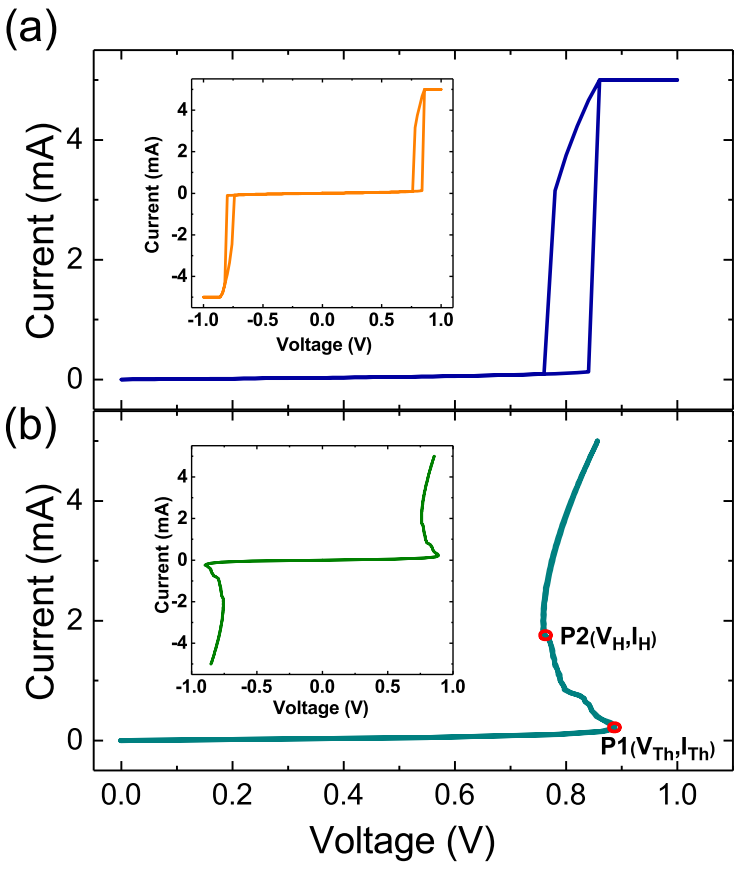

Figure 6.2: Typical current-voltage characteristics of the device. (a) positive voltage sweep and (b) positive current sweep. Insets show symmetric, non-polar nature of voltage and current sweeps.

conduction path in the oxide layer and its nonpolar switching nature is illustrated in the inset of Fig. 6.2(a). In this context, it should be noted that threshold switching is only observed after an initial forming process in which the voltage is scanned from 0 to -8 V with 20 mA compliance current.

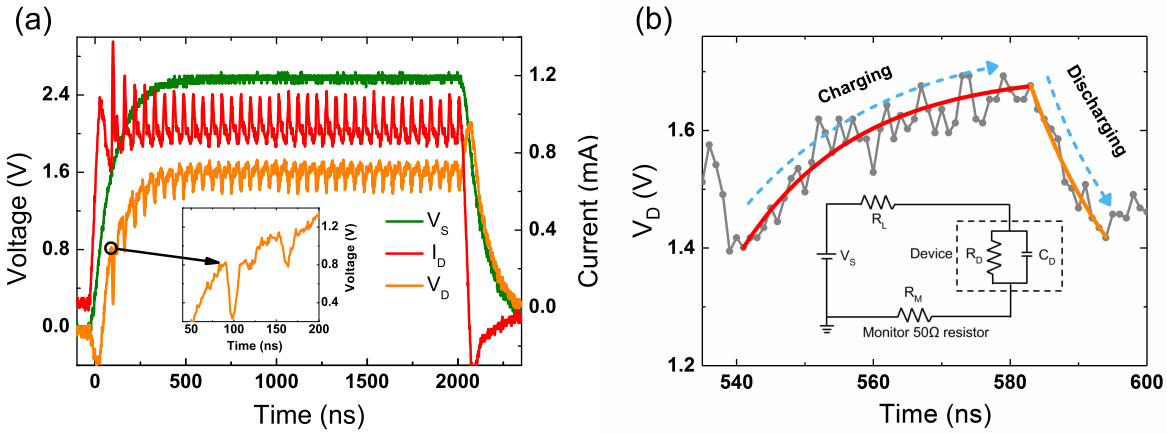

Figure 6.3: (a) Electrical oscillatory responses of V_D and I_D during a 2 µs 2.6 V pulse. Inset shows detail of the initial response. (b) Expanded view of a single device voltage oscillation. Inset shows the equivalent circuit used for analysis.

The current-controlled I-V sweep (Fig. 6.2(b)) provide additional insight into the switching process, and clearly highlights the NDR response of these devices. This was measured by scanning the current from 0 mA to 5 mA and back to 0 mA in 50 µA steps. The voltage and current at the threshold (V_{Th}, I_{Th}) and hold (V_H, I_H) points were measured as ∼0.3 mA and ∼0.88 V, and ∼1.95 mA and ∼0.76 V, respectively. The symmetric, nonpolar nature of the characteristics is again highlighted in the inset. This NDR response provides the basis for a relaxation oscillator and is the focus of the following discussion.

The oscillation dynamics of NbO_x devices were studied by including the devices in a series circuit as shown in the inset to Fig. 6.3(b). The circuit consists of source voltage (V_S), a load resistor (R_L), a 50 Ω monitoring resistor (R_M) and the device under test. Rectangular voltage pulses were generated with a Waveform Generator/Fast Measurement Unit (WGFMU) as part of the B1500A analyser, and the

resulting electrical response was recorded by monitoring the voltage drop across the 50 Ω resistor using a Tektronix TPS2024B oscilloscope.

Fig. 6.3(a) shows the device voltage (V_D) and device current (I_D) during excitation with a pulse of amplitude of 2.6 V and width of 2 µs, with R_L equal to 1 kΩ. Oscillations begin as V_D reaches ∼0.82 V, as illustrated in the inset to Fig. 6.3(a), which is close to the threshold voltage reported in Fig. 6.2(b). Stable, periodic oscillations are observed once V_S reaches its specified value of 2.6 V. For this case, the peak-to-peak voltage and current amplitudes were measured as ∼0.3 V and ∼0.26 mA, respectively. The oscillation frequency was determined from fast Fourier transform analysis to be 19 MHz in this case.

The oscillator circuit depicted in Fig. 6.3(b) is of the Pearson-Anson form and its response is determined by the device NDR characteristics (Fig. 6.2(b)) and by V_S and R_L [211]. The oscillation of V_D shows an exponential rise and sharp fall as illustrated in Fig. 6.3(b). The time constant for charging is given by R_TC_T where C_T is the overall capacitance associated with the intrinsic device capacitance (C_{Device}) and the parasitic capacitance ($C_{Parasitic}$). $C_{Parasitic}$ arises from the measurement system, i.e., coaxial cables, the voltage source, and probes. $R_T=(R_L+R_M)R_D/(R_L+R_M+R_D)$ with R_D representing the high resistance state of the NbO_x device. The time constant for charging was ∼42 ns in this case. As V_D approaches its maximum value, the device switches to its low resistance state and V_D begins to drop with an R_TC_T time constant in which R_D now represents the low resistance state of the device. The discharging time constant was ∼11 ns.

6.3.2 Voltage and load resistance dependence

Fig. 6.4 depicts the oscillation range of V_S and R_L for both polarities, and compares values determined from direct measurement with those derived from the data in Fig. 6.2(b) using load-line analysis [212]. The region bounded by the solid lines represents V_S and R_L values for which stable oscillation was observed. Load line

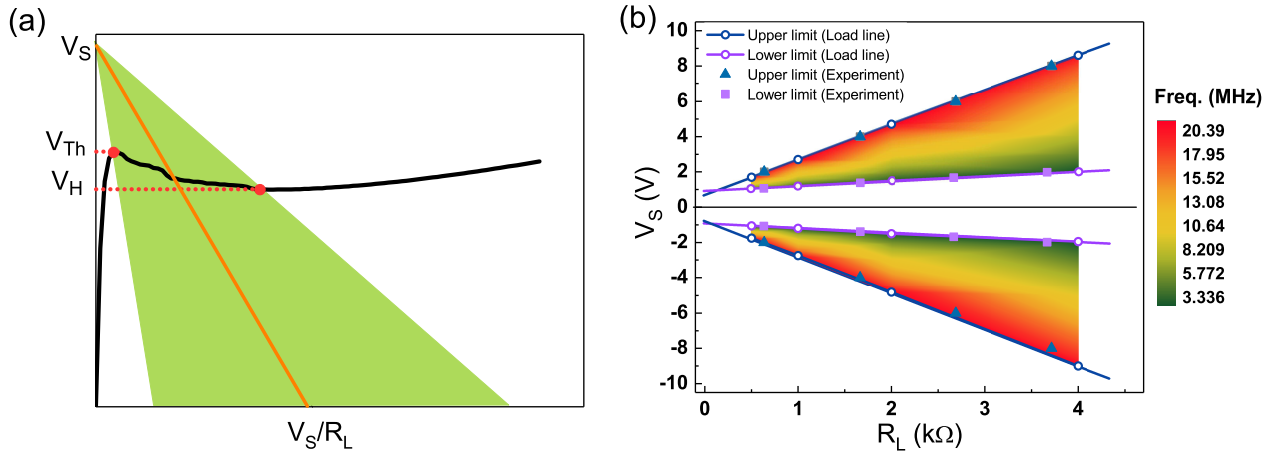

Figure 6.4: (a) Loadline analysis based on the CC-NDR response obtained in Fig. 6.2(b). (b) Oscillation window defined by V_S and R_L with oscillation frequency depicted by shading. The color-coded region is the effect of these parameters on the oscillation frequency. The solid triangle and rectangle data points of the lower and upper limits were obtained through experimental measurements.

analysis shows that the voltage window for stable oscillation is from $V_{S,min}$ to $V_{S,max}$, where $V_{s,min} = V_{th} + (R_L + 50)I_{th}$ and $V_{s,max} = V_h + (R_L + 50)I_h$.

A 2-µs-long bias pulse with voltage amplitude in the range of ($V_{S,min}$, $V_{S,max}$) was applied, during which voltage oscillations across the Ti/NbO_x device were observed. With R_L of 1 kΩ, load-line analysis indicates that the oscillation generation window is between 1.1 and 2.9 V. Fig. 6.5 shows the measured device current ($I_{Device} = I_{50\Omega} = V_{50\Omega}/50$) at various V_S values ranging from 1.0 to 2.8 V. Three features are evident. The first feature is sporadic oscillations with an ill-defined period for V_S around 1.17 V, which is the threshold for inducing the transition. Interestingly, even when using the same operation conditions, a different number of peaks is observed, an effect related to the stochastic nature of the switching process and intrinsic material inhomogeneities. stable relaxation oscillations were observed with V_S between 1.17 V and 2.6 V. With further increase in applied voltage, damped oscillation is observed for $V_S \geq 2.6$ V where the device tends to remain in the metallic state during the pulse period. This damped oscillation is typical for a circuit with CC-NDR elements when the source voltage is close to the upper limit. These fea-

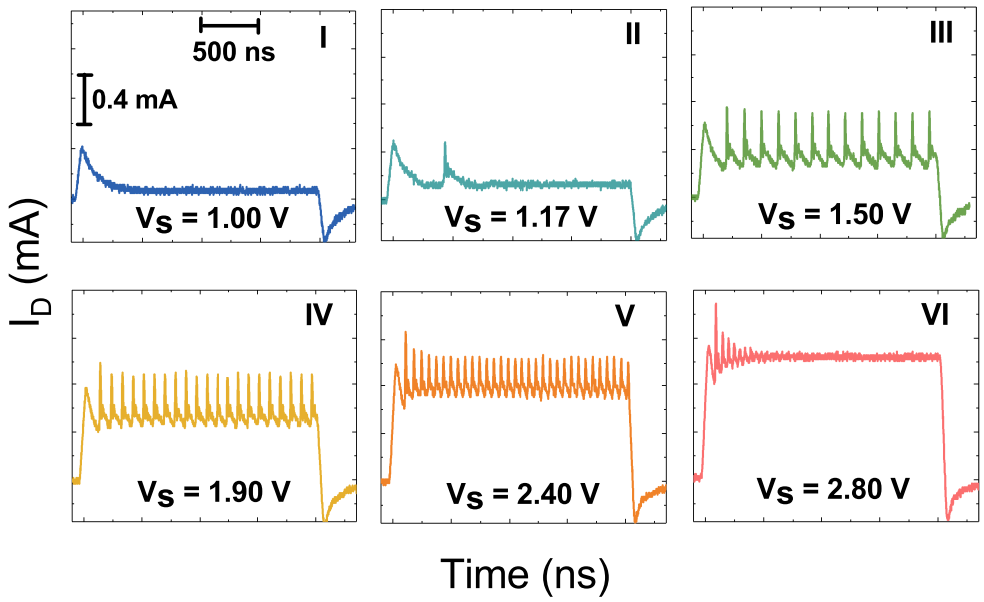

Figure 6.5: Measured oscillation waveform of the device current (I_{Device}) in the 50 Ω resistor for 2 µs source voltage (V_S) pulses in the range from 1.0 to 2.8 V and a series resistor of 1 kΩ.

tures can also be observed for different V_S with R_L = 500 Ω, 2 kΩ, and 4 kΩ, as shown in Fig. 6.6.

The frequency of the NbO_x oscillator was observed to increase as V_S increased, with a voltage tuning sensitivity of f_{osc} from 22.6 MHz/V with R_L of 0.5 kΩ to 2.5MHz/V with R_L of 4 kΩ. This is shown more explicitly in Fig. 6.7 which also demonstrates the near linear scaling of frequency with V_S. This dependence is consistent with that expected for the Pearson-Anson oscillator shown inset in Fig. 6.3(b) which predicts a dependence of the form [212].

$$f_o = \left[\alpha R_L C \ln\left(\frac{V_S - V_H}{V_S - V_{Th}}\right)\right]^{-1} \tag{6.1}$$

where V_{Th} and V_H are the threshold and hold voltages, and α is a scaling parameter, that accounts for factors such as parasitic capacitance. The solid lines in

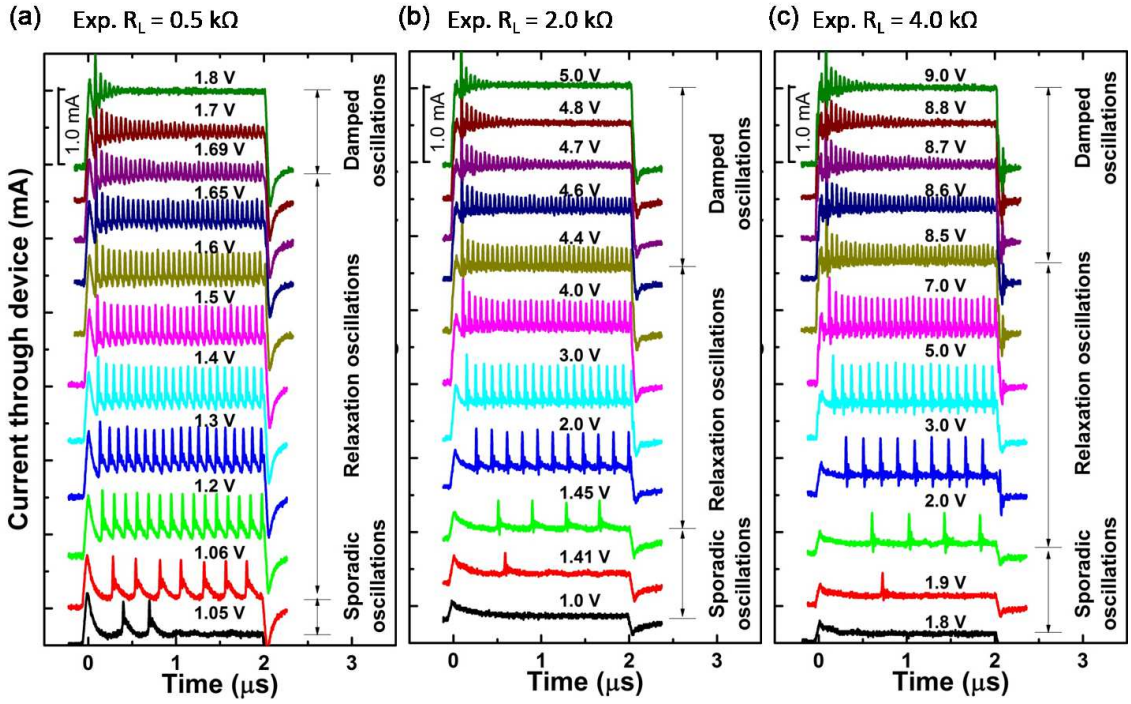

Figure 6.6: The measured oscillation of device current I_{Device} as a function of source voltage V_S for different load resistors R_L: (a) 0.5 kΩ, (b) 2 kΩ, and (c) 4 kΩ. Three features are evident: (1) Sporadic oscillations with an ill-defined period; (2) Stable relaxation oscillation; and (3) Damped oscillations.

Fig. 6.7 represent a fit of this equation to the data, with a fixed α value of 55 for all curves.

Device endurance and stability are important for practical applications. These were tested by running oscillators for 96 minutes with a pulse amplitude of 2.2 V, which corresponds to $\sim 6.5\times10^{10}$ oscillation cycles. The oscillation characteristics were monitored after 1, 6, 36 and 96 minutes by recording the oscillator output. The stability of the peak-to-peak device current and oscillation frequency are shown in Fig. 6.8. The peak-to-peak current is observed to undergo a 20% reduction in amplitude during the first $\sim 8\times10^{8}$ (1 minute) cycles but to remain reasonably constant thereafter. In contrast, the oscillation frequency decreases almost linearly with increasing cycle number, decreasing by around 25% over the full testing period, $\sim 6.5\times10^{10}$. The relative changes in the peak-to-peak current and frequency are

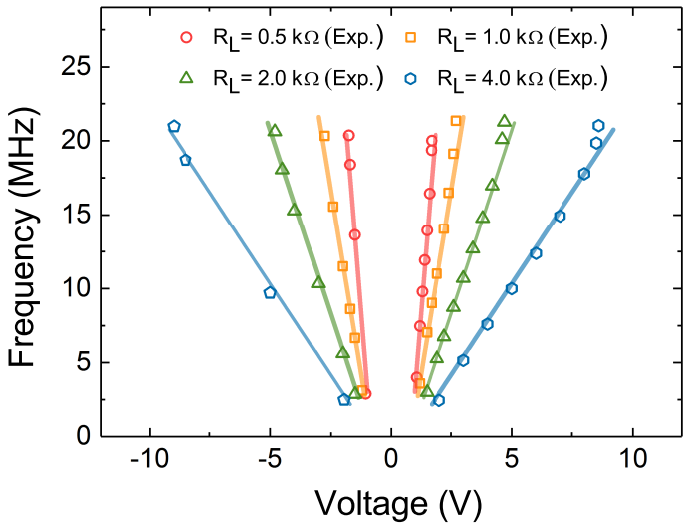

Figure 6.7: Oscillation frequency as a function of V_S for different values of R_L. Solid lines represent fits of Equation (6.1).

similar (∼25%) over the full testing period, but their trend with increasing cycle number is clearly quite different. The only variables in the circuit, once V_S and R_L are fixed, are the device capacitance and resistance. It is therefore clear that the device structure changes with time during continuous operation.

For the simple equivalent circuit depicted in Fig. 6.3(b) the device current depends only on changes in the device resistance, while the frequency is affected by changes in both the resistance and capacitance. While it is possible to construct schemes where specific changes in resistance and capacitance account for the changes reported in Fig. 6.8 this remains speculative. Chemical reactions at the NbO_x/Ti interface or modification of the threshold switching volume are likely to occur due to local Joule-heating. Further work is required to understand the physical evolution associates with the changes in frequency and peak-to-peak amplitude occurring in the device.

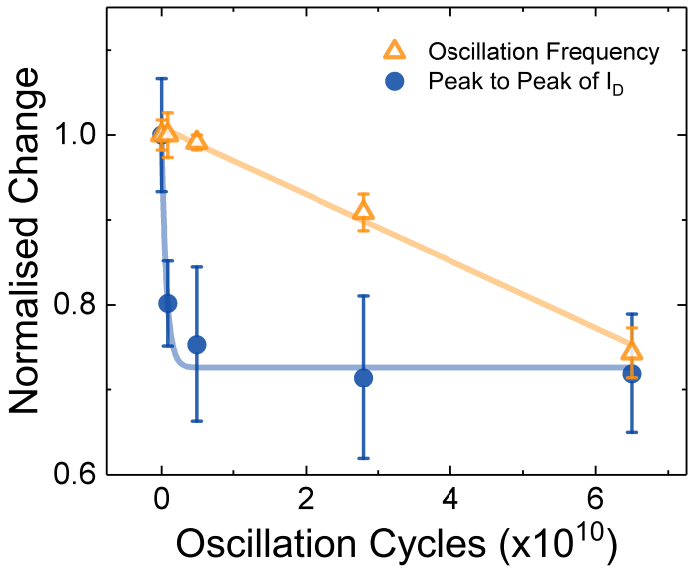

Figure 6.8: Change in oscillation frequency and peak-to-peak amplitude as a function of oscillation cycle number. The data points represents measurements after 1, 6, 36 and 96 minutes. The error bar heights represent the standard deviation over 8 individual pulses for each timestamp.

6.4 Temperature dependent oscillation

The temperature dependence of threshold switching (CC-NDR) has been studied in VO_2, Ti_2O_3, Ta_2O_5 and NbO_2 systems [58, 176, 209, 213, 214]. However, the temperature dependence of self-oscillation in these transition-metal-oxides has received far less attention. Kim et. al. showed that the oscillation frequency of planar VO_2 two terminal devices increased with increasing temperature [215], but provided little insight into the effect of temperature on frequency tuning (increase in frequency with applied voltage), or the frequency range. In this section, we investigate the temperature dependence of CC-NDR in Pt/NbO_x/TiN devices, and its effect on the dynamics of a Pearson-Anson relaxation oscillator based on these devices. The details of device fabrication and the electroforming process are described in Section 5.2.

Fig. 6.9 shows a current-controlled I-V sweep for the device after stabiliza-

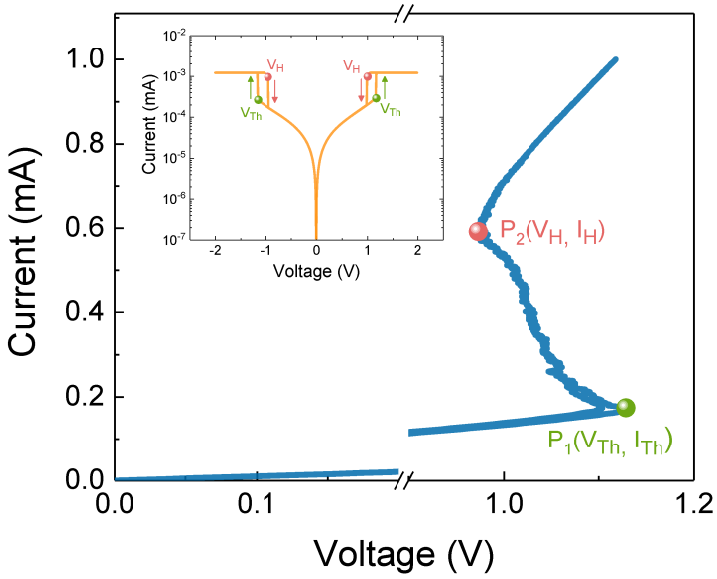

Figure 6.9: Measured I-V characteristics during current-controlled sweeps showing clear NDR characteristics. The NDR region forms the basis of the relaxation oscillator. The inset is the symmetric voltage controlled threshold switching.

tion. The region of CC-NDR is bounded by the threshold point P1 (V_{Th}, I_{Th}) and the hold point P2 (V_H, I_H), and corresponds to a region in which the conductivity of the sample increases rapidly. For currents above the hold-current, I_H, the conductivity reaches a maximum and the device exhibits near-Ohmic behaviour. The device therefore exhibits three distint regimes as the current increases, a pre-threshold regime, a negative differential regime and a saturation regime. For a device voltage of 1.05 V, the resistances in these regimes are 3.8 kΩ, -436 Ω and +407 Ω, respectively.

Oscillator dynamics were studied by incorporating the device-under-test (DUT) in a simple Pearson-Anson oscillator circuit, as shown schematically in Fig. 6.3(b) and discussed previously in Section 6.3. The conditions for stable oscillation are determined from the measured I-V characteristics using standard load line analysis. The corresponding V_S-R_L oscillation window and frequency are shown in Fig. 6.10(a) for room temperature operation. For a given load resistance, the oscillation frequency is observed to increase from around 1.2 to 8.8 MHz as the

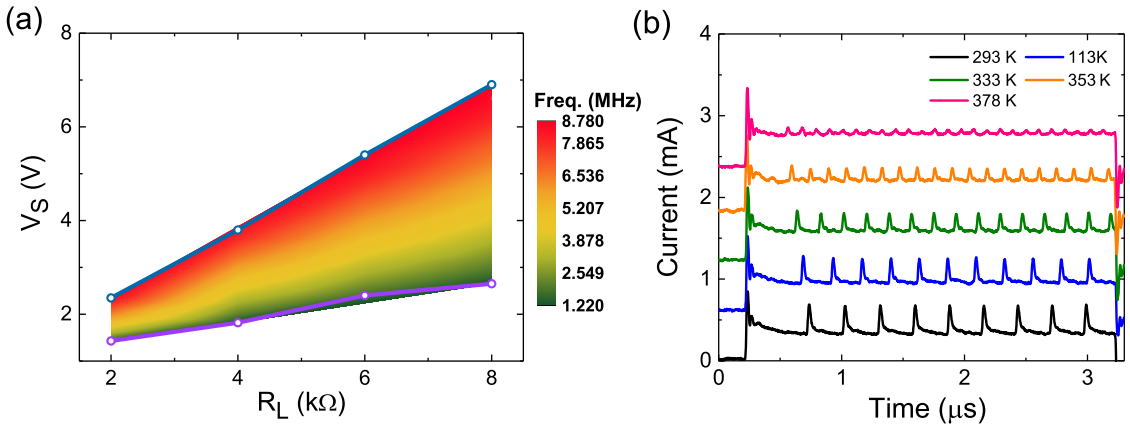

Figure 6.10: (a) Oscillation window defined by V_S and R_L with oscillation frequency depicted by shading. The black squares are from load line analysis. (b) Oscillation as a function of temperature for an applied pulse of 2.4 V and 3 μs.

voltage is varied from $V_{S,min}$ to $V_{S,max}$. Since the voltage window increases with increasing load resistance, the voltage-tuning sensitivity decreases from 7.57 MHz/V for R_L equal to 2 kΩ, to 1.77 MHz/V for R_L equal to 8 kΩ.

The measured I-V characteristics and corresponding threshold- and hold-voltages and currents as a function of device temperature are shown in Fig. 5.13(a) and Fig. 5.14. The effect of these changes on the oscillation behaviour was studied using the circuit of Fig. 6.2(b) with a load resistance of 4 kΩ. The choice of load resistance is largely arbitrary as it is temperature independent, but it does determines the voltage range over which oscillations are observed, as shown in Fig. 6.10(a). Fig. 6.10(b) shows the oscillator response as a function of temperature for an applied bias of 2.4 V. This shows that the oscillation frequency increases, and that the oscillation amplitude decreases with increasing temperature. The reduction in amplitude is consistent with the observed reduction in the threshold- and hold-voltages, and the oscillation window can be determined from the CC-NDR curves shown in Fig. 5.13(a) using load line analysis. In this figure, the points indicate the window-boundaries determined from load-line analysis, and the color-coded data defines the region in which oscillations were directly measured. In this case, oscillations were found to

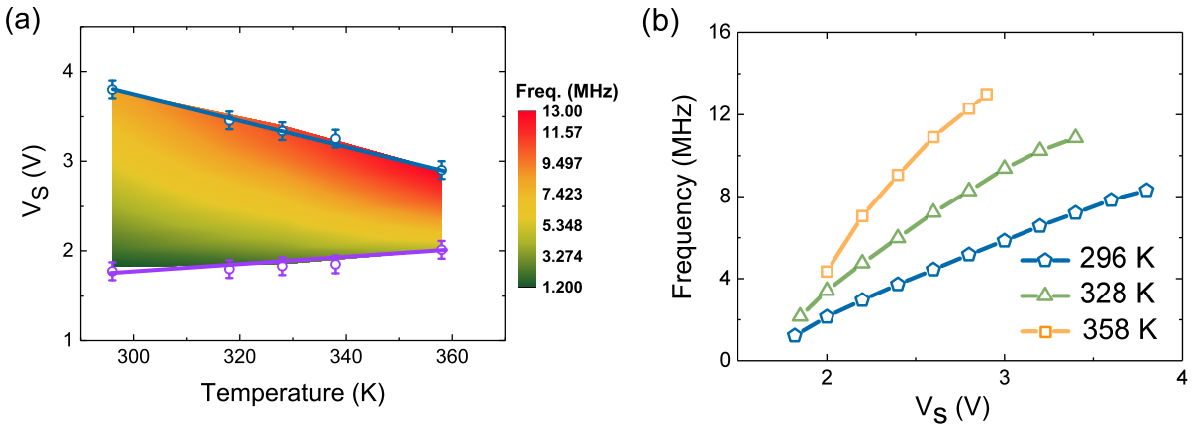

Figure 6.11: (a) Measured oscillation window as a function of temperature with a constant load resistor of 4 kΩ. The oscillation frequency depicted by colour shading and the green/red circles are from load line analysis for corresponding temperature. The error bar heights represent the standard deviation over 3 pulses for temperature. (b) Frequency as a function of applied bias at three different temperatures.

disappear for temperature above 378 K.

The effect of temperature on the oscillation frequency is shown color-coded in Fig. 6.11(a), and explicitly in Fig. 6.11(b). For a fixed source voltage and load resistance, the frequency is observed to increase with increasing temperature, as expected from the change in the CC-NDR characteristics. For example, by assuming that the oscillation frequency is limited by the slower, low-to-high transition, and that the monitor resistor can be ignored, the low-frequency behavior has the form [212]

$$f_o = \left[R' C_D \ln \left(\frac{\beta V_S - V_H}{\beta V_S - V_{Th}} \right) \right]^{-1} \tag{6.2}$$

where, $R' = R_D R_L/(R_D+R_L)$, and $\beta = R_D/(R_D+R_L)$. Since V_{Th} decreases more rapidly with temperature than V_H, as shown in Fig. 5.14, the frequency is predicted to increase with temperature. However, this simple analysis ignores the temperature dependence of device resistance (R_D) and capacitance (C_D), and therefore overestimates the temperature sensitivity. It also fails to account for the dynamics of the

resistive and capacitive device currents, as previously discussed.

The data in Fig. 6.10(b) and Fig. 6.11 highlight the important functionalty of these relaxation oscillators, including the temperature dependent oscillation frequency, the ability to program the oscillator frequency and its temperature coeffient using the source voltage. The latter is evident from the data in Fig. 6.11(b), which shows an increasing frequency span as the voltage increases. For example, in the temperature range 296-328 K, the temperature coefficient ranges from 39.6 kHz/K at a source voltage of 2 V, to 110 kHz/K at a source voltage of 3 V.

6.4.1 Oscillation in nanoscale device

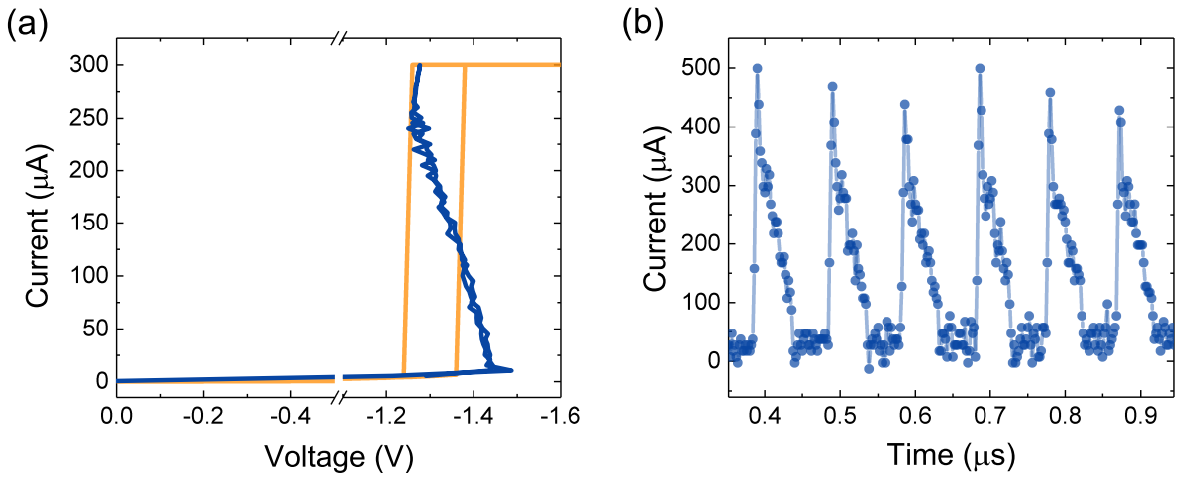

Figure 6.12: (a) I-V characteristics of nanovia devices with 400 nm diameter. (b) Stable periodic oscillations with a 10 kΩ series resistor during a 2 μs -2.6 V pulse.

Nanovia devices with effective device area of 400 nm diameter were fabricated so as to compare the oscillation response with the micro-size devices. The device fabrication and details of initial forming process are described in Section 5.8. Fig. 6.12(a) illustrates the typical device electrical response under voltage-controlled and current-controlled sweeps where the slight difference in hold voltage is due to the variation of sweep rate between the two modes. The periodic oscillation of device current in Fig. 6.12(b) corresponds to the transitions of device conductance. The expanded view in Fig. 6.13(a) demonstrates the transition process from insulating state to metallic state with ~6 ns switching time (ΔT_{ON}). The switching time is significantly reduced in comparison to the micro-size devices due to the downscale in device area which results reduction in device capacitance. The switch-off time (ΔT_{OFF}) is ~46 ns. Fig. 6.13(b) shows oscillation frequency scales with source voltage from 2.6 to 10.66 MHz which are similar to the behaviour observed in micro-size devices. Although there is a significant reduction in device capacitance from downscaling device area, the minimum and maximum operating frequency still remains consistent as to the microscale devices. This suggests that the oscillation frequency is largely limited by the circuit capacitance which determines the RC time constant.

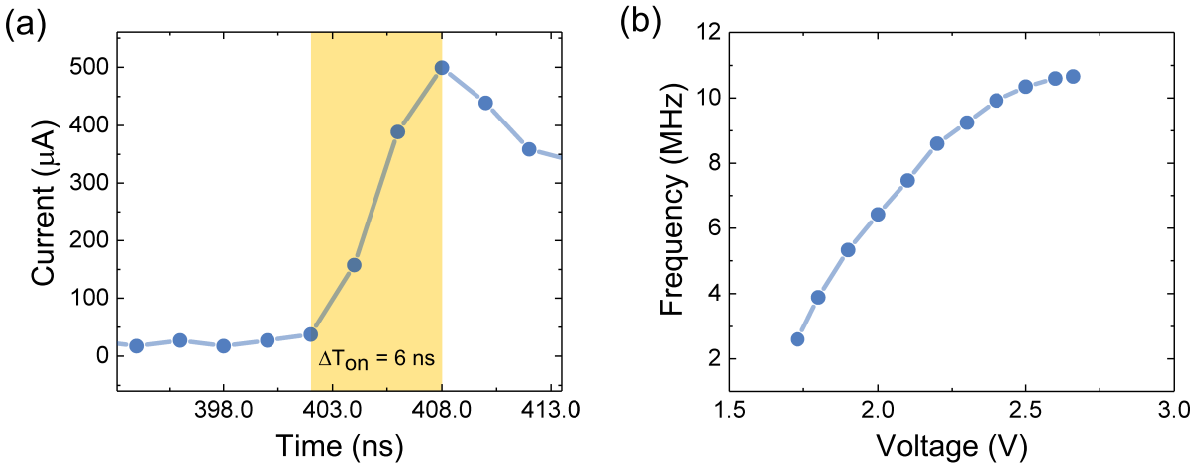

Figure 6.13: (a) Expanded view of transition process from insulating to metallic state. (b) Oscillation frequency as function of source voltage with a 10 kΩ series resistor.

6.5 Numerical modelling of oscillation behaviour

6.5.1 Modelling details

Pickett and Williams established a compact analytical model of threshold switching based on Joule heating of a volume that undergoes an insulator-to-metal transition, and used a SPICE simulation to obtain good agreement with the experimental measurements of the static and dynamic behaviour of devices [37]. However, a large departure between the experimental and the model I–V curves was observed, especially in the low current region below the threshold voltage [37]. This departure was believed to arise from the most aggressive assumption of their model where the electrical resistance of the insulating phase is constant and temperature independent, and the temperature within the metallic filament is uniform. Furthermore, using these simple material and geometric parameters, this model is unable to adequately describe our data, in particular, the feature of the NDR region in the quasi-static current-sweeping I–V curves. To address these limitations and more accurately describe Joule heating and thermal transport between the metallic filament and the surrounding device, the Pickett model was extended using a finite-element model.

A two dimensional (2D) axis-symmetric finite element simulation model was solved self-consistently in a time-dependent solver with the I-V charactersitics as shown in Fig. 6.14(b). In relation to our micro-meter sized devices with 75 nm thick films and the high compliance current (∼20 mA) forming process, the model considers a NbO/NbO_2 current channel (filament) surrounded by oxygen-deficient Nb_2O_{5-x} as the simulated cell, where the effective NbO_2 zone is a small active region with 100 nm diameter and 30 nm thickness, as shown in Fig. 6.14(a). The threshold switching response of NbO_2 is assumed to result from a thermally induced MIT as proposed by Pickett and Williams [37]. The time-dependent heat equation is solved, along with the continuity equation for temperature T and potential V [202,216], i.e.,

$$\rho_m C_p \partial T/\partial t - \nabla k \nabla T = J^2/\sigma \tag{6.3}$$

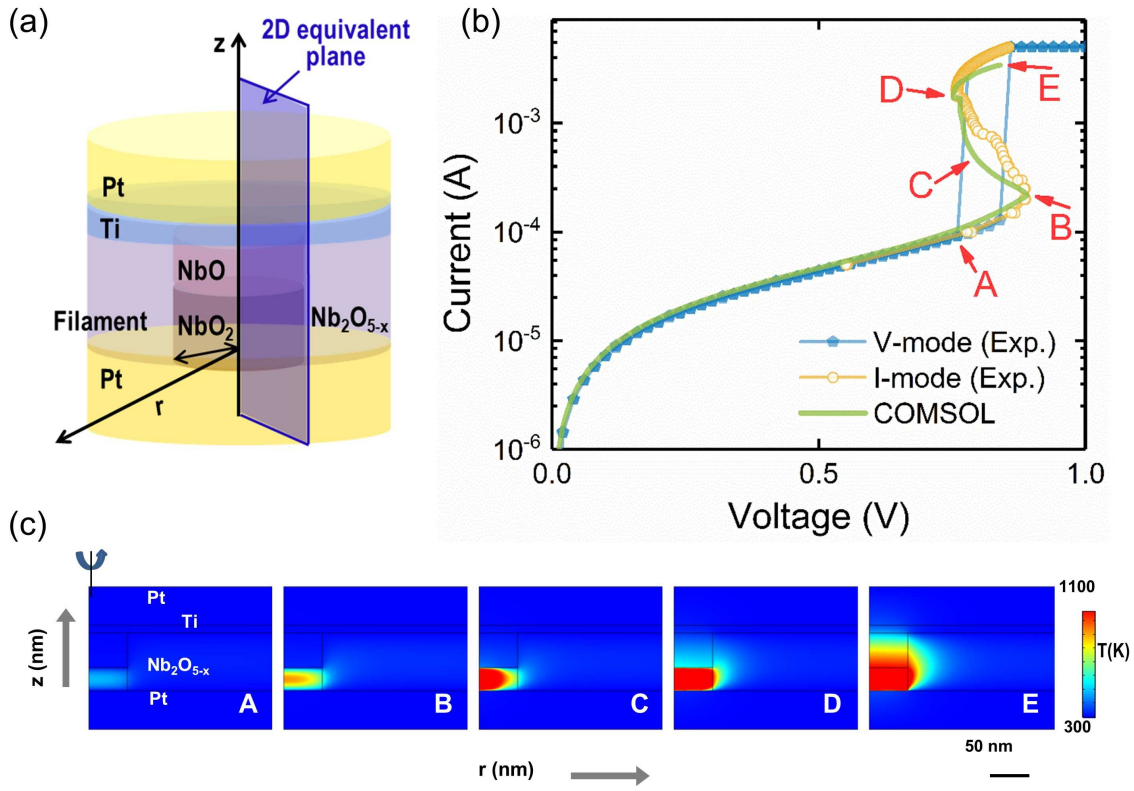

Figure 6.14: (a) Geometry of the simulated device structure assuming a cylindrical conductive channel (filament) comprised of NbO/NbO2 zones and surrounded by an Nb_2O_{5-x} matrix. (b) The comparison of simulated and experimental I–V characteristics of Pt/Ti/NbO_x/Pt devices. (c) Calculated 2-D maps of temperature for states A, B, C, D, and E as depicted in the I–V curve of the simulation results. The red color represents the high-temperature metallic regions during the MIT.

$$\nabla J = \nabla \sigma \nabla V = 0 \tag{6.4}$$

where ρ_m, C_p, k, J, and σ denote mass density, heat capacity, thermal conductivity, local current density, and electric conductivity, respectively. The k and σ values of NbO_2 film depend on device temperature and its conduction state. Simply, we use $k_{insulator} = 0.07$, $k_{metal} = 1.5$ W m^{-1} K^{-1}, and $\sigma_{insulator} = \sigma_o exp(-E_a/k_B T)$, $\sigma_{metal} = 1{\times}10^4$ Ω^{-1} m^{-1}. Here, σ_o is a pre-exponential factor, and E_a is the activation energy for carrier transport. We further assumed that the Nb_2O_{5-x} zone represented the

high resistance state of the memory [217], and that the temperature dependence of k and σ were given by: $\sigma_{Nb_2O_5} = \sigma_o exp(-E_a/k_BT)$ and $k_{Nb_2O_5} = k_{th0}(1+\lambda(T-T_0))$, where σ_o = 100 Ω^{-1} m^{-1}, E_a = 0.048 eV, k_{th0} = 0.035 W m^{-1} K^{-1}, and λ = 0.01 K^{-1}. The k and σ values of the NbO zone represented the low resistance state of the memory, and were assumed as σ_{NbO} =7.5×10^4 Ω^{-1} cm^{-1} and k_{NbO} = 10 W m^{-1} K^{-1} [217]. For the k and σ values of Pt and Ti and other key material parameters (e.g. mass density and heat capacity), we used the build-in material parameters in COMSOL software.

The metal-insulator transition temperature (T_{MIT}) for thermally induced phase transitions in transition metal oxides can differ during heating and cooling branches [218]. However, no such hysteresis is reported for NbO_2 films [68]. To simplify the analysis, we therefore assumed the same transition temperature in the calculation, with the MIT transition modelled by temperature-dependent thermal and electrical conductivities that vary between those of the insulating and metallic phases over a temperature range of 100 K, centered at the nominal transition temperature of 1073K. These parameters were chosen to match the published data on the MIT in NbO_2 [37, 202]. This allowed a quantitative analysis of field and temperature contributions and accounts accurately for the CC-NDR characteristics of the DC response [195, 198, 202].

6.5.2 I-V characteristics

The calculated I-V characteristics for the best fit of the model to the experimental data are shown in Fig. 6.14(b). Both the low and high current regions are matched reasonably well except for a deviation in the multi-NDR region. The on/off ratio for the current jump across the transition is around one order of magnitude, which is close to the resistance change across the thermal transition in NbO_2. The threshold and hold voltage points are (V_{Th}∼0.89 V; I_{Th}∼0.2 mA) and (V_H∼0.74 V; I_H∼1.6 mA), respectively, with the hold current being slightly less than the experimental

value (2.1 mA). The fact that the model reproduces the CC-NDR response of the device means that it can be used as a predictive tool for circuit design as well as for simulating the parametric behaviour of oxide threshold switching. Fig. 6.14(c) shows the calculated 2D map of temperature for states A, B, C, D, and E as labelled in Fig. 6.14(b). Initially, at low biases, the device is resistive and the current conducts through the NbO_2 zone, then the temperature increases with the increasing current due to Joule heating (A-B in Fig. 6.14(c)). As the device current increases above I_{th} (B in Fig. 6.14(c)), the conductivity of the filament decreases and the local MIT is induced in the central hot spot of NbO_2 zone, as shown in the red color region, which results in the CC-NDR shown in the I-V curve. A complete metallic NbO_2 zone emerged around I_H (D in Fig. 6.14(c)), and as the current increases further, the NbO_2 zone remains in the metallic state, and the temperature increases further (D-E in Fig. 6.14(c)).

The I–V curves for different devices show some variability due to the simple device structures employed (i.e., direct probing onto contact pads) and due to the statistical variability in the electro-forming process. The resulting I–V curves can be fitted using the proposed MIT model by changing the "effective" geometry of the filament (i.e., the diameter and relative thickness of the filamentary oxide layers), as might be expected to result from different electroforming conditions. Indeed, the model has general applicability and can also be used to model devices with small active regions such as that in Pickett's paper [37]. From an experimental perspective, improvements in uniformity were demonstrated for Pt/NbO_x/TiN structures using more controlled electroforming (series resistance to reduce current overshoot).

Alternative models of the NDR response in NbO_x have also recently been proposed [69,172,173]. These are based on the temperature and field dependence of PF conduction rather than the thermally induced MIT in crystalline t-NbO_2 [37,68]. However, the calculated NDR response in these models critically depends on the assumed temperature and field dependence of the film conductivity as well as accurate modelling of local Joule heating. The uncertainty associated with these

assumptions and the sensitivity of the calculated temperature rise to such parameters makes it difficult to distinguish between the various PF and MIT models. For example, the current MIT model can also generate the NDR response reported by Funck [173]. Recent studies have demonstrated the existence of two distinct NDR regions with dependence on device operating current, one attributed to PF conduction at a low temperature (∼400 K) and the other to a Mott-Peierls transition (∼1000 K).

6.5.3 Oscillation characteristics

To simulate the dynamics of the device in an oscillator circuit, including the frequency and waveform of the device current, the model was extended to include device capacitance (C_{Device}) and circuit capacitance ($C_{Parasitic}$) as shown in the schematic of Fig. 6.16(a). Here, $C_{Parasitic}$ is marked in the circuit schematic which plays an important role in determining the oscillation waveform. The simulation parameters were obtained by fitting the I-V measurement of Fig. 6.14(b) and the current oscillation curves as shown in in Fig. 6.15(a).

The device current oscillations shown in Fig. 6.15(a) are for V_S=1.2 V with a 2 µs pulse. The current waveform in one oscillation period consists of two parts: a rapid current spike followed by a slower decay where the order is opposite to the waveforms of device voltage. Each spike component is associated with the transition of the threshold switching device. In this case, the peak-to-peak amplitudes of the current waveforms (ΔI_{pp}) were measured as ∼0.4 mA, which is ∼21% of the difference between the I_{Th} and I_H ($\Delta I = I_h - I_{th}$ =1.9 mA). This is not the case in VO_2 devices reported by Kim et al., where the ΔI_{pp} is almost the same as ΔI. This difference is related to the ratio between C_{Device} and $C_{Parasitic}$ in the circuit and will be discussed further later. The decay part of the current oscillation can be fitted with an exponential decay curve derived from simple circuit analysis

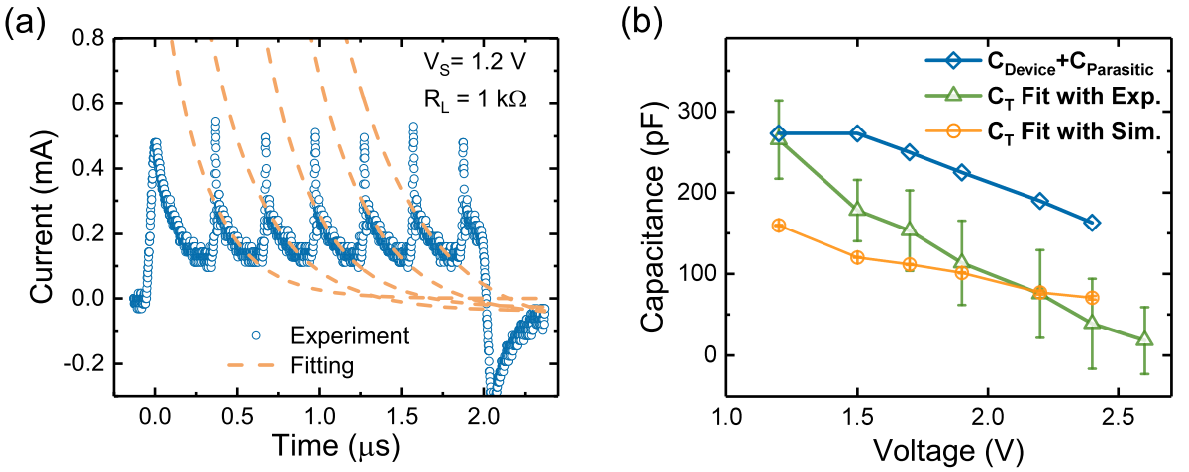

Figure 6.15: (a) Waveforms of device current oscillation. The decay part of the current waveform with fitted exponential decay curves from simple circuit analysis. (b) The total capacitance C_T determined from fits to experimental and simulated waveforms, and the sum of the simulated device capacitance C_{Device} and circuit capacitance $C_{Parasitic}$ as a function of the source voltage. The error bar heights represent the standard deviation over >6 oscillation cycles for each voltage.

$$I_{Device} \propto V_S \left[1 + \frac{R_D}{R_L + R_M} exp\left(-\frac{t - t_0}{\tau}\right)\right] \tag{6.5}$$

where I_{Device} is the current across the device, V_S is the source voltage, and τ is the RC time constant of the circuit. In Fig. 6.15(a), the orange dashed lines show fits to the data with the exponential decay curve of Equation (6.5). Based on the fitted results, C_T was estimated as ~265 pF for a bias voltage of 1.2 V and was found to decrease with the increasing voltage, as shown in Fig. 6.15(b). A similar phenomenon of negative differential capacitance has also been observed in VO_2 films and interpreted as an increase in the fraction of metallic nano-domains within the switching region with increasing voltage [183].

As shown in Fig. 6.16(b), the model captures the periodicity and waveform of the oscillations and reproduces the experimental behaviour very well with the optimal value of C_{Device} = 240 pF, which is close to the value determined from complex impedance spectra reported for micro-sized NbO_x devices [219], and the optimal

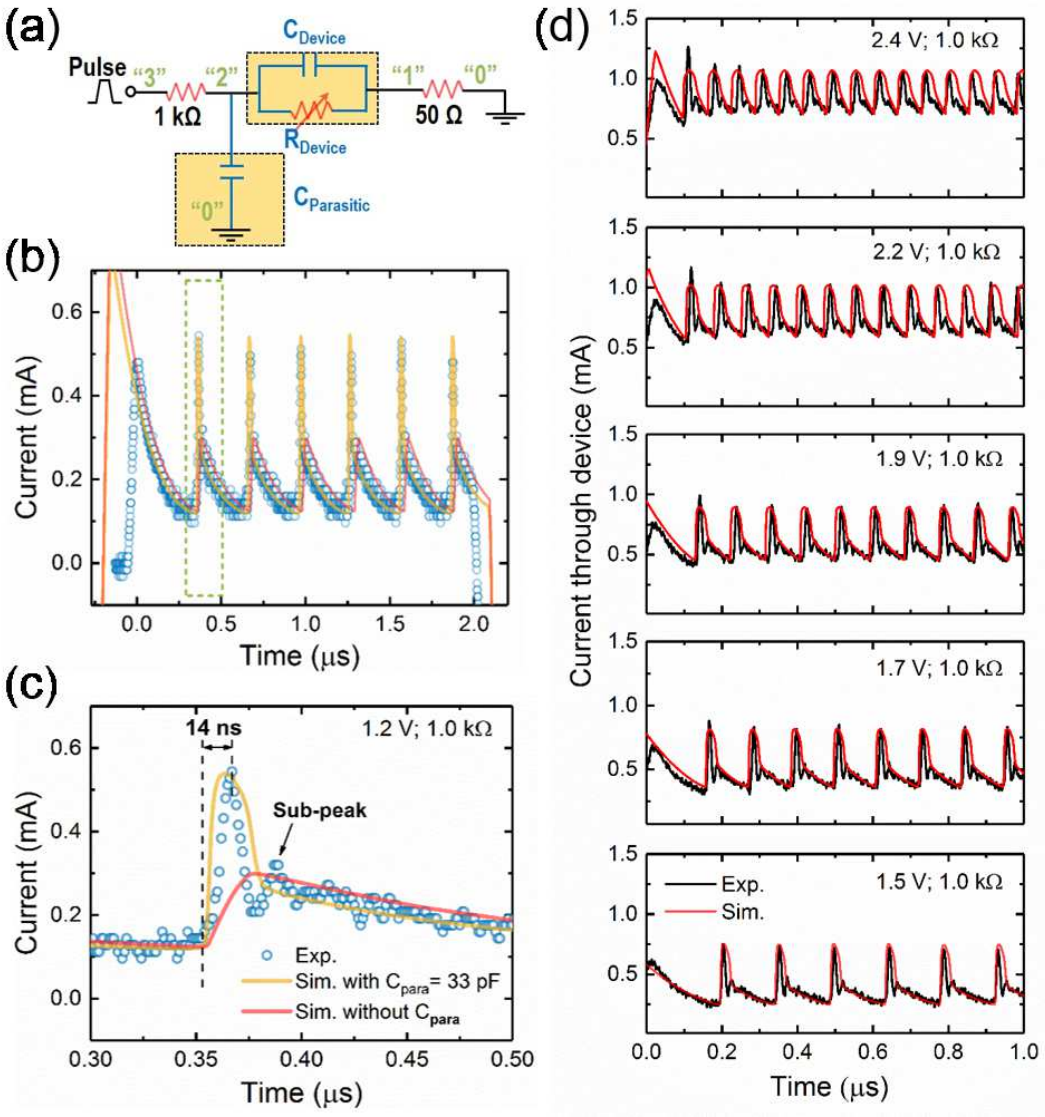

Figure 6.16: (a) Schematic of the electrical circuit used in simulation to study the dynamics of self-oscillations. (b) Measured (black squares) and simulated (red curves) oscillation waveforms of the current through the 50 Ω resistor for a source voltage of V_S=1.2 V (2 μs) and the series resistance of R_L=1 kΩ. The green lines show the simulation data for $C_{Parasitic}$=0 for comparison, where no current spike was observed in the current waveform. (c) Magnification of the dashed rectangle region in (b). (d) Measurements (black curves) and simulation (red curves) of time traces of the current through the device when excited with source voltages ranging from 1.5 V (bottom) to 2.6 V (top) with 1kΩ series.

value of $C_{Parasitic}$ = 33 pF, which is comparable to the measured open circuit capacitance of the measuring system. The calculations show that the current waveform

is sensitive to the value of $C_{Parasitic}$. For example, for $C_{Parasitic}$=0, the current spike disappears, resulting in a sawtooth waveform with the same fundamental frequency, as shown by the red-coloured line included in Fig. 6.16(b).

An expanded view of the current spike region is shown in Fig. 6.16(c). Both the experimental and calculated off-to-on-transition times are ΔT_{ON} = 14 ns, which is consistent with a previous experimental report (∼22 ns) but two orders of magnitude larger than that (∼700 ps) reported by Pickett and Williams [37]. This highlights the effect of the measurement system and device structure on the observed rise time. Measurement of the on-to-off-transition time is complicated in the present case by a sub-peak in the current oscillation which appears to result from the multi-NDR regions in the I-V curves in Fig. 6.2(b). An estimate of ∼4.0 pJ for the total energy input during on-switching can be obtained by noting that the voltage across the device was ∼0.9 V and that numerical integration of the measured current over the transition time is ∼4.4 pC. This is more than one order of magnitude larger than that obtained from Pickett's experiments due to the energy consumption from the intrinsic capacitance [37].

To match the measured pulse characteristics for source voltages above 1.5 V the values of C_{Device} and $C_{Parasitic}$ were first set as constant at 240 pF and 33 pF, respectively. However, the frequency and waveform of simulated device current deviate from the with measured oscillation characteristics as the source voltage increases. The value of C_{Device} and $C_{Parasitic}$ were then adjusted to match the measured oscillation waveforms for other load resistance and source voltages as shown in Fig. 6.16(d) and Fig. 6.17. The sum of C_{Device} + $C_{Parasitic}$ was plotted in Fig. 6.15(b) as a function of source voltages.

Moreover, we fitted our calculated waveforms with the exponential decay curve of Equation (6.5) from simple circuit analysis. Then the obtained C_T for different V_S from the simulation shows the same trend as that from the experimental data, as shown in Fig. 6.15(d). However, these calculated C_T values are not equal to the sum of C_{Device} + $C_{Parasitic}$, due to circuit dynamics. For the voltage pulse of 2.6 V,

the simulated device current does not show oscillation behaviour: this is due to the fact that the voltage exceeds the upper limit of the stable oscillation window, which is limited to the voltage range 1.1 to 2.5 V from load-line analysis of the calculated I-V curve in Fig. 6.14(b). This model can also be used to simulate other measured pulse characteristics for different source voltages with of R_L= 0.5 kΩ, 2 kΩ, and 4 kΩ, as can be seen in Fig. 6.16.

6.5.4 Waveforms and limit cycles

To better understand the device behaviour and the dynamics associated with oscillations, Fig. 6.18(a) shows the relationship between the device voltage V_{Device} and various current components for a single oscillation period in terms of simulation data

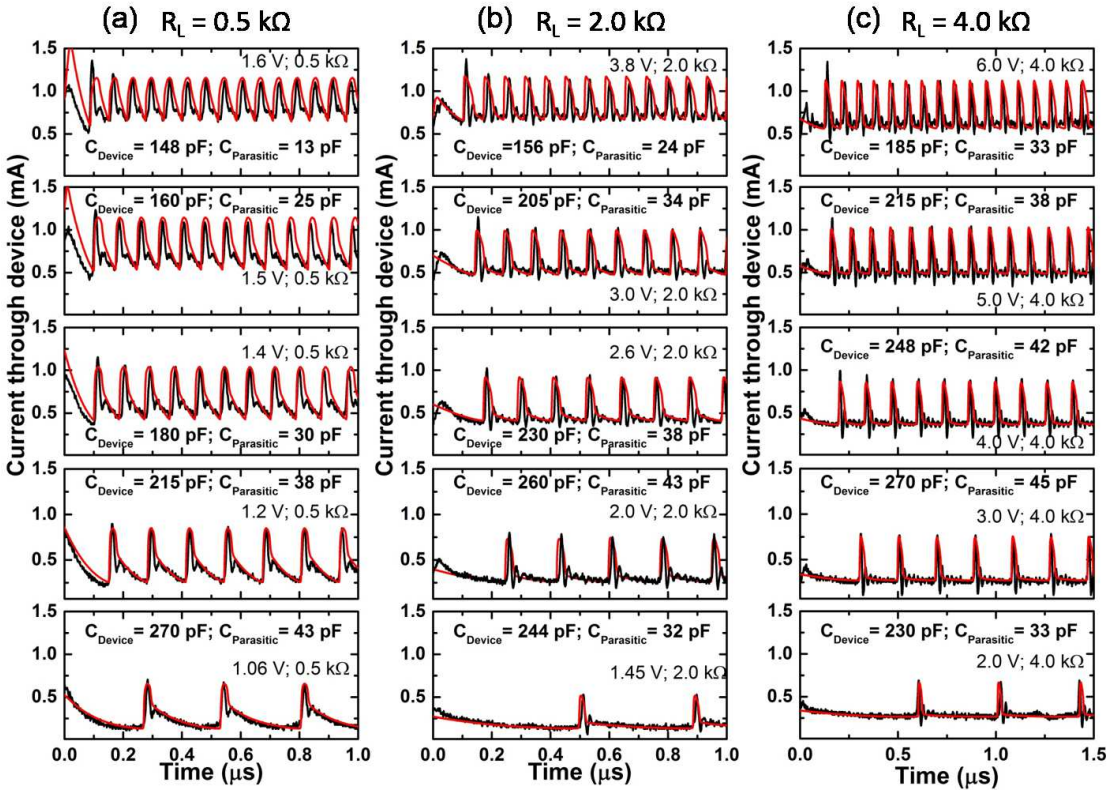

Figure 6.17: Measurements (black curves) and simulations (red curves) of time traces of the oscillation current through the device when excited with source voltages and different series resistor: (a) 0.5 kΩ, (b) 2 kΩ, and (c) 4 kΩ.

for V_S = 1.2 V. The latter include the current due to the resistance of the device (I_{R_device}), the current due to the capacitance of device (I_{C_device}), the total device current I_{Device}, and the current due to parasitic capacitance($I_{C\_parasitic}$). The sequential charging and discharging stages are evident in the V_{Device} trace which is related to the low and high current regions of the I_{R_device} signal. Note that I_{R_device} is positive while I_{C_device} is negative, and the sum of the two currents is the current through the device: $I_{Device} = I_{R\_device} + I_{C\_device}$. This is the origin of the deviation mentioned above where the ΔI_{pp} is less than the current difference between the I_{Th} and I_H. The oscillation waveforms for the total device current have a roughly trapezoidal shape, which is also observed in other experiments [37, 204, 220]. The current through the parasitic capacitance, $I_{C\_parasitic}$ is also negative due to the charging and discharging of $C_{Parasitic}$, which also influences the waveform of I_{Device}. As a consequence, the peak of I_{Device} occurs concurrently with the minimum of $I_{C\_parasitic}$, but it has ∼6 ns delay compared with the maximum of I_{R_device}, as shown in Fig. 6.18(a). Consequently, the oscillation frequency, the waveform of I_{Device}, the peak-to-peak current amplitude, and even the off-to-on-transition time are affected by C_{Device} and $C_{Parasitic}$, as discussed later.

Replotting the I_{Device}–V_{Device} response for V_S = 1.2 V defines a limit cycle as shown by the red line in Fig. 6.18(b), which is a characteristic of self-sustained oscillators [39, 221, 222]. The I_{R_device}–V_{Device} response (blue line) is also plotted in Fig. 6.16(b), and is shown to roughly match the hysteresis region of the voltage sweeping I-V curves (dashed line). In relation to the current sweeping I-V curves (dotted line), four characteristic points for a cycle of I_{R_device} oscillation are marked in Fig. 6.18(b), which corresponds to those in Fig. 6.14(b). Region B-E represents the transition from insulating to metallic state, E-D corresponds to the device in a metallic state, D-A represents the transition from metallic to insulating state, and A-B corresponds to the device in its insulating state. The oscillation mechanism can then be described as follows: (a) Starting from the threshold-bias point B, the current rises to the on-state point E upon switching as a result of the total capacitance

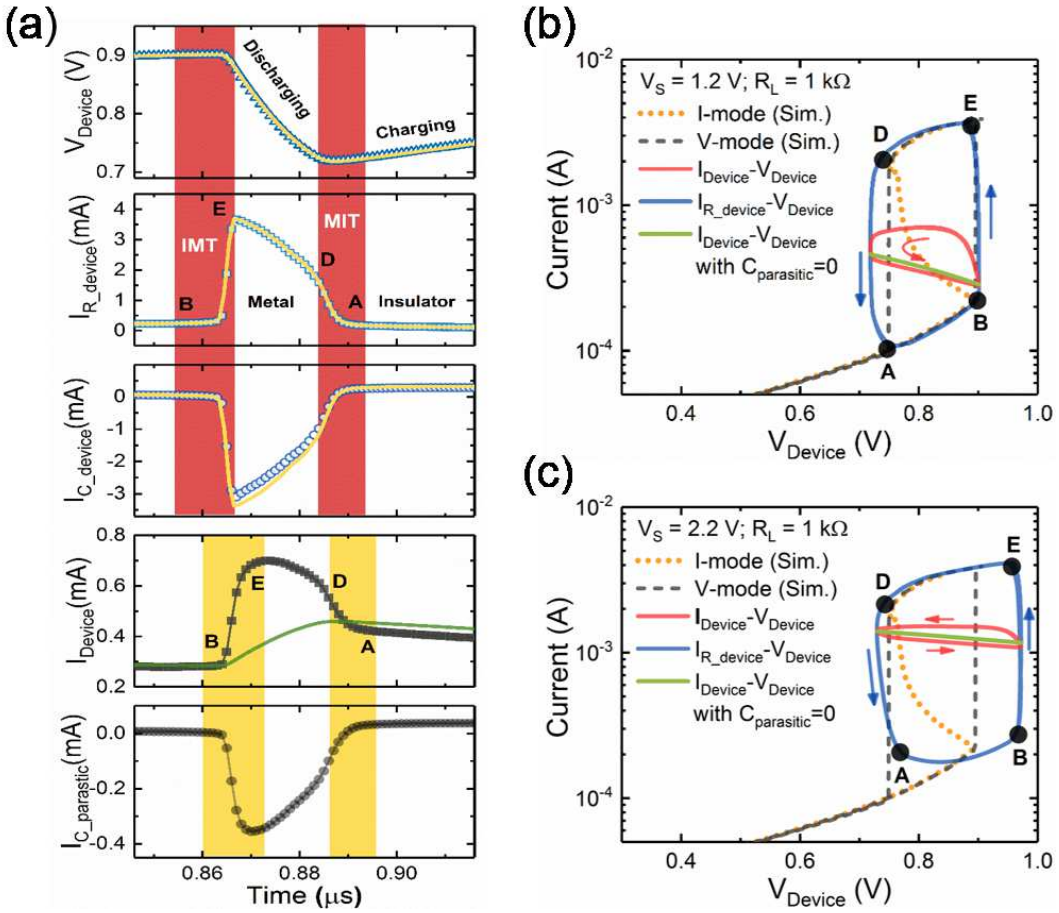

Figure 6.18: (a) Calculated device voltage, V_{Device}, and related current components: I_{R_device}, I_{C_device}, I_{Device}, and $I_{C\_parasitic}$ for a source voltage of $V_S = 1.2$ V and load resistance of $R_L = 1k\Omega$. (b) and (c) Show the limit cycles of I_{Device}–V_{Device} (red lines) for $V_S = 1.2$ V and 2.2 V, respectively. The green lines show the simulation data of I_{Device}–V_{Device} with $C_{Parasitic} = 0$, where the limit cycles collapse to straight lines. The blue lines show the I_{R_device}–V_{Device} characteristics. The black lines show the I-V response of the device under voltage-controlled (dashed) and current-controlled (dotted) operation for comparison.

(C_T) in the circuit; (b) the current decreases to point D of the I_{R_device}–V_{Device} characteristic as the capacitance discharges, and then, the current falls to the off–state point A due to the MIT; (c) then the voltage increases as the capacitance charges, and a new cycle of oscillation begins once the threshold-bias point B is reached.

The corresponding four characteristic points are also marked in Fig. 6.18(a) to determine the transition time. The rise time of 14 ns from B to E in the simulation of

I_{R_device} and I_{Device} is consistent with the experimental value as shown in Fig. 6.16(c). Here, each spike component can be related to the insulator-to-metal transition (B-E), metal (E-D), and metal-to-insulator transition (D-A), while each decay component can be related to the insulator state (A-B) of the device. The corresponding time was defined as t_{IMT}, t_{metal}, t_{MIT}, and $t_{insulator}$. For the case of V_S = 1.2 V and R_L = 1kΩ, the oscillation period is $T_{osc} = t_{IMT}+t_{metal}+t_{MIT}+t_{insulator}$ = 14+17+10+266 = 307 ns. All four stages can be tuned by appropriate control of the bias voltage, a series resistor, and an external capacitance. The oscillation frequency f_{osc} can be tuned accordingly.

Similarly, the I_{Device}–V_{Device} response for V_S = 1.2 V and R_L = 1kΩ, also defines a limit cycle as shown by the red line in Fig. 6.18(c). In relation to the voltage sweeping I-V curves (dashed line), the I_{R_device}–V_{Device} response represents a deformed hysteresis region as shown by the blue line in Fig. 6.18(c), which is a dynamic feature due to the high frequency. Note that if the $C_{Parasitic}$ = 0, the limit cycle collapses to a straight line for both V_S = 1.2 V and 2.2 V case with R_L = 1 kΩ, as shown by the green lines in Fig. 6.18(b) and Fig. 6.18(c).

6.5.5 Capacitance dependence

The tunability of this Ti/NbO_x oscillator, including the effect of device and parasitic capacitances on the operating frequency, is explored through two sets of simulations: (1) C_{Device} is varied from 1 pF to 2 nF and the other parameters are kept constant (V_S = 1.2 V, R_L = 1 kΩ, and $C_{Parasitic}$ = 33 pF); (2) $C_{Parasitic}$ is varied from 1 pF to 5 nF and the other parameters are kept constant (V_S = 1.2 V, R_L = 1kΩ, and C_{Device} = 240 pF). Results show that both the oscillation wave shape and frequency depend strongly on C_{Device} and $C_{Parasitic}$. Fig. 6.19(a) and (b) show the current-time characteristics of simulated, self-sustained oscillations for various capacitance values, where the effects of capacitance can be clearly observed. The peak-to-peak amplitudes of the total device current (ΔI_{pp}) decrease significantly when C_{Device}

reaches 500 pF (Fig. 6.19(a)), since a larger device capacitance stores and discharges more charge. By increasing C_{Device}, I_{C_device} increases accordingly and ΔI_{pp} decreases. In contrast, ΔI_{pp} increases significantly when $C_{Parasitic}$ changes from 1 pF to 1 nF (Fig. 6.19(b)). Finally, ΔI_{pp} increases proportionally with the ratio of $C_{Parasitic}$ and C_{Device} and then tends to saturate, as shown in Fig. 6.19(c).

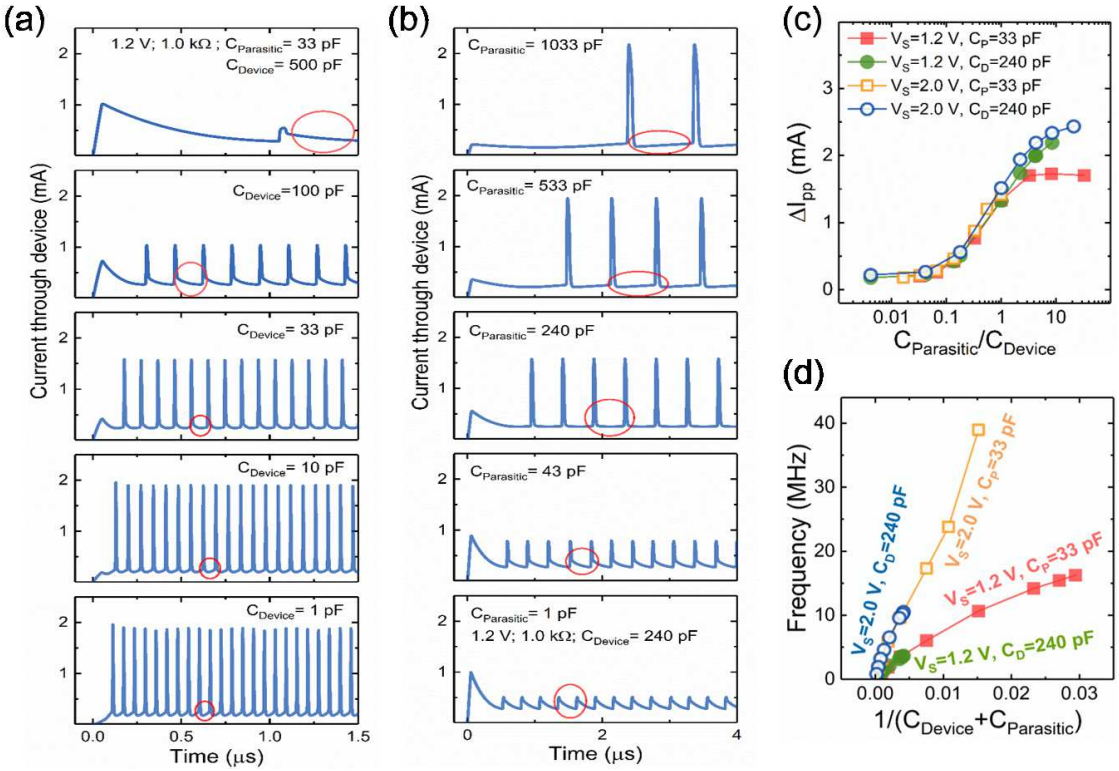

Figure 6.19: (a) Waveforms of I_{Device} as a function of the device capacitance C_{Device}, and (b) as a function of the parasitic capacitance $C_{Parasitic}$. (c) The dependence of the peak-to-peak device current on the ratio of $C_{Parasitic} = C_{Device}$. (d) The dependence of the oscillation frequency on the sum of CDevice and CParasitic.

The physical transition times in a nanoscale NbO_2 device between on and off states have been reported to be ∼700 ps for the insulator-to-metal transition and 2.3 ns for the metal-to-insulator transition [37], which indicates that the maximum achievable frequency for these oscillators is expected to be ∼GHz. However, the oscillation frequency is determined by the resistor-capacitor time constant associated with charging/discharging, and in most cases, the peak frequency is limited by

$C_{Parasitic}$ and C_{Device}. Fig. 6.19(d) indicates that the frequency is inversely proportional to the sum of $C_{Parasitic}$ and C_{Device}. To increase the frequency, clearly both the $C_{Parasitic}$ and C_{Device} should be reduced. This suggested as the advantage of nanoscale devices for high-frequency operation.

6.6 Summary

The electrical self-oscillation behaviour of an NbO_x CC-NDR device was investigated experimentally and with reference to a finite element model of the switching response based on a thermally induced MIT. Room temperature electrical oscillation was demonstrated for a circuit containing the NbO_x device, and shown to be directly related to the presence of the NDR region in the I-V characteristic of the device operated in the current mode. Devices were further shown to display sporadic, relaxation, and damped oscillations depending on the applied voltage and series resistance. The voltage range over which CC-NDR is observed, decreases with increasing temperature, up to 378 K. Up to this temperature, relaxation oscillators exhibit voltage and temperature dependent oscillation frequencies and the sensitivity of the frequency to temperature changes was found to be voltage-dependent.

A Joule-heating induced electro-thermal threshold switching model based on the finite element method was presented and shown to reproduce the I-V characteristic of the device. Based on this model, the switching dynamics of the electrical circuit which included the CC-NDR device were investigated. The waveform of the device voltage and current were discussed in detail with reference to the model predictions. The model highlighted the role of circuit and device capacitance in controlling the oscillation frequency and current amplitude.

Chapter 7

Coupled NbO_x Oscillators

7.1 Introduction

Coupled oscillatory systems exhibit rich dynamics that have attracted considerable scientific interest over many years [25, 223, 224]. The process of synchronisation not only governs fundamental physical, chemical and biological systems in nature, including neural oscillations, circadian rhythms and thalamo-cortical systems [225–228], but also underpins the development of a diverse range of novel applications in physics and engineering [184, 229, 230].

A particular focus in recent years has been the development of compact, low-power solid-state relaxation oscillatory networks for neuromorphic computing applications, such as real-time spatio-temporal recognition [231]. This is based on the fact that such networks have been shown to emulate the functionality of computational neurons [18, 186, 232]. Devices of interest include those based on threshold switching, or current-controlled negative differential resistance (CC-NDR), in strongly correlated oxides.

In this chapter, we experimentally investigate the coupling dynamics between two Nb/Nb_2O_5 CC-NDR driven oscillators. The oscillation characteristics of each isolated oscillator are studied and their distinct differences are examined. The behaviour of the coupled systems is explored experimentally by introducing a coupling capacitor and studied as a function of source voltage and coupling capacitance. The experimentally measured coupling modes were compared and explained with a physics-based finite element model.

7.2 Experimental details

Devices were fabricated on a thermally oxidised Si wafer, with a bottom electrode comprised of a 10 nm Ti wetting layer, a 25 nm Pt layer and a 10 nm Nb layer deposited by electron beam evaporation without breaking vacuum. A 20 nm Nb_2O_5 layer was subsequently deposited on the bottom contact by RF sputter deposition using an Nb_2O_5 target as the source. Circular Pt top contacts (50 nm thick and 150 um diameter) were then deposited by electron beam evaporation through a shadow mask to complete the test devices. Completed devices were subsequently encapsulated with a 40 nm SiNx layer deposited by plasma enhanced chemical vapor deposition at 300 °C (2 min). This served to protect the devices from the ambient and provided a low temperature anneal to sinter the contacts and stabilize the structures. A cross sectional transmission electron microscope (TEM) view of a complete device structure is shown in the inset of Fig. 7.1(a).

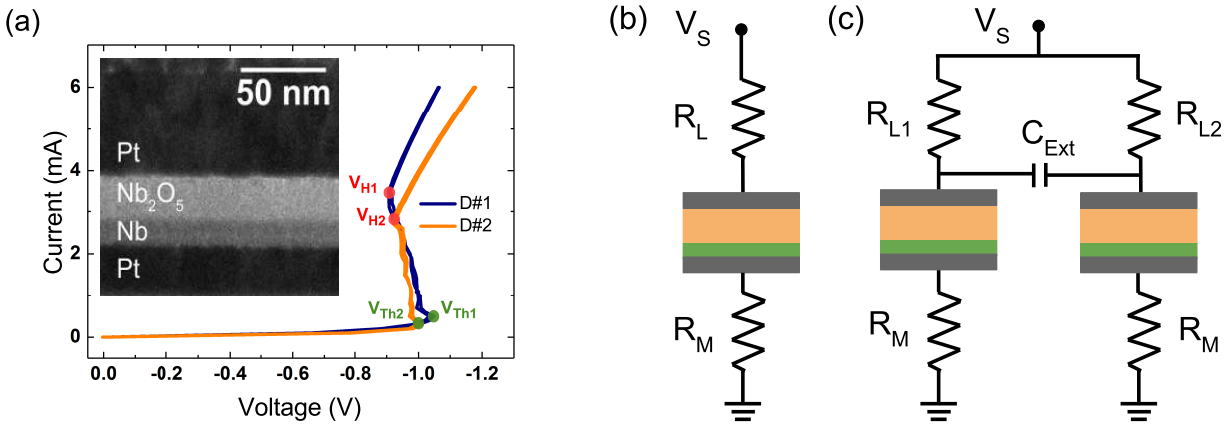

Figure 7.1: (a) NDR responses of isolated devices under a I-V sweep. Inset shows TEM cross section of the device structure. (b) Circuit configuration for single-device oscillator (c) Circuit configuration for coupled oscillator systems.

Before electrical measurements top electrodes were opened by wet etching and the initial I-V curves of the devices in their pre-switching state exhibit rectifying characteristics, as shown in Fig. 7.2(a). To initiate the threshold switching, an electroforming process is necessary, as shown in Fig. 7.2(b). This involved a voltage sweep

from 0 V to -5 V with a 200 μA compliance current to induce soft breakdown. Stable CC-NDR was then achieved after several stabilising switching cycles. The CC-NDR response is believed to result from the development of an interlayer at the Nb/Nb_2O_5 interface in the vicinity of the residual conductive filament. The development and stabilisation of this interlayer is enhanced by local Joule heating during electroforming and the first few switching cycles, and is limited to the region around the filament due to its current confining effect. Stabilisation of the interlayer is expected after the first few switching cycles and devices then show reproducible CC-NDR characteristics. Current-voltage (I-V) characteristics were measured using an Agilent B1500A semiconductor parametric analyzer attached to a Signatone probe station.

Fig. 7.1(a) shows quasi-DC I-V characteristics for two Nb/Nb_2O_5 devices under current-controlled sweeps. As the current through the device-under-test (DUT) increases, the voltage also initially increases up to a threshold value after which it decreases with increasing current. The latter response corresponds to a region of negative differential resistance due to an increase in conductivity with increasing current. This region is bounded by the threshold voltage, V_{Th1} and V_{Th2}, and the hold voltage, V_{H1} and V_{H2}. Under voltage-controlled I-V measurements the current

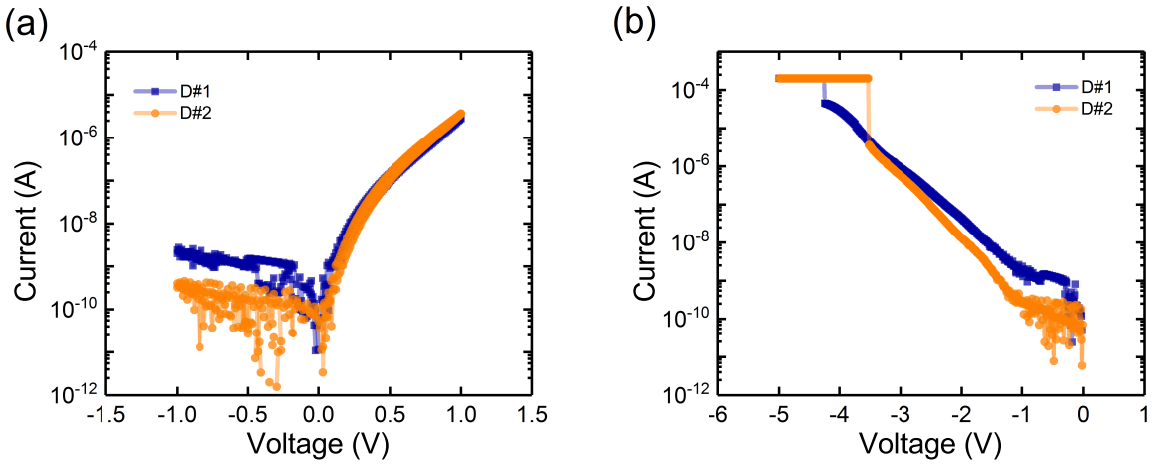

Figure 7.2: ((a) The initial I-V curves of the two $Pt/Nb_2O_5/Nb/Pt$ devices in their virgin (pre-switching) state exhibit a rectifying characteristic. (b) Electroforming process with 200 μA compliance current for the two devices.

increases rapidly at the threshold voltage due to the positive feedback created by the nonlinear increase in conductivity [51]. In both cases the change is volatile, with the conductivity returning to its initial state when the current (voltage) is reduced.

7.3 Individual oscillator response

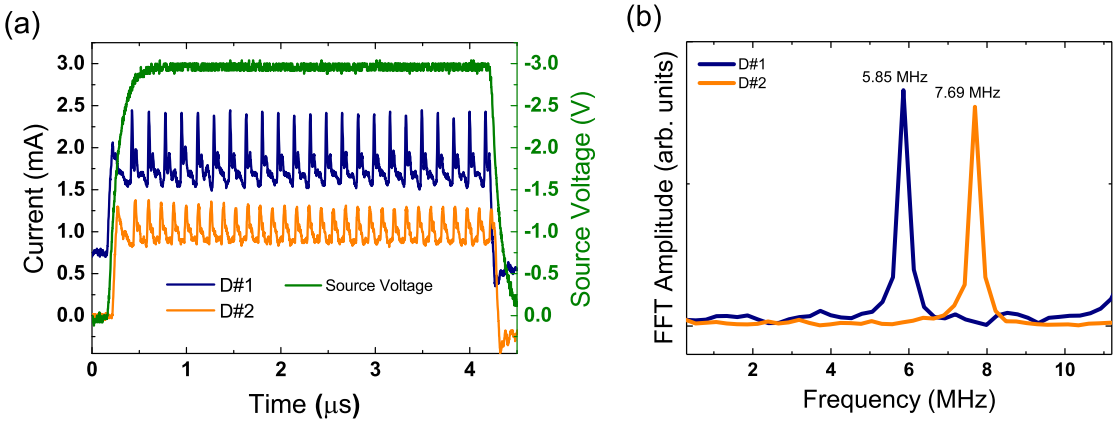

Figure 7.3: (a) Device current of isolated oscillators during excitation with 4 μs, -3 V pulse. D#1 current has been vertically offset upwards by 0.7 mA for clarity. (b) FFT amplitude spectra of accompanying current signals for D#1 and D#2 with -3 V excitation.

To study the individual oscillator response, devices were incorporated in a simple Pearson-Anson circuit as shown in Fig. 7.1(b). This comprised a load resistor R_L and a 50 Ω monitoring resistor (R_M) in series with the DUT. The source voltage,V_S, was applied as a pulse of 4 μs duration. The resulting oscillation waveforms are shown in Fig. 7.3(a) for R_L = 1 kΩ and V_S = -3 V. The rise and fall of the device current corresponds to the dynamic transition between low and high resistance states in the DUT. Device 1 (D#1) and Device 2 (D#2) exhibit their own natural oscillation frequencies at 5.85 MHz and 7.69 MHz, respectively as shown in Fig. 7.3(b). The differences in natural oscillation frequency and device peak-to-peak currents reflect the different CC-NDR characteristics of the individual devices shown in Fig. 7.1(a). More detailed analysis of these single oscillator dynamics was described in Chapter 6. Suf-

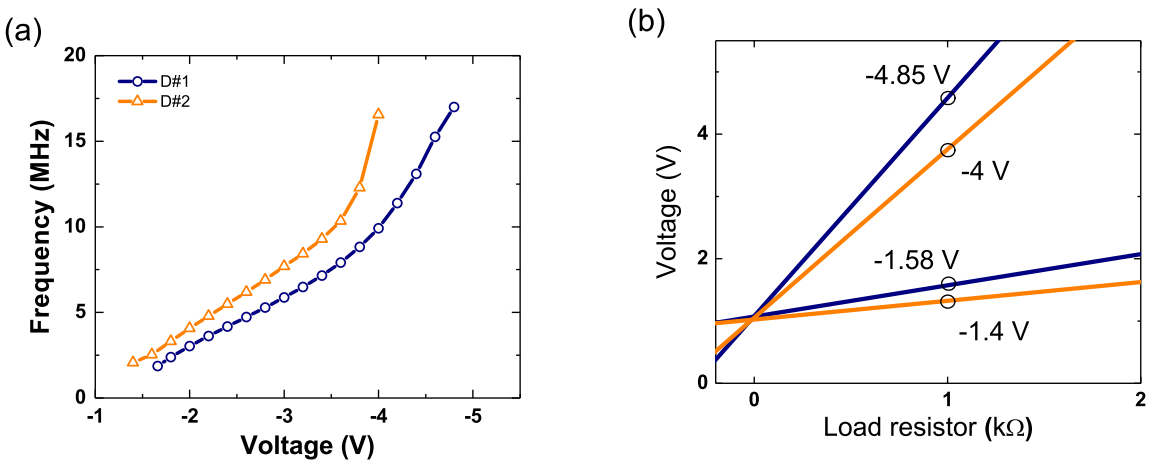

Figure 7.4: (a) Plot of the isolated oscillator frequency as a function of source voltage. (b) Oscillation window defined by V_S and R_L for D#1 and D#2.

fice it to say that oscillation is the result of the switching response of the DUT in combination with the voltage divider created by the load resistor, with the oscillation frequency determined largely by the bias voltage and the RC time constant of the circuit, including both intrinsic and parasitic contributions. As a consequence, the frequency of the individual devices can be tuned by adjusting the load resistor, R_L, and source voltage, V_S.

The fundamental frequencies of each oscillator as function of the applied voltage are shown in Fig. 7.4(a). This shows an approximately linear dependence on V_S for frequencies up to 8∼10 MHz, and a more rapid increase at higher frequencies due to a reduction in the capacitive reactance. The minimum and maximum frequency limits for D#1 are between 1.69 MHz and 17.04 MHz and for D#2 they are 2 MHz to 16.59 MHz, respectively. Fig. 7.4(b) shows the bounded region as the oscillation window for D#1 and D#2. It clearly illustrates the distinct differences between their oscillation windows. For instance, with a fixed load resistance of 1 kΩ, D#1 is capable of sustaining self-oscillation for voltages in the range from -1.8 V to -4.85 V while D#2 has a voltage tunable range from -1.4 V and -4 V. The distinct oscillation frequency and voltage tunability are particularly interesting for capacitive coupling between D#1 and D#2.

7.4 Voltage and coupling capacitance effect

The effect of coupling these two devices was investigated using the circuit configuration shown in Fig. 7.1(c), where the external variable capacitor (C_{Ext}) was used to control the coupling strength. The variable capacitor is configured to have a minimum value of 35 pF and to increment in 100 pF steps. For the measurements presented here, the load resistors, R_{L1} and R_{L2}, had the same fixed value of 1 kΩ, and the switching dynamics of the individual oscillators were monitored through 50 Ω resistors in series with each device. A typical synchronisation mode is shown

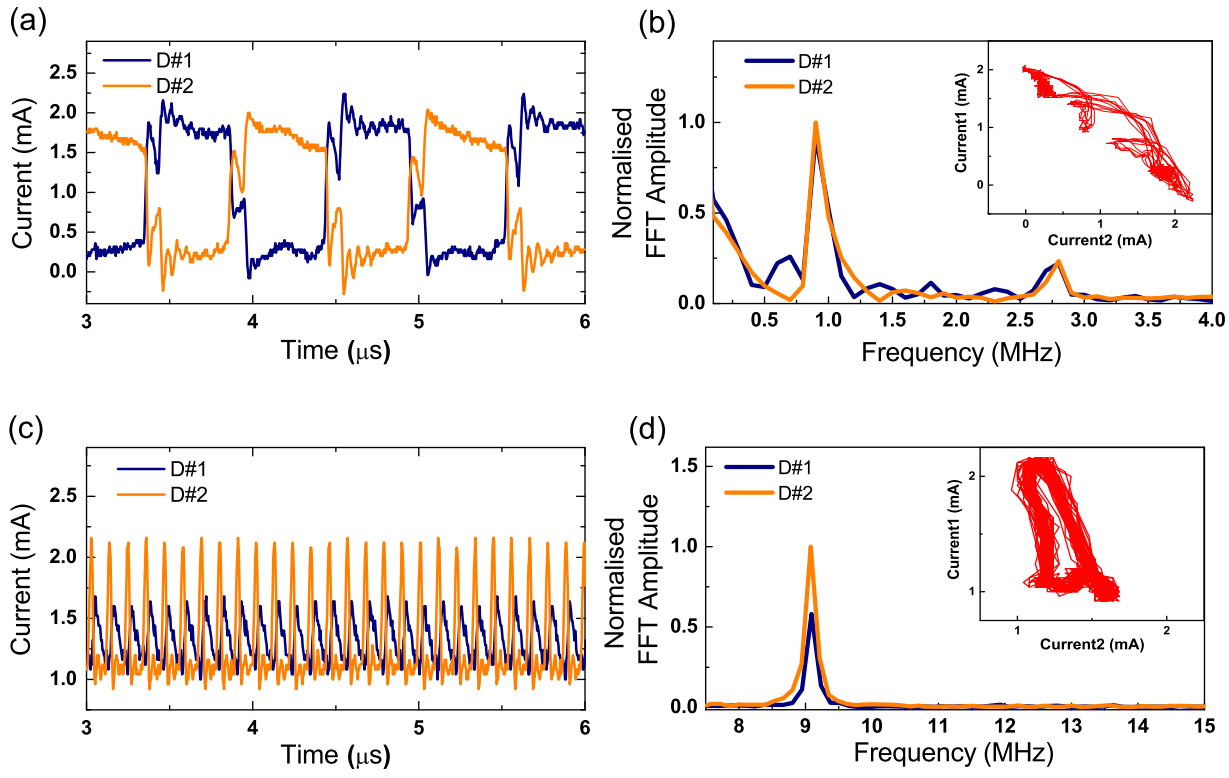

Figure 7.5: (a) Device currents for oscillators coupled with a 2035 pF external capacitor during excitation with an 8 μs, -3 V voltage pulse. (b) FFT amplitude spectra of the accompanying current signals for -3 V excitation. Inset shows a current phase-space diagram for the coupled devices. ((c) Individual device currents for oscillators coupled with a 2035 pF external capacitor during excitation with an 8 μs, -3.6 V voltage pulse. (d) FFT amplitude spectra of accompanying current signals for -3.6 V excitation. Inset shows a current phase space diagram for the coupled devices.

in Fig. 7.5(a) for C_{Ext} = 2035 pF and V_S = -3 V. In this case, the oscillators exhibit antiphase oscillations and have a peak-to-peak current in the range ∼0.2 mA to 2 mA. The underlying dynamics are such that when device D#1 switches from a LRS to a HRS, device D#2 concurrently transits from a HRS to a LRS, producing a 180^o phase relationship in device current between the two oscillators. Fast Fourier Transform (FFT) spectra of the coupled oscillators are presented in Fig. 7.5(b) and show that the coupled system operates with a unique synchronised frequency of 0.9 MHz, much lower than that of the isolated oscillators in this case. The inset in Fig. 7.5(b) shows phase-space trajectories for the device currents. These trace closed loop trajectories, consistent with synchronisation, but have a complex form due to the fine structure in the current oscillation waveforms.

When the source voltage is increased to -3.6 V, the oscillation frequency increases and the relative phase difference between the individual oscillators decreases, as shown in Fig. 7.5(c). The accompanying FFT spectra (see Fig. 7.5(d)) show that the oscillators now have a mutual frequency of 9.08 MHz which is between their natural frequencies of 8 MHz and 10.28 MHz, respectively. The inset in Fig. 7.5(d) shows the phase-space trajectories for this case, again highlighting a closed loop structure consistent with coupled oscillation, and a simplified form compared to that in Fig. 7.5(b) due to the simpler current waveforms. This behavior can be broadly understood by noting that the reactance of the coupling capacitor decreases with increasing frequency (or increasing capacitance) thereby leading to more direct, (i.e. lower impedance) coupling.

The effect of source voltage and coupling capacitance on individual oscillator frequencies is shown more generally in Fig. 7.6. Fig. 7.6(a) plots the oscillator frequencies as a function of source voltage for a fixed coupling capacitance of 2035 pF and highlights three distinct coupling regimes. This behaviour can be understood conceptually by considering the response of device D#2 to changes in device D#1 (see the circuit in Fig. 7.1(c)). When device D#1 switches from one state to another it produces a voltage difference across the coupling capacitor. This induces a current to

flow through R_{L2} and device D#2 and changes the voltage across device D#2. For the lowest source voltages (Region I) this contribution has little effect on switching and the devices switch at their natural frequencies. As the source voltage increases, the coupling contribution also increases to the point where it affects switching in device D#2. Device switching then becomes more interdependent, with switching in device D#1 influencing switching in device D#2, and vice versa. While such arguments underpin the general trends in Fig. 7.6(a) the behaviour is much more complex due to the mutual interaction of the oscillators and can only be captured by more detailed modelling. This is particularly evident from the discontinuous behaviour between Regions I and II and Regions II and III. Specifically, in Region II the mutual operating frequency is found to be relatively independent of the source voltage and is lower than that of the individual oscillators, having a frequency equals to $(f_2 - f_1)/2$ where f_1 is the frequency of device D#1 and f_2 is the frequency of device D#2, and the device currents are frequency- and phase-locked with a phase difference of 180^o. In contrast, at higher source voltages (Region III), the mutual frequency is $(f_1 + f_2)/2$ and a constant phase-difference of approximately 130^o.

Fig. 7.6(b) shows the coupling frequency as a function of coupling capacitance

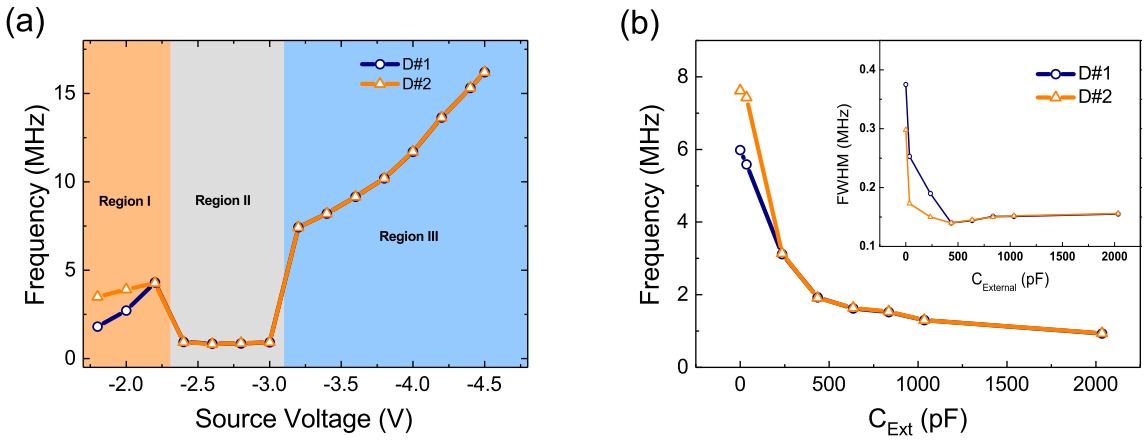

Figure 7.6: (a) Frequency of coupled oscillators as a function of source voltage for C_{Ext} = 2035 pF. (b) Change in the coupling frequency and the coupling strength (inset) as a function of C_{Ext} for V_S = -3 V.

for a fixed source voltage of -3 V. For relative low capacitances (<235 pF) the oscillators are only weakly coupled and oscillate with different frequencies. As the capacitance increases to ≥235 pF, the devices synchronise and oscillate with a common frequency that decreases with increasing capacitance due to longer charging and discharging cycles. The inset in Fig. 7.6(b) shows the full width at half maximum (FWHM) of the dominant FFT peak as a function of coupling capacitance. The reduced FWHM reflects the stronger coupling interaction and stable synchronisation due to the mutual feedback [233].

7.5 Numerical modelling of coupling dynamics

For further understanding of the coupling mechanism, different synchronisation modes of the coupled systems have been simulated based on the extension of our previous modelling work [187]. A Joule-heating induced electro-thermal threshold switching model based on the finite element method (FEM) was presented and shown to reproduce the current-voltage (I-V) characteristic of the device. We extended our previous work to explore synchronization of NbO_x coupled oscillators for computational applications.

Fig. 7.7(a) shows the schematic structure of the Pt/Nb_2O_5(25 nm)/Nb(10 nm)/Pt test device and the electrical measuring conditions. To reproduce the I−V curves, a two dimensional (2D) axis-symmetric finite element simulation model was solved self-consistently in a time-dependent solver. The details of the simulation parameters are previously discussed in Section 6.5. Similar with our previous simulation conditions, the model considers a NbO_2/NbO current channel (filament) surrounded by oxygen-deficient Nb_2O_{5-x} as the simulated cell as shown in Fig. 7.7(b), where the size of the effective NbO_2 zone is adjustable according to the I−V curves after electroforming. Here, the effective NbO_2 zone for D#1 is used as a small active region with 100 nm diameter and 20 nm thickness, while the effective NbO_2 zone for D#2 is used as a small active region with 90 nm diameter and 25 nm thickness.

As shown in Fig. 7.8(a) and Fig. 7.8(b), the calculated I-V characteristics are able to match the threshold and hold points within the NDR region which provides the fundamental basis of self-sustained oscillation in each device.

To reproduce the waveforms and dynamics of an isolated oscillator, the same circuit configuration was adopted in the simulation as described in Section 6.5 of Fig. 6.16(a). The oscillator is composed of a NbO_x device in series with a load resistor (R_L). The NbO_x device is assumed to be composed of a variable resistance (R_D) and an intrinsic capacitance (C_D). Sufficient amount of source voltage (V_S) was applied in order to initiate the oscllation. A parasitic capacitance (C_P) is assumed in the circuit. The waveforms and dynamics of an isolated oscillator were reproduced when the NDR device based on the FEM model is combined with circuit elements, as shown in Fig. 7.9(a) and Fig. 7.9(b). Here, the C_{D1} =847 pF and C_{P1} = 178 pF were used for D#1, while the C_{D2} =485 pF and C_{P2} = 70 pF were used for D#2.

To study the dynamics of coupled oscillators, the electrical circuit configuration used in the simulation is shown in Fig. 7.10. Electrical coupling of two oscillators

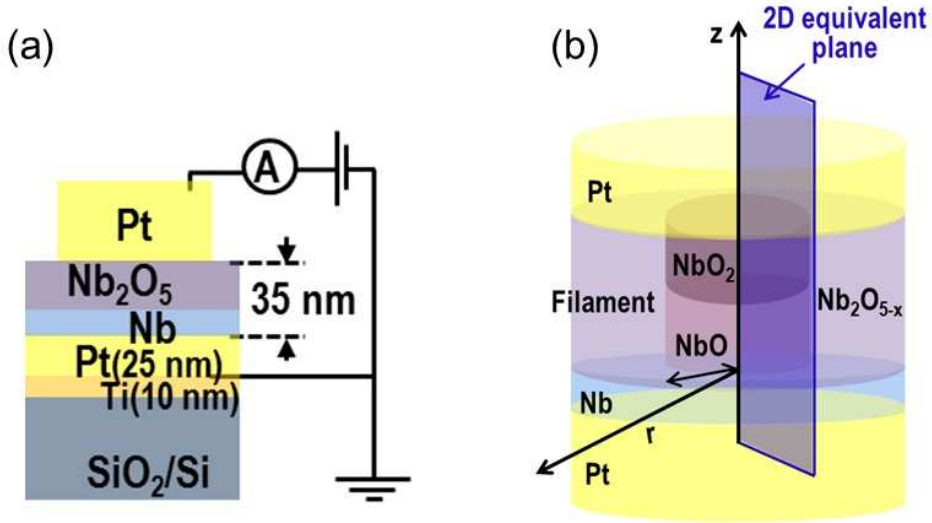

Figure 7.7: (a) Schematic of the fabricated $Pt/Nb_2O_5/Nb/Pt$ test devices and the measuring conditions. (b) Geometry of the simulated device structure assuming a cylindrical conductive channel (filament) comprised of NbO2/NbO zones and surrounded by an Nb_2O_{5-x} matrix.

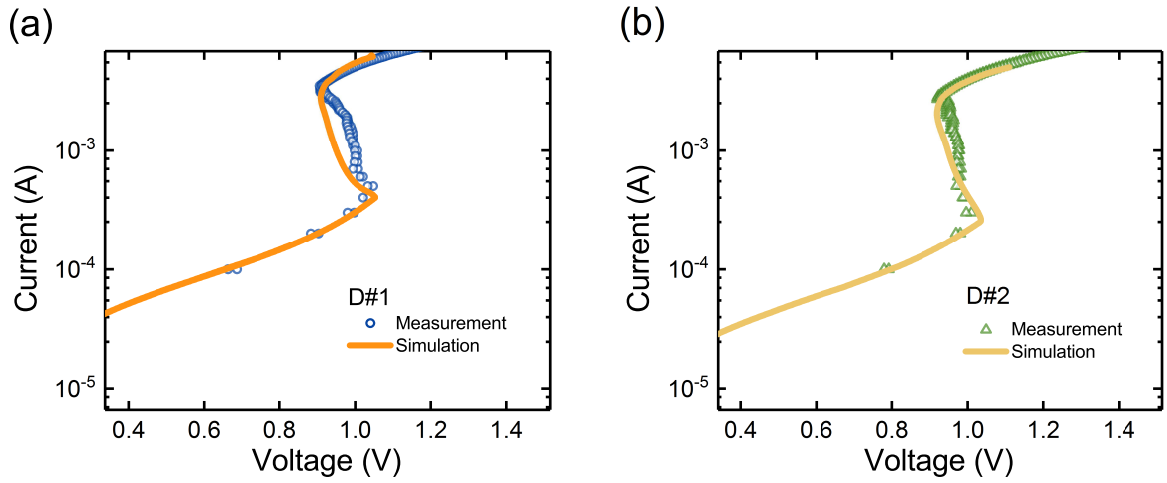

Figure 7.8: Measured and simulated I-V curves with clear NDR characteristics in current-sweeping mode for (a) D#1 and (b) D#2.

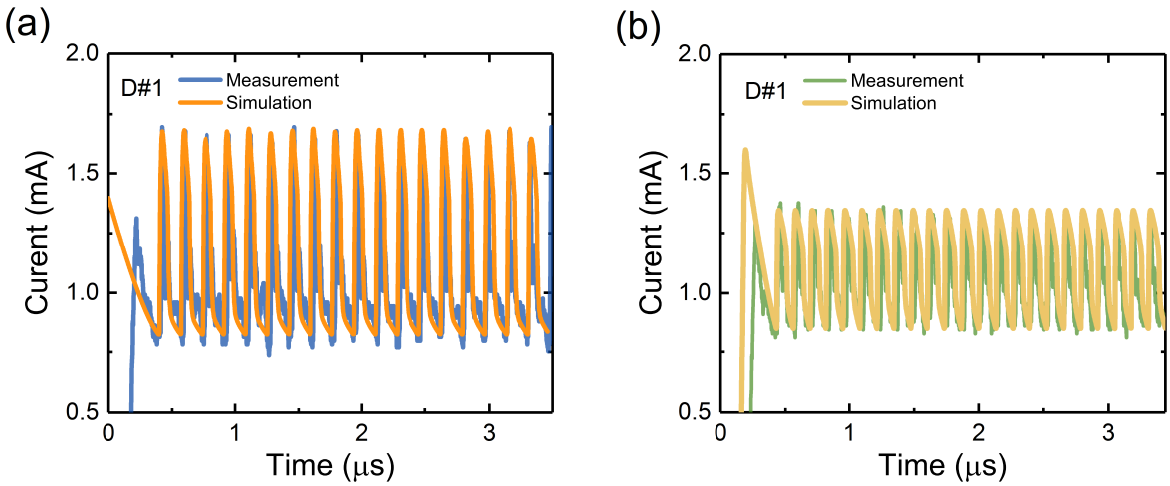

Figure 7.9: (a) Measured and simulated oscillation waveforms of current through the 50 Ω resistor for D#1 with a source voltage of V_S = -3.0 V and R_L = 1 kΩ. (b) Measured and simulated oscillation waveforms of the current for D#2.

is enabled through a coupling capacitor (C_{Ext}). The FEM simulation demonstrated the dependence of coupling modes on C_{Ext}.

Fig. 7.11 shows simulated current dynamics for oscillators coupled with two different coupling capacitances and operated with a fixed source voltage of -3 V. The coupled oscillators exhibit antiphase synchronisation with a 835 pF coupling capa-

citor (see Fig. 7.11(a)), and a reduced phase offset when the coupling capacitance is increased to 1535 pF (see Fig. 7.11(c)). The corresponding FFT spectra and current flow trajectories are shown in Figs. 7.11(b) and (d), respectively. The data in Fig. 7.5 and Fig. 7.11 highlight the fact that the synchronisation dynamics depend on source voltage (oscillator frequency) and coupling capacitance, consistent with expected changes in the coupling reactance (i.e. $X_C = [2\pi fC]^{-1}$) where an increase in frequency or capacitance leads to a decrease in reactance of the coupling capacitor. Fig. 7.12(a) shows the corresponding dynamics of time domain waveforms (V_1 and V_2) for the two NbO_x oscillators with capacitively coupling (C_{Ext}=835 pF). After an initial unsynchronized period of ~1 μs, they frequency lock and converge to a single resonant frequency (3.28 MHz). Fig. 7.12(b) shows voltage flow diagrams in phase space. In contrast to the disordered trajectory for $C_{Ext} \leq 75$ pF, a steady state butterfly shaped orbit is obtained in the synchronized case. Fig. 7.13(a) shows the simulated time domain waveforms (V_1 and V_2) for the two NbO_x oscillators with

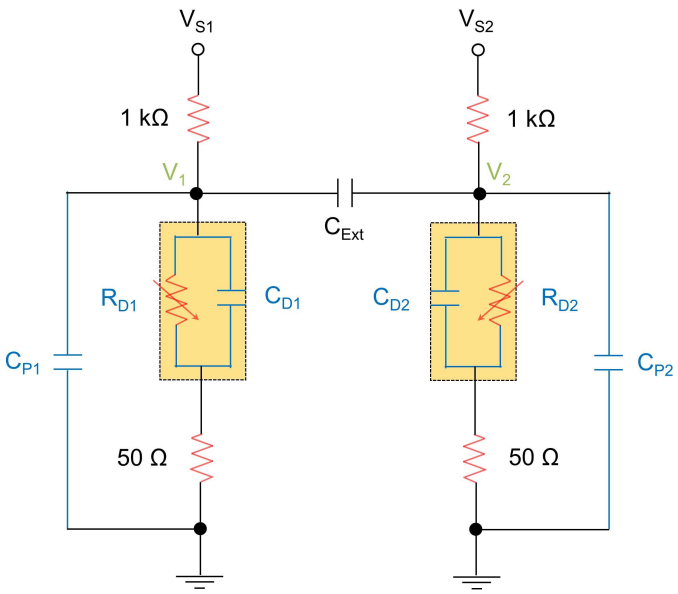

Figure 7.10: Schematic of coupled oscillators, where each individual oscillator is composed of a NbO_x device in series with a load resistor (R_L) and electrical coupling is enabled through a coupling capacitance (C_{Ext}).

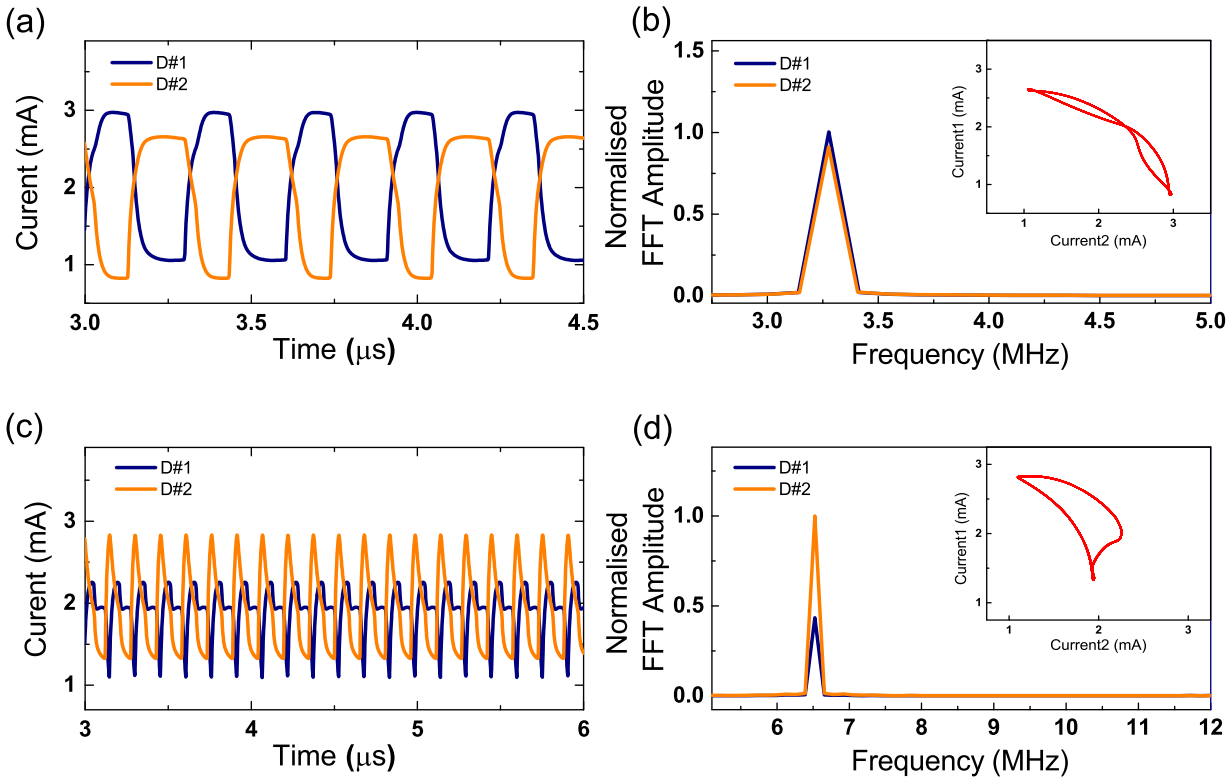

Figure 7.11: (a) Simulated device currents for oscillators coupled with a 835 pF external capacitor with −3 V voltage pulse. (b) Corresponding FFT amplitude spectra of the accompanying current signals for −3 V excitation. Inset shows a current phase–space diagram for the coupled devices. (c) Simulated device currents for oscillators coupled with a 1535 pF external capacitor during excitation with −3 V voltage pulse. (d) FFT amplitude spectra of accompanying current signals for −3 V excitation. Inset shows a current phase space diagram for the coupled devices.

the coupling strength (C_{Ext}=1535 pF). After an initial unsynchronized period of ∼1 μs, the frequency and phase of the two NbO_x oscillators are both completely locked. The synchronized frequency is 6.52 MHz. Fig. 7.13(b) shows voltage flow diagrams in phase space. In contrast to the disordered trajectory for $C_{Ext} \leq 75$ pF and steady state butterfly shaped orbit for $75 \leq C_{Ext} \leq 1035$ pF, a steady state linear shaped orbit is obtained in this synchronized case. The results are consistent with results reported for VO_2 based coupled oscillators [46].

Fig. 7.14 shows the coupling frequency as a function of coupling capacitance for a fixed source voltage of -3.0 V. The coupling interaction can be grouped into 3 regions.

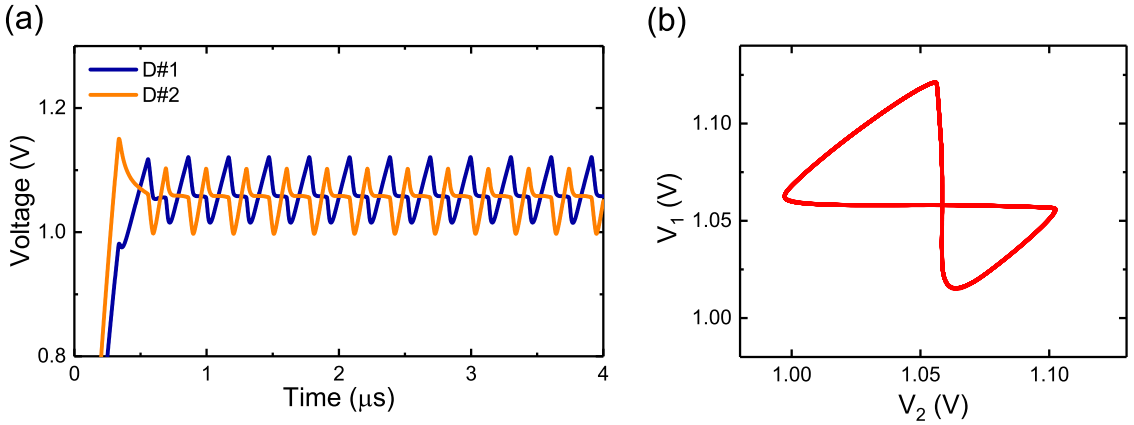

Figure 7.12: (a) The simulated time domain waveform (V_1 and V_2) of the two NbO_x oscillators with a coupling capacitance of 835 pF. (b) Voltage flow diagram in phase space for coupled oscillations. The arrows show the flow direction of the electrical trajectory for the coupled configuration. A steady state butterfly shaped orbit is obtained in the synchronized case.

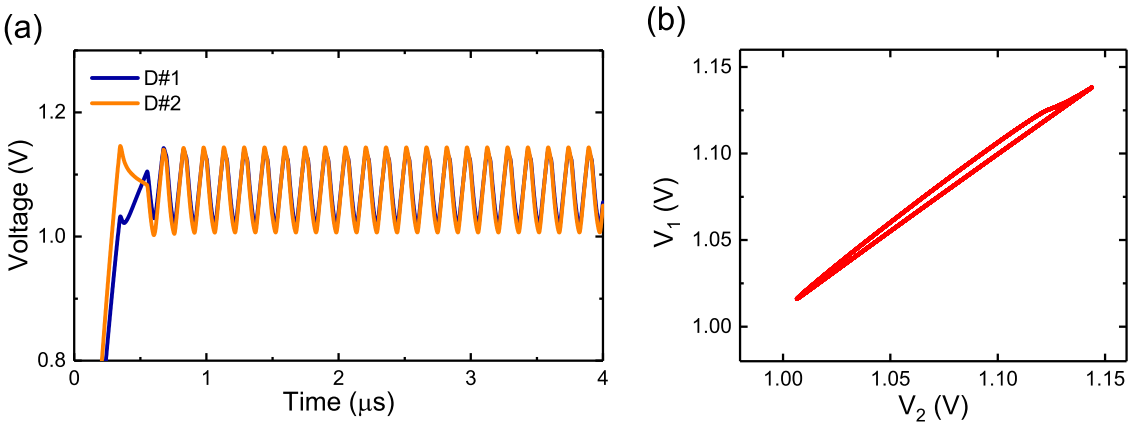

Figure 7.13: (a) The simulated time domain waveform (V_1 and V_2) of the two NbO_x oscillators with a coupling capacitance of 1535 pF. (b) Voltage flow diagram in phase space for coupled oscillations. The arrows show the flow direction of the electrical trajectory for the coupled configuration. The steady state periodic orbit is almost a straight line.

For relative low coupling capacitance region (<75 pF, Region I), the two oscillators are only weakly coupled and oscillate with different frequencies. For coupling capacitance in the middle range ($75 \leq C_{Ext} \leq 1035$ pF, region II), the two oscillators exhibit stable anti-phase coupled oscillations. The two oscillators synchronize and

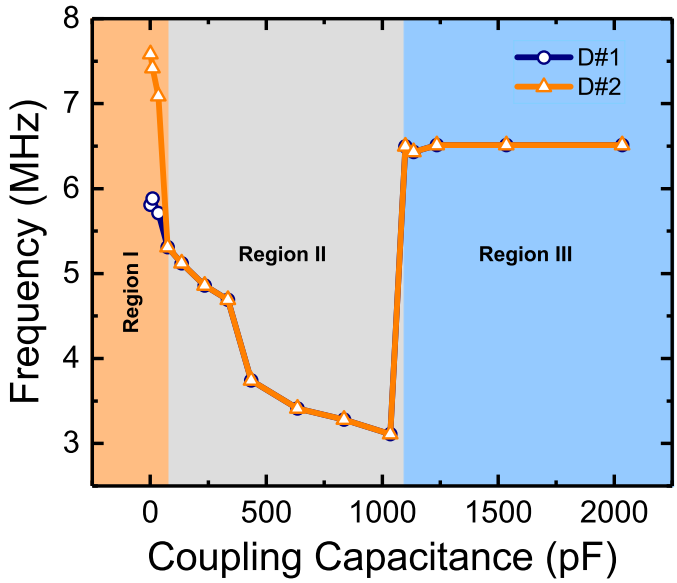

Figure 7.14: The frequencies of V_1 and V_2 nodes for both oscillators change with increasing coupling capacitance (C_{Ext}).

oscillate with a common frequency that decreases with increasing capacitance due to longer charging and discharging cycles. As the capacitance is increased further (>1100 pF, Region III), the coupled oscillators transit to a higher mutual frequency that lies between the natural frequencies of the isolated oscillators. Simulations reveal that the synchronized frequency from the region II and to III exhibits an abrupt increase which is attributed to the increase in coupling capacitance.

7.6 Summary

In summary, we have shown that two non-identical Nb/Nb_2O_5 relaxation oscillators can be capacitively coupled to produce reliable functional devices with high operating frequency, low operating voltage and broad tunability. The coupled system was shown to exhibit rich collective behaviour, from weak coupling with individual device frequencies and phases, to strongly-coupled, synchronised responses, depending on the magnitude of the source voltage and coupling capacitor. Stable frequency

and phase locking states were demonstrated with broad MHz tunable range and low operating voltage. The physical realisation and understanding of such simple coupled oscillatory system are crucial for future development of large-scale coupled oscillatory networks for non-Boolean computing.

Chapter 8

Conclusion and Outlook

8.1 Conclusion and summary

This dissertation has investigated the volatile threshold switching, or current-controlled negative differential resistance (CC-NDR) behaviour, in amorphous NbO_x based metal-insulator-metal (MIM) devices. The thesis began by examining the material properties of NbO_x thin films and then studied the following three areas of interest: 1) threshold switching characteristics and anatomy within a self-assembled threshold-memory structure, 2) suitability of NbO_x threshold switching device as a self-sustained oscillator and corresponding oscillation behaviour, 3) dynamics of capacitively coupled CC-NDR driven oscillators.

In Chapter 3, the physical and electrical properties of NbO_x thin films were studied. Roughness of the sputtered NbO_x samples was found to be relatively smooth and have an exponential dependence on film thickness. The XRD characterisation showed that the film remained amorphous for temperatures up to 500 ^oC and formed pseudohexagonal TT-Nb_2O_5 at 600 ^oC. The composition analysis by RBS showed that an increase in oxygen from 5 % to 12.5 % resulted in a variation in NbO_x composition (O/Nb ratio) from 2.05±0.02 (semiconducting) to 2.87±0.03 (highly insulating). For electrical characterisation, six switching modes in NbO_x were found, including: unipolar resistive switching, bipolar resistive switching, threshold switching, self-assembled threshold-memory switching, co-existence of threshold-memory switching, and co-existence of smooth S-type and abrupt box-like NDRs. Devices with both inert top and bottom electrodes commonly exhibit unipolar resistive

switching while bipolar resistive switching needed to be initiated with a reactive electrode as an oxygen exchange layer.

Chapter 4 focused on understanding the threshold switching behaviour and anatomy of Pt/NbO_x/TiN device structures. The devices exhibited self-assembled threshold-memory switching after a forming process and a subsequent SET/RESET cycle. Symmetric and stable threshold switching was achieved when a compliance current limit was applied. The symmetric threshold switching was studied as a function of device area and NbO_x thickness. The threshold and hold voltages were found to be relatively constant, but the threshold power (current) decreased monotonically with increasing film thickness. The invariant threshold and hold voltages suggested that the threshold switching volume is both laterally and vertically confined at the oxide/electrode interface while the change in threshold power is contributed from a semiconducting shell surrounding the filamentary core. The proposed core/shell structure was supported by the predictions of a resistor network model and detailed numerical modelling. With downscaling device area to the nanoscale, devices exhibited considerable reduction in threshold current and significant improvement in on/off ratio. Localised switching and the core/shell structure were verified by comparison with the threshold switching response between the micro- and nano-scale devices. With increase in ambient temperature, the threshold and hold voltages were reduced while the currents increased. The findings are direct results of lower thermal power required to reach the transition temperature. The temperature and field dependent conduction of the subthreshold region was found to be attributed to the trap-assisted Poole-Frenkel emission.

Chapter 5 experimentally studied the characteristics of a high-frequency electrical oscillation behaviour in NbO_x based threshold switching devices and investigated the suitability of such devices as self-sustained oscillators with reference to a numerical model. Devices are capable of sustaining self-oscillation in a Pearson-Anson circuit configuration within the CC-NDR region. The voltage and load resistance dependent oscillation window and frequency profile can be predicted with the load-

line analysis and the Schmidt model. Three distinct oscillation regimes, sporadic oscillation at the lower boundary, relaxation oscillation, and damped oscillation at the upper boundary, were observed. Oscillators exhibit stable relaxation oscillation for more than $\sim 6.5 \times 10^{10}$ cycles with a minimal source voltage of 1.06 V and a maximum operating temperature up to ~380 K. Temperature dependent measurements showed an increase in oscillation frequency and frequency tunability, and a decrease in peak-to-peak amplitude with rising ambient temperature. The oscillation dynamics were also investigated by finite element modelling in a Pearson-Anson circuit which was able to well describe the oscillation characteristics with inclusion of the circuit and device capacitance. The model underlines the significant effects of the intrinsic and external capacitance on oscillation frequency and peak-to-peak amplitude.

The dynamics of two capacitively coupled CC-NDR driven oscillators were experimentally demonstrated and studied in Chapter 6. The compact and scalable coupled systems were shown to exhibit low power operation and broad MHz tunable range. A diverse range of coupling modes were observed by tuning the source voltage and the coupling capacitance, from weak coupling to strong synchronisation. With a constant coupling capacitance, the coupled oscillators exhibited three coupling regions with increasing source voltage which began with the distinct natural frequency and phase of each oscillator, and then transited to a mutual frequency and phase locking state. The developed finite element model was able to predict and describe the voltage and capacitance dependent nonlinear coupling behaviours.

In summary, the results of these studies have contributed to the advancement of current understanding of threshold switching in amorphous NbO_x thin films. The experimental findings from the systemic device area and thickness study suggested that the localised conduction path consisted of a core/shell structure and was validated with the resistor network model and detailed numerical modelling. We further experimentally demonstrated that the NbO_x based threshold switching devices are promising to be used as scalable and low power self-sustained oscillators with

MHz frequency tunable range, high endurance and high operating temperature tolerance. Finally, the coupled system was physically realised with two NbO_x based CC-NDR driven oscillators and was shown to exhibit rich coupling dynamics which provide a crucial fundamental basis for further development of large-scale coupled networks for non-Boolean computing.

8.2 Future research directions

There are several opportunities for future research:

- The systemic device area and oxide thickness study suggests that the threshold switching occurs in a localised core/shell structure with a fixed threshold switching volume at the oxide/electrode interface. However, direct physical characterisations, including temperature mapping, microstructural analysis and chemical composition, are important to confirm the filamentary nature and examine the oxygen-deficient phases. Evolution of the filament formation process and the threshold switching dynamics can be unravelled by performing in situ current-voltage measurements in horizontally aligned MIM devices with real-time high-resolution transmission electron microscopy imaging. Although direct physical characterisation of the switching process can be complicated and even inconclusive, this type of analysis would be highly important work to pursue.

- The current study has mainly focused on understanding the S-type smooth NDR and its associated self-sustained oscillation behaviour. However, several other NDR responses, including abrupt box-like NDRs, co-existence of smooth S-type and abrupt box-like NDRs, and double S-type smooth NDRs, were also observed during the electrical measurements which demonstrate the switching behaviour in niobium oxide is more complicated. Future systematic study is

needed to unfold the full mechanism, evaluate the NDR stability and understand its implication on oscillation characteristics.

- The oscillation dynamics of single and coupled CC-NDR driven oscillators were addressed with relatively large microscale devices. While the present study is adequate to understand the general behaviour and demonstrate the potential to be used in emerging technologies, it is essential to thoroughly investigate the behaviour in nanoscale devices as higher density and lower power consumption are expected. Device capacitance, leakage current, forming and operating conditions will be changed when device area is scaled down to 10's – 100's nm which is likely to impact the oscillation and coupling responses. Moreover, studies can be extended to investigate alternative coupling methods (e.g. resistor, resistive switching element and transistor), optimise coupling efficiency for two and more devices and examine the implications of device variability and phase noise on coupling response. Further work is clearly required to be carried out in the domain of nanoscale oscillator network.

- From an application perspective, the present study primarily concentrated on understanding the basic properties of NbO_x coupled oscillators for consideration as a fundamental building block in non-Boolean computing application. In the space of brain-inspired computing systems, there are several dynamical systems and hardware implementation designs that can leverage the switching properties in NbO_x and the complex dynamics of such oscillator, including template matching, vertex colouring, Hopfield networks, feed-forward artificial neural network and reservoir computing. Although these computational frameworks all rely on the oscillator-based approach, compatibility, computational efficiency and other specific implementation requirements remain to be explored.

Bibliography

[1] R. Ananthanarayanan, S. K. Esser, H. D. Simon, and D. S. Modha. The cat is out of the bag: cortical simulations with 109 neurons, 1013 synapses. In *Proceedings of the Conference on High Performance Computing Networking, Storage and Analysis*, pages 1–12, Nov 2009.

[2] E.R. Kandel, J.H. Schwartz, and T.M. Jessell. *Principles of neural science*. Elsevier, 1985.

[3] Charles F. Stevens. The neuron. *Scientific American*, 241(3):54–65, 1979.

[4] Daniel E. Feldman. The spike-timing dependence of plasticity. *Neuron*, 75(4):556 – 571, 2012.

[5] Sen Song, Kenneth D. Miller, , and L. F. Abbott. Competitive hebbian learning through spike-timing-dependent synaptic plasticity. *Nat. Neurosci.*, 3:919 – 926, 2000.

[6] Sung Hyun Jo, Ting Chang, Idongesit Ebong, Bhavitavya B. Bhadviya, Pinaki Mazumder, and Wei Lu. Nanoscale memristor device as synapse in neuromorphic systems. *Nano Lett.*, 10(4):1297–1301, 2010.

[7] Duygu Kuzum, Shimeng Yu, and H-S Philip Wong. Synaptic electronics: materials, devices and applications. *Nanotechnology*, 24(38):382001, 2013.

[8] Curtis J. O'Kelly, Heba N. M. Abunahla, Maguy Abi Jaoude, Dirar Homouz, and Baker Mohammad. Subthreshold continuum conductance change in nbo pt memristor interfaces. *J. Phys. Chem. C*, 120(34):18971–18976, 2016.

[9] Kyungah Seo, Insung Kim, Seungjae Jung, Minseok Jo, Sangsu Park, Jubong Park, Jungho Shin, Kuyyadi P Biju, Jaemin Kong, Kwanghee Lee, Byounghun Lee, and Hyunsang Hwang. Analog memory and spike-timing-dependent plasticity characteristics of a nanoscale titanium oxide bilayer resistive switching device. *Nanotechnology*, 22(25):254023, 2011.

[10] Ting Chang, Sung-Hyun Jo, and Wei Lu. Short-term memory to long-term memory transition in a nanoscale memristor. *ACS Nano*, 5(9):7669–7676, 2011.

[11] S. Yu, Y. Wu, R. Jeyasingh, D. Kuzum, and H. S. P. Wong. An electronic synapse device based on metal oxide resistive switching memory for neuromorphic computation. *IEEE Trans. Electron Devices*, 58(8):2729–2737, Aug 2011.

[12] Y. Wu, S. Yu, H. S. P. Wong, Y. S. Chen, H. Y. Lee, S. M. Wang, P. Y. Gu, F. Chen, and M. J. Tsai. Alox-based resistive switching device with gradual resistance modulation for neuromorphic device application. In *2012 4th IEEE International Memory Workshop*, pages 1–4, May 2012.

[13] M. Prezioso, F. Merrikh-Bayat, B. D. Hoskins, G. C. Adam, K. K. Likharev, and D. B. Strukov. Training and operation of an integrated neuromorphic network based on metal-oxide memristors. *Nature*, 521:61–64, 2015.

[14] Alexander Serb, Johannes Bill, Ali Khiat, Radu Berdan, Robert Legenstein, and Themis Prodromakis. Unsupervised learning in probabilistic neural networks with multi-state metal-oxide memristive synapses. *Nat. Commun.*, 7(12611), 2016.

[15] Francisco Bezanilla. Ion channels: From conductance to structure. *Neuron*, 60(3):456 – 468, 2008.

[16] A. L. Hodgkin and A. F. Huxley. A quantitative description of membrane current and its application to conduction and excitation in nerve. *J. Physiol.*, 117(4):500–544, 1952.

[17] H. D. Crane. The neuristor. *IRE Trans. Elect. Comput.*, EC-9(3):370–371, Sept 1960.

[18] M. D. Pickett, G. Medeiros-Ribeiro, and R. S. Williams. A scalable neuristor built with Mott memristors. *Nat. Mater.*, 12:114–117, February 2013.

[19] Leon Chua and Sung Mo Kang. Memristive devices and systems. *Proc. IEEE*, 64(2):209–223, 1976.

[20] Leon Chua. Memristor, hodgkin–huxley, and edge of chaos. *Nanotechnology*, 24(38):383001, 2013.

[21] Leon Chua. Local activity is the origin of complexity. *Int. J. Bifurc. Chaos*, 15(11):3435–3456, 2005.

[22] Leon Chua, Valery Sbitnev, and Hyongsuk Kim. Neurons are poised near the edge of chaos. *Int. J. Bifurc. Chaos*, 22(04):1250098, 2012.

[23] Mainzer Klaus et al. *Local Activity Principle: The Cause Of Complexity And Symmetry Breaking*. World Scientific, 2013.

[24] Juan A. Acebrón, L. L. Bonilla, Conrad J. Pérez Vicente, Félix Ritort, and Renato Spigler. The kuramoto model: A simple paradigm for synchronization phenomena. *Rev. Mod. Phys.*, 77:137–185, Apr 2005.

[25] Wei Zou, D. V. Senthilkumar, Raphael Nagao, Istvan Z. Kiss, Yang Tang, Aneta Koseska, Jinqiao Duan, and Jurgen Kurths. Restoration of rhythmicity in diffusively coupled dynamical networks. *Nat. Commun.*, 6, July 2015.

[26] Arkady Pikovsky, Michael Rosenblum, and Jürgen Kurths. *Synchronization: A Universal Concept in Nonlinear Sciences*. The Cambridge nonlinear science series. Cambridge University Press, Cambridge, 2001.

[27] Pascal Fries. A mechanism for cognitive dynamics: neuronal communication through neuronal coherence. *Trends Cogn. Sci*, 9(10):474–480, 2005.

[28] Juergen Fell and Nikolai Axmacher. The role of phase synchronization in memory processes. *Nat. Rev. Neurosci.*, pages 105–118, 2011.

[29] Alfons Schnitzler and Joachim Gross. Normal and pathological oscillatory communication in the brain. *Nat. Rev. Neurosci*, 6(4):285, 2005.

[30] Andreas K Engel, Pascal Fries, and Wolf Singer. Dynamic predictions: oscillations and synchrony in top–down processing. *Nat. Rev. Neurosci*, 2(10):704, 2001.

[31] Charles M Gray, Peter König, Andreas K Engel, and Wolf Singer. Oscillatory responses in cat visual cortex exhibit inter-columnar synchronization which reflects global stimulus properties. *Nature*, 338(6213):334, 1989.

[32] Pieter R Roelfsema, Andreas K Engel, Peter König, and Wolf Singer. Visuomotor integration is associated with zero time-lag synchronization among cortical areas. *Nature*, 385(6612):157, 1997.

[33] G. Tanaka and K. Aihara. Complex-valued multistate associative memory with nonlinear multilevel functions for gray-level image reconstruction. *IEEE Trans. Neural Netw.*, 20(9):1463–1473, Sept 2009.

[34] F. C. Hoppensteadt and E. M. Izhikevich. Pattern recognition via synchronization in phase-locked loop neural networks. *IEEE Transactions on Neural Networks*, 11(3):734–738, May 2000.

[35] M. J. Cotter, Y. Fang, S. P. Levitan, D. M. Chiarulli, and V. Narayanan. Computational architectures based on coupled oscillators. In *2014 IEEE Computer Society Annual Symposium on VLSI*, pages 130–135, July 2014.

[36] S. Kim, X. Liu, J. Park, S. Jung, W. Lee, J. Woo, J. Shin, G. Choi, C. Cho, S. Park, D. Lee, E. j. Cha, B. H. Lee, H. D. Lee, S. G. Kim, S. Chung, and H. Hwang. Ultrathin (<10nm) Nb_2O_5/NbO_2 hybrid memory with both memory and selector characteristics for high density 3d vertically stackable rram applications. In *2012 Symposium on VLSI Technology (VLSIT)*, pages 155–156, June 2012.

[37] Matthew D Pickett and R Stanley Williams. Sub-100 fJ and sub-nanosecond thermally driven threshold switching in niobium oxide crosspoint nanodevices. *Nanotechnology*, 23(21):215202, 2012.

[38] Matthew Jerry, Abhinav Parihar, Arijit Raychowdhury, and Suman Datta. A random number generator based on insulator-to-metal electronic phase transitions. In *Device Research Conference (DRC), 2017 75th Annual*, pages 1–2, 2017.

[39] A. Ascoli, S. Slesazeck, H. Mähne, R. Tetzlaff, and T. Mikolajick. Nonlinear dynamics of a locally-active memristor. *IEEE Trans. Circuits Syst. I Regul. Pap.*, 62(4):1165–1174, April 2015.

[40] Abhinav Parihar, Nikhil Shukla, Matthew Jerry, Suman Datta, and Arijit Raychowdhury. Vertex coloring of graphs via phase dynamics of coupled oscillatory networks. *Sci. Rep.*, 7(1):911, 2017.

[41] Suhas Kumar, John Paul Strachan, and R. Stanley Williams. Chaotic dynamics in nanoscale NbO_2 mott memristors for analogue computing. *Nature*, 548:318–321, 2017.

[42] Dániel Marx. Graph colouring problems and their applications in scheduling. *Period Polytech Electr Eng*, 48(1-2):11–16, 2004.

[43] John J Hopfield. Neural networks and physical systems with emergent collective computational abilities. *Proc. Natl. Acad. Sci. U.S.A.*, 79(8):2554–2558, 1982.

[44] Zidong Wang, Yurong Liu, Karl Fraser, and Xiaohui Liu. Stochastic stability of uncertain hopfield neural networks with discrete and distributed delays. *Phys. Lett. A*, 354(4):288–297, 2006.

[45] Toshijiro Tanaka and Etsumasa Hiura. Computational abilities of a chaotic neural network. *Phys. Lett. A*, 315(3-4):225–230, 2003.

[46] N. Shukla, A. Parihar, E. Freeman, H. Paik, G. Stone, V. Narayanan, H. Wen, Z. Cai, V. Gopalan, R. Engel-Herbert, D. G. Schlom, A. Raychowdhury, and S. Datta. Synchronized charge oscillations in correlated electron systems. *Sci. Rep.*, 4:4964, May 2014.

[47] Shuai Li, Xinjun Liu, Sanjoy Kumar Nandi, Dinesh Kumar Venkatachalam, and Robert Glen Elliman. Coupling dynamics of Nb/Nb_2O_5 relaxation oscillators. *Nanotechnology*, 28(12):125201, 2017.

[48] Daniele Ielmini and Yuegang Zhang. Analytical model for subthreshold conduction and threshold switching in chalcogenide-based memory devices. *J. Appl. Phys.*, 102(5):054517, 2007.

[49] H. S. P. Wong, S. Raoux, S. Kim, J. Liang, J. P. Reifenberg, B. Rajendran, M. Asheghi, and K. E. Goodson. Phase change memory. *Proc. IEEE*, 98(12):2201–2227, Dec 2010.

[50] Y. Zhou and S. Ramanathan. Mott memory and neuromorphic devices. *Proc. IEEE*, 103(8):1289–1310, Aug 2015.

[51] S. Li, X. Liu, S. K. Nandi, D. K. Venkatachalam, and R. G. Elliman. Temperature dependence of threshold switching in NbO_x thin films. In *2014 Conference on Optoelectronic and Microelectronic Materials Devices*, pages 138–140, Dec 2014.

[52] J. S. Brockman, L. Gao, B. Hughes, C. T. Rettner, M. G. Samant, K. P. Roche, and S. S. P. Parkin. Subnanosecond incubation times for electric-field-induced metallization of a correlated electron oxide. *Nat. Nanotechnol.*, 9:453–458, June 2014.

[53] Zheng Yang, Changhyun Ko, and Shriram Ramanathan. Oxide electronics utilizing ultrafast metal-insulator transitions. *Annu. Rev. Mater. Res.*, 41(1):337–367, 2011.

[54] Leon Chua. Resistance switching memories are memristors. In *Memristor Networks*, pages 21–51. Springer, 2014.

[55] Leon O Chua and Sung Mo Kang. Memristive devices and systems. *Proc. IEEE*, 64(2):209–223, 1976.

[56] F. J. Morin. Oxides which show a metal-to-insulator transition at the neel temperature. *Phys. Rev. Lett.*, 3:34–36, Jul 1959.

[57] DAVID Adler. Mechanisms for metal-nonmental transitions in transition-metal oxides and sulfides. *Rev. Mod. Phys.*, 40:714–736, Oct 1968.

[58] Matthew D. Pickett, Julien Borghetti, J. Joshua Yang, Gilberto Medeiros-Ribeiro, and R. Stanley Williams. Coexistence of memristance and negative differential resistance in a nanoscale metal-oxide-metal system. *Adv. Mater.*, 23(15):1730–1733, 2011.

[59] K. L. Chopra. Avalanche-induced negative resistance in thin oxide films. *J. Appl. Phys.*, 36:184–187, January 1965.

[60] Gary C. Vezzoli. Recovery curve for threshold-switching NbO_2. *J. Appl. Phys.*, 50(10):6390–6395, 1979.

[61] G. Taylor and B. Lalevic. Threshold switching in polycrystalline TiO_2 thin films. *J. Appl. Phys.*, 48(10):4410–4412, 1977.

[62] G Dearnaley, A M Stoneham, and D V Morgan. Electrical phenomena in amorphous oxide films. *Rep. Prog. Phys*, 33(3):1129, 1970.

[63] R G Cope and A W Penn. High-speed solid-state thermal switches based on vanadium dioxide. *J. Phys. D: Appl. Phys.*, 1(2):161, 1968.

[64] C. N. Berglund. Thermal filaments in vanadium dioxide. *IEEE Trans. Electron Dev.*, 16(5):432–437, May 1969.

[65] F. Argall. Switching phenomena in titanium oxide thin films. *Solid-State Electron.*, 11(5):535 – 541, 1968.

[66] Katsuo Seta and Keiji Naito. Calorimetric study of the phase transition in NbO_2. *J. Chem. Thermodyn.*, 14(10):921 – 935, 1982.

[67] V. Eyert. The metal-insulator transition of NbO_2: An embedded peierls instability. *EPL*, 58(6):851, 2002.

[68] R.F. Janninck and D.H. Whitmore. Electrical conductivity and thermoelectric power of niobium dioxide. *J. Phys. Chem. Solids*, 27(6):1183 – 1187, 1966.

[69] Gary A. Gibson, Srinitya Musunuru, Jiaming Zhang, Ken Vandenberghe, James Lee, Cheng-Chih Hsieh, Warren Jackson, Yoocharn Jeon, Dick Henze, Zhiyong Li, and R. Stanley Williams. An accurate locally active memristor model for s-type negative differential resistance in NbO_x. *Appl. Phys. Lett.*, 108(2), 2016.

[70] Ye Zhao, Zhengjun Zhang, and Yuanhua Lin. Optical and dielectric properties of a nanostructured NbO_2 thin film prepared by thermal oxidation. *J. Phys. D: Appl. Phys*, 37(24):3392, 2004.

[71] Y. Wang, R. B. Comes, S. A. Wolf, and J. Lu. Threshold switching characteristics of Nb/NbO_2/TiN vertical devices. *IEEE J. Electron Devices Soc.*, 4(1):11–14, Jan 2016.

[72] Toyanath Joshi, Pavel Borisov, and David Lederman. The role of defects in the electrical properties of NbO_2 thin film vertical devices. *AIP Adv.*, 6(12):125006, 2016.

[73] Fu-Chien Chiu. A review on conduction mechanisms in dielectric films. *Adv. Mater. Sci. Eng.*, 2014.

[74] R. H. Fowler and L. Nordheim. Electron emission in intense electric fields. *Proceedings of the Royal Society of London A: Mathematical, Physical and Engineering Sciences*, 119(781):173–181, 1928.

[75] M. Lenzlinger and E. H. Snow. Fowler-nordheim tunneling into thermally grown SiO_2. *J. Appl. Phys.*, 40(1):278–283, 1969.

[76] Dieter K. Schroder. *Semiconductor Material and Device Characterization*. Wiley-IEEE Press, 2005.

[77] J. G. Simmons. Poole-Frenkel Effect and Schottky Effect in Metal-Insulator-Metal Systems. *Physical Review*, 155:657–660, March 1967.

[78] Tadao Kasuya and Sigenao Koide. A theory of impurity conduction. ii. *J. Phys. Soc. Jpn.*, 13(11):1287–1297, 1958.

[79] Allen Miller and Elihu Abrahams. Impurity conduction at low concentrations. *Phys. Rev.*, 120:745–755, Nov 1960.

[80] N.F. Mott. Conduction in non-crystalline materials. *Philos. Mag*, 19(160):835–852, 1969.

[81] N. F. Mott and E. A. Davis. *Electronic processes in non-crystalline materials*. Oxford University Press, 1979.

[82] A. Rose. Space-charge-limited currents in solids. *Phys. Rev.*, 97:1538–1544, Mar 1955.

[83] Murray A. Lampert. Simplified theory of space-charge-limited currents in an insulator with traps. *Phys. Rev.*, 103:1648–1656, Sep 1956.

[84] N. F. Mott and R. W. Gurney. *Electronic Processes in Ionic Crystals*. Oxford University Press,, 1940.

[85] P. W. Anderson. Absence of diffusion in certain random lattices. *Phys. Rev.*, 109:1492–1505, Mar 1958.

[86] D. Belitz and T. R. Kirkpatrick. The anderson-mott transition. *Rev. Mod. Phys.*, 66:261–380, Apr 1994.

[87] Florian Gebhard. *The Mott Metal-Insulator Transition*. Springer, 1997.

[88] R. E. Peierls. *Quantum theory of solids*. Clarendon Press, 1964.

[89] G. Grüner. The dynamics of charge-density waves. *Rev. Mod. Phys.*, 60:1129–1181, 1988.

[90] N. F. Mott. *Metal-Insulator Transitions*. Taylor & Francis Press, 1990.

[91] N. F. Mott. Metal-insulator transition. *Rev. Mod. Phys.*, 40:677–683, Oct 1968.

[92] Masatoshi Imada, Atsushi Fujimori, and Yoshinori Tokura. Metal-insulator transitions. *Rev. Mod. Phys.*, 70:1039–1263, Oct 1998.

[93] M. Sako, Y. Watanabe, T. Nakajima, J. Sato, K. Muraoka, M. Fujiu, F. Kono, M. Nakagawa, M. Masuda, K. Kato, Y. Terada, Y. Shimizu, M. Honma, A. Imamoto, T. Araya, H. Konno, T. Okanaga, T. Fujimura, X. Wang, M. Muramoto, M. Kamoshida, M. Kohno, Y. Suzuki, T. Hashiguchi, T. Kobayashi, M. Yamaoka, and R. Yamashita. A low power 64 gb mlc nand-flash memory in 15 nm cmos technology. *IEEE J. Solid-State Circuits*, 51(1):196–203, Jan 2016.

[94] J. G. Zhu. Magnetoresistive random access memory: The path to competitiveness and scalability. *Proceedings of the IEEE*, 96(11):1786–1798, Nov 2008.

[95] H. S. P. Wong, H. Y. Lee, S. Yu, Y. S. Chen, Y. Wu, P. S. Chen, B. Lee, F. T. Chen, and M. J. Tsai. Metal-oxide rram. *Proceedings of the IEEE*, 100(6):1951–1970, June 2012.

[96] H-S Philip Wong, Heng-Yuan Lee, Shimeng Yu, Yu-Sheng Chen, Yi Wu, Pang-Shiu Chen, Byoungil Lee, Frederick T Chen, and Ming-Jinn Tsai. Metal-oxide rram. *Proc. IEEE*, 100(6):1951–1970, 2012.

[97] Rainer Waser, Regina Dittmann, Georgi Staikov, and Kristof Szot. Redox-based resistive switching memories–nanoionic mechanisms, prospects, and challenges. *Adv. Mater.*, 21(25-26):2632–2663, 2009.

[98] Akihito Sawa. Resistive switching in transition metal oxides. *Mater. Today*, 11(6):28–36, 2008.

[99] H. Akinaga and H. Shima. Resistive random access memory (ReRAM) based on metal oxides. *Proceedings of the IEEE*, 98(12):2237–2251, Dec 2010.

[100] M. Janousch, G. I. Meijer, U. Staub, B. Delley, S. F. Karg, and B. P. Andreasson. Role of oxygen vacancies in Cr-doped $SrTiO_3$ for resistance-change memory. *Adv. Mater.*, 19(17):2232–2235, 2007.

[101] Gyeong-Su Park, Xiang-Shu Li, Dong-Chirl Kim, Ran-Ju Jung, Myoung-Jae Lee, and Sunae Seo. Observation of electric-field induced ni filament channels in polycrystalline NbO_x film. *Appl. Phys. Lett.*, 91(22):222103, 2007.

[102] D.-H. Kwon, K. M. Kim, J. H. Jang, J. M. Jeon, M. H. Lee, G. H. Kim, X.-S. Li, G.-S. Park, B. Lee, S. Han, M. Kim, and C. S. Hwang. Atomic structure of conducting nanofilaments in TiO_2 resistive switching memory. *Nat. Nanotechnol.*, 5:148–153, February 2010.

[103] B. Gao, J. F. Kang, Y. S. Chen, F. F. Zhang, B. Chen, P. Huang, L. F. Liu, X. Y. Liu, Y. Y. Wang, X. A. Tran, Z. R. Wang, H. Y. Yu, and A. Chin. Oxide-based rram: Unified microscopic principle for both unipolar and bipolar switching. In *2011 International Electron Devices Meeting*, pages 17.4.1–17.4.4, Dec 2011.

[104] Daniele Ielmini and Rainer Waser. *Resistive switching: from fundamentals of nanoionic redox processes to memristive device applications*. John Wiley & Sons, 2015.

[105] U. Russo, D. Ielmini, C. Cagli, and A. L. Lacaita. Self-accelerated thermal dissolution model for reset programming in unipolar resistive-switching memory (RRAM) devices. *IEEE Trans. Electron Devices*, 56(2):193–200, Feb 2009.

[106] D. Ielmini. Modeling the universal set/reset characteristics of bipolar rram by field- and temperature-driven filament growth. *IEEE Trans. Electron Devices*, 58(12):4309–4317, Dec 2011.

[107] A. L. Bowman, T. C. Wallace, J. L. Yarnell, and R. G. Wenzel. The crystal structure of niobium monoxide. *Acta Cryst.*, 21(5):843, Nov 1966.

[108] T. B. Reed and E. R. Pollard. The crystal structure of niobium monoxide. *Inorg. Synth.*, 21(5):843, Nov 1966.

[109] Jeremy K. Burdett and Timothy Hughbanks. Niobium oxide (NbO) and titanium oxide (TiO): a study of the structural and electronic stability of structures derived from rock salt. *J. Am. Chem. Soc*, 106(11):3101–3113, 1984.

[110] W. W. Schulz and R. M. Wentzcovitch. Electronic band structure and bonding in Nb_3O_3. *Phys. Rev. B*, 48:16986–16991, December 1993.

[111] Jr. Pollard, E. R. Electronic properties of niobium monoxide. *Massachusetts Institute of Technology: Cambridge, MA*, 1968.

[112] A. K. Cheetham and C. N. R. Rao. A neutron diffraction study of niobium dioxide. *Acta Crystallogr. Sect. B*, 32(5):1579–1580, May 1976.

[113] R.F. Janninck and D.H. Whitmore. Electrical conductivity and thermoelectric power of niobium dioxide. *J. Phys. Chem. Solids*, 27(6):1183 – 1187, 1966.

[114] S. H. Shin, T. Halpern, and P. M. Raccah. High-speed high-current field switching of NbO_2. *J. Appl. Phys.*, 48(7):3150–3153, 1977.

[115] J.M. Gallego and C.B. Thomas. Phase transitions in films of niobium dioxide. *Solid State Commun.*, 43(7):547 – 549, 1982.

[116] Gary C. Vezzoli. Recovery curve for threshold-switching NbO_2 . *J. Appl. Phys.*, 50(10):6390–6395, 1979.

[117] T. Sakata, K. Sakata, and I. Nishida. Study of phase transition in NbO_2. *Phys. Status Solidi B*, 20(2):K155–K157, 1967.

[118] Harald Schäfer, R. Gruehn, and F. Schulte. The modifications of niobium pentoxide. *Angew. Chem. Int. Ed.*, 5(1):40–52, 1966.

[119] Hiroshi Kodama, Takeshi Kikuchi, and Masaru Goto. Relative stabilities of several forms of niobium pentoxide. *J. Less-Common Met.*, 29(4):415–421, 1972.

[120] B. M. Gatehouse and A. D. Wadsley. The crystal structure of the high temperature form of niobium pentoxide. *Acta Cryst.*, 17(12):1545–1554, Dec 1964.

[121] Rozina Abdul Rani, Ahmad Sabirin Zoolfakar, Anthony P. O'Mullane, Michael W. Austin, and Kourosh Kalantar-Zadeh. Thin films and nanostructures of niobium pentoxide: fundamental properties, synthesis methods and applications. *J. Mater. Chem. A*, 2:15683–15703, 2014.

[122] J. Niebuhr. Die niederen oxide des niobs. *J. Less-Common Met.*, 11(3):191 – 203, 1966.

[123] M. Grundner and J. Halbritter. Xps and aes studies on oxide growth and oxide coatings on niobium. *J. Appl. Phys.*, 51(1):397–405, 1980.

[124] S. Andersson and A. D. Wadsley. Crystallographic Shear and Diffusion Paths in Certain Higher Oxides of Niobium, Tungsten, Molybdenum and Titanium. *Nature*, 211:581–583, August 1966.

[125] A.Ann McConnell, J.S. Aderson, and C.N.R. Rao. Raman spectra of niobium oxides. *Spectrochim. Acta Mol. Spectrosc.*, 32(5):1067 – 1076, 1976.

[126] J. Halbritter. On the oxidation and on the superconductivity of niobium. *Appl. Phys. A*, 43:1–28, May 1987.

[127] B. Meyer and R. Gruehn. Umwandlungs- und reduktionsprodukte von metastabilem Nb_2O_5, elektronenoptische untersuchung. *J. Less-Common Met.*, 83(2):185 – 203, 1982.

[128] E. S. Crawford and J. S. Anderson. Homogeneous solid state transformations in niobium oxides. *Phil. Trans. R. Soc. A*, 304(1485):327–364, 1982.

[129] R.P. Elliott. Columbium–oxygen system. *Trans. Am. Soc. Met.*, 54:990–1014, 1960.

[130] John T. Harding. Density of niobium. *J. Appl. Phys.*, 37(2):928–928, 1966.

[131] R.P. Tye. Preliminary measurements on the thermal and electrical conductivities of molybdenum, niobium, tantalum and tungsten. *J. Less-Common Met.*, 3(1):13 – 18, 1961.

[132] N Morton, B W James, G H Wostenholm, and R J Nichols. The electrical resistivity of niobium and niobium-zirconium alloys. *J. Phys. F: Met. Phys.*, 5(1):85, 1975.

[133] A.T. Wu. Investigation of oxide layer structure on niobium surface using a secondary ion mass spectrometry. *Physica C*, 441(1):79 – 82, 2006. Proceedings of the 12th International Workshop on RF Superconductivity.

[134] K.J.S. Sokhey, S.K. Rai, and G.S. Lodha. Oxidation studies of niobium thin films at room temperature by x-ray reflectivity. *Appl. Surf. Sci.*, 257(1):222 – 226, 2010.

[135] J. K. Hulm, C. K. Jones, R. A. Hein, and J. W. Gibson. Superconductivity in the TiO and NbO systems. *JJ. Low Temp. Phys*, 7(3):291–307, May 1972.

[136] W. Gao, J. F. Conley Jr., and Y. Ono. NbO as gate electrode for n-channel metal-oxide-semiconductor field-effect-transistors. *Appl. Phys. Lett.*, 84(23):4666–4668, 2004.

[137] J.M. Gallego and C.B. Thomas. Preparation and characterization of thin films of NbO_2. *Thin Solid Films*, 98(1):11 – 22, 1982.

[138] J.M. Gallego and C.B. Thomas. The conductivity at high fields in films of amorphous niobium dioxide. *Solid State Commun.*, 47(6):419 – 422, 1983.

[139] M.W.G. Snook, C.B. Thomas, and H.S. Reehal. Preparation of polycrystalline films of NbO_2 by rf sputtering. *Materials Letters*, 3(11):462 – 466, 1985.

[140] D. L. Perry. *Handbook of Inorganic Compounds*. CRC Press, 2011.

[141] D. Adler. Mechanisms for Metal-Nonmental Transitions in Transition-Metal Oxides and Sulfides. *Rev. Mod. Phys*, 40:714–736, October 1968.

[142] S.H. Shin, T.H. Halpern, and P.M. Raccah. Crystal growth and study of the stoichiometry of nbo2. *Mats. Res. Bull.*, 10(10):1061 – 1065, 1975.

[143] J. C. Lee and W. W. Durand. Electrically stimulated optical switching of NbO_2 thin films. *J. Appl. Phys.*, 56(11):3350–3352, 1984.

[144] Shuai Li, Xinjun Liu, Sanjoy Kumar Nandi, Dinesh Kumar Venkatachalam, and Robert Glen Elliman. High-endurance megahertz electrical self-oscillation in Ti/NbO_x bilayer structures. *Appl. Phys. Lett.*, 106(21):212902, 2015.

[145] K. T. Jacob, Chander Shekhar, M. Vinay, and Yoshio Waseda. Thermodynamic properties of niobium oxides. *J. Chem. Eng. Data*, 55(11):4854–4863, 2010.

[146] Roberta Brayner and Francois Bozon-Verduraz. Niobium pentoxide prepared by soft chemical routes: morphology, structure, defects and quantum size effect. *Phys. Chem. Chem. Phys.*, 5:1457–1466, 2003.

[147] E.Z Kurmaev, A Moewes, O.G Bureev, I.A Nekrasov, V.M Cherkashenko, M.A Korotin, and D.L Ederer. Electronic structure of niobium oxides. *J Alloys Compd.*, 347(1):213 – 218, 2002.

[148] S. Venkataraj, R. Drese, Ch. Liesch, O. Kappertz, R. Jayavel, and M. Wuttig. Temperature stability of sputtered niobium–oxide films. *J. Appl. Phys.*, 91(8):4863–4871, 2002.

[149] I.P. Zibrov, V.P. Filonenko, P.-E. Werner, B.-O. Marinder, and M. Sundberg. A new high-pressure modification of Nb_2O_5. *J. Solid State Chem.*, 141(1):205 – 211, 1998.

[150] M. Guenin, R. Frety, E. Garbowski, and P. Vergnon. Characterization of niobium pentoxide prepared by flame reaction. *J. Mater. Sci.*, 23:1009–1013, March 1988.

[151] V. Fischer, H. Stormer, D. Gerthsen, M. Stenzel, H. Zillgen, and E. Ivers-Tiffee. Niobium as new material for electrolyte capacitors with nanoscale dielectric oxide layers. In *Proceedings of the 7th International Conference on Properties and Applications of Dielectric Materials (Cat. No.03CH37417)*, volume 3, pages 1134–1137, June 2003.

[152] G. E. Cavigliasso, M. J. Esplandiu, and V. A. Macagno. Influence of the forming electrolyte on the electrical properties of tantalum and niobium oxide films: an eis comparative study. *J. Appl. Electrochem.*, 28(11):1213–1219, Nov 1998.

[153] M Maček and B Orel. Electrochromism of sol-gel derived niobium oxide films. *Sol. Energy Mater. Sol. Cells*, 54(1):121 – 130, 1998.

[154] M.R.N. Soares, S. Leite, C. Nico, M. Peres, A.J.S. Fernandes, M.P.F. Graça, M. Matos, R. Monteiro, T. Monteiro, and F.M. Costa. Effect of processing method on physical properties of Nb_2O_5. *J. Eur. Ceram. Soc.*, 31(4):501 – 506, 2011.

[155] M.P.F. Graça, A. Meireles, C. Nico, and M.A. Valente. Nb_2O_5 nanosize powders prepared by sol-gel structure, morphology and dielectric properties. *J. Alloys Compd.*, 553:177 – 182, 2013.

[156] A Kohli, C.C Wang, and S.A Akbar. Niobium pentoxide as a lean-range oxygen sensor. *Sens. Actuator B-Chem.*, 56(1):121 – 128, 1999.

[157] Hyunhee Baek, Chanwoo Lee, Jungkyu Choi, and Jinhan Cho. Nonvolatile memory devices prepared from sol–gel derived niobium pentoxide films. *Langmuir*, 29(1):380–386, 2013.

[158] Dongchang Chen, Jeng-Han Wang, Tsung-Fu Chou, Bote Zhao, Mostafa A. El-Sayed, and Meilin Liu. Unraveling the nature of anomalously fast energy storage in T-Nb_2O_5. *J. Am. Chem. Soc.*, 139(20):7071–7081, 2017.

[159] W. R. Hiatt and T. W. Hickmott. Bistable switching in niobium oxide diodes. *Appl. Phys. Lett.*, 6(6):106–108, 1965.

[160] T. W. Hickmott and W. R. Hiatt. Electrode effects and bistable switching of amorphous Nb_2O_5 diodes. *Solid-State Electron*, 13:1033, July 1970.

[161] N. Fuschillo, B. Lalevic, N.K. Annamalai, and W. Slusark. Switching phenomena and dielectric breakdown in amorphous Nb_2O_5 films. *J. Non-Cryst. Solids*, 22(1):159 – 172, 1976.

[162] B. Lalevic and W. Slusark. Switching processes and dielectric breakdown in polycrystalline Nb_2O_5 films. *J. Electron. Mater.*, 5(5):531–551, Oct 1976.

[163] T. Mikolajick, H. Wylezich, H. Maehne, S. Slesazeck, and T. Mikolajick. Versatile resistive switching in niobium oxide. In *2016 IEEE International Symposium on Circuits and Systems (ISCAS)*, pages 381–384, May 2016.

[164] F. Hanzig, H. Mähne, J. Veselý, H. Wylezich, S. Slesazeck, A. Leuteritz, M. Zschornak, M. Motylenko, V. Klemm, T. Mikolajick, and D. Rafaja. Effect of the stoichiometry of niobium oxide on the resistive switching of Nb_2O_5 based metal-insulator-metal stacks. *J. Electron. Spectrosc. Relat. Phenom.*, 202:122 – 127, 2015.

[165] Jieun Bae, Inrok Hwang, Yuhyun Jeong, Sung-Oong Kang, Sahwan Hong, Jongwan Son, Jinsik Choi, Jinsoo Kim, June Park, Maeng-Je Seong, Quanxi Jia, and Bae Ho Park. Coexistence of bi-stable memory and mono-stable threshold resistance switching phenomena in amorphous nbox films. *Appl. Phys. Lett.*, 100(6):062902, 2012.

[166] Kyooho Jung, Yongmin Kim, Woong Jung, Hyunsik Im, Baeho Park, Jinpyo Hong, Jiyeong Lee, Jongku Park, and Jeon-Kook Lee. Electrically induced conducting nanochannels in an amorphous resistive switching niobium oxide film. *Appl. Phys. Lett.*, 97(23):233509, 2010.

[167] D. V. Geppert. A new negative-resistance device. *Proceedings of the IEEE*, 51(1):223–223, Jan 1963.

[168] Andrew O'Hara, Timothy N. Nunley, Agham B. Posadas, Stefan Zollner, and Alexander A. Demkov. Electronic and optical properties of NbO_2. *J. Appl. Phys.*, 116(21):213705, 2014.

[169] David Lindley. Atomic vibrations stabilize metallic vanadium dioxide, 2015.

[170] Suhas Kumar, Ziwen Wang, Noraica Davila, Niru Kumari, Kate J. Norris, Xiaopeng Huang, David Strachan, John Paul amd Vine, A. L. David Kilcoyne, Yoshio Nishi, and R. Stanley Williams. Physical origins of current and temperature controlled negative differential resistances in NbO_2. *Nat. Commun.*, 8:658, 2017.

[171] G. C. Vezzoli, S. Levy, B. Lalevic, and M. Shoga. Threshold switching polycrystalline NbO_2: Decay and recovery of the on state at room and low temperatures and its relationship to trapping centers. *J. Appl. Phys.*, 54:5828–5838, 1983.

[172] S. Slesazeck, H. Mahne, H. Wylezich, A. Wachowiak, J. Radhakrishnan, A. Ascoli, R. Tetzlaff, and T. Mikolajick. Physical model of threshold switching in nbo2 based memristors. *RSC Adv.*, 5:102318–102322, 2015.

[173] Carsten Funck, Stephan Menzel, Nabeel Aslam, Hehe Zhang, Alexander Hardtdegen, Rainer Waser, and Susanne Hoffmann-Eifert. Multidimensional simulation of threshold switching in NbO_2 based on an electric field triggered thermal runaway model. *Adv. Electron. Mater.*, 2(7):1600169, 2016.

[174] Yong Wook Lee, Bong-Jun Kim, Jung-Wook Lim, Sun Jin Yun, Sungyoul Choi, Byung-Gyu Chae, Gyoungock Kim, and Hyun-Tak Kim. Metal-insulator transition-induced electrical oscillation in vanadium dioxide thin film. *Appl. Phys. Lett*, 92(16):162903, 2008.

[175] Md. Suruz Mian, Kunio Okimura, and Joe Sakai. Self-oscillation up to 9 mhz based on voltage triggered switching in VO_2/TiN point contact junctions. *J. Appl. Phys.*, 117(21):215305, 2015.

[176] A. A. Sharma, Y. Li, M. Skowronski, J. A. Bain, and J. A. Weldon. High-frequency TaO_x-based compact oscillators. *IEEE Transactions on Electron Devices*, 62(11):3857–3862, Nov 2015.

[177] Tom Driscoll, Jack Quinn, Massimiliano Di Ventra, Dimitri N Basov, Giwan Seo, Yong-Wook Lee, Hyun-Tak Kim, and David R Smith. Current oscillations in vanadium dioxide: Evidence for electrically triggered percolation avalanches. *Phys. Rev. B*, 86(9):094203, 2012.

[178] Joe Sakai. High-efficiency voltage oscillation in VO_2 planer-type junctions with infinite negative differential resistance. *J. Appl. Phys.*, 103(10):103708, 2008.

[179] You Zhou, Xiaonan Chen, Changhyun Ko, Zheng Yang, Chandra Mouli, and Shriram Ramanathan. Voltage-triggered ultrafast phase transition in vanadium dioxide switches. *IEEE Electron Device Lett.*, 34(2):220–222, 2013.

[180] Ligang Gao, Pai-Yu Chen, and Shimeng Yu. NbO_x based oscillation neuron for neuromorphic computing. *Appl. Phys. Lett.*, 111(10):103503, 2017.

[181] A. Beaumont, J. Leroy, J.-C. Orlianges, and A. Crunteanu. Current-induced electrical self-oscillations across out-of-plane threshold switches based on VO_2 layers integrated in crossbars geometry. *J. Appl. Phys.*, 115(15):154502, 2014.

[182] Jonathan Leroy, Aurelian Crunteanu, Julien Givernaud, Jean-Christophe Orlianges, Corinne Champeaux, and Pierre Blondy. Generation of electrical self-oscillations in two-terminal switching devices based on the insulator-to-metal phase transition of VO_2 thin films. *Int. J. Microwave Wireless Technol.*, 4(1):101–107, 2012.

[183] Hyun-Tak Kim, Bong-Jun Kim, Sungyoul Choi, Byung-Gyu Chae, Yong Wook Lee, T. Driscoll, M. M. Qazilbash, and D. N. Basov. Electrical oscillations induced by the metal-insulator transition in VO_2. *J. Appl. Phys.*, 107(2):023702, 2010.

[184] Frank C. Hoppensteadt and Eugene M. Izhikevich. Oscillatory neurocomputers with dynamic connectivity. *Phys. Rev. Lett.*, 82:2983–2986, Apr 1999.

[185] Abhinav Parihar, Nikhil Shukla, Suman Datta, and Arijit Raychowdhury. Synchronization of pairwise-coupled, identical, relaxation oscillators based on metal-insulator phase transition devices: A model study. *J. Appl. Phys.*, 117(5):054902, 2015.

[186] S. Datta, N. Shukla, M. Cotter, A. Parihar, and A. Raychowdhury. Neuro inspired computing with coupled relaxation oscillators. In *2014 51st ACM/EDAC/IEEE Design Automation Conference (DAC)*, pages 1–6, June 2014.

[187] Xinjun Liu, Shuai Li, Sanjoy Kumar Nandi, Dinesh Kumar Venkatachalam, and Robert Glen Elliman. Threshold switching and electrical self-oscillation in niobium oxide films. *J. Appl. Phys.*, 120(12):124102, 2016.

[188] Lawrence R Doolittle. A semiautomatic algorithm for rutherford backscattering analysis. *Nucl. Inst. Meth. B*, 15(1-6):227–231, 1986.

[189] Sanjoy Kumar Nandi, Xinjun Liu, Dinesh Kumar Venkatachalam, and Robert Glen Elliman. Effect of electrode roughness on electroforming in HfO_2

and defect-induced moderation of electric-field enhancement. *Phys. Rev. Applied*, 4(6):064010, 2015.

[190] A. Kawahara, R. Azuma, Y. Ikeda, K. Kawai, Y. Katoh, Y. Hayakawa, K. Tsuji, S. Yoneda, A. Himeno, K. Shimakawa, T. Takagi, T. Mikawa, and K. Aono. An 8 mb multi-layered cross-point reram macro with 443 mb/s write throughput. *IEEE J. Solid-State Circuits*, 48(1):178–185, Jan 2013.

[191] J. Joshua Yang, Dmitri B. Strukov, and Duncan R. Stewart. Memristive devices for computing. *Nat. Nanotechnol.*, 8:13 – 24, 2013.

[192] E. Linn, R. Rosezin, C. Kugeler, and R. Waser. Complementary resistive switches for passive nanocrossbar memories. *Nature Mater.*, 9, March 2010.

[193] Dimin Niu, Cong Xu, Naveen Muralimanohar, Norman P. Jouppi, and Yuan Xie. Design trade-offs for high density cross-point resistive memory. In *Proceedings of the 2012 ACM/IEEE International Symposium on Low Power Electronics and Design*, ISLPED '12, pages 209–214, 2012.

[194] J. Zhou, K. H. Kim, and W. Lu. Crossbar rram arrays: Selector device requirements during read operation. *IEEE Electron Device Lett.*, 61(5):1369–1376, May 2014.

[195] Sanjoy Kumar Nandi, Xinjun Liu, Dinesh Kumar Venkatachalam, and Robert Glen Elliman. Self-assembly of an NbO_2 interlayer and configurable resistive switching in Pt/Nb/HfO_2/Pt structures. *Appl. Phys. Lett.*, 107(13):132901, 2015.

[196] Xinjun Liu, Sharif Md Sadaf, Myungwoo Son, Jungho Shin, Jubong Park, Joonmyoung Lee, Sangsu Park, and Hyunsang Hwang. Diode-less bilayer oxide (WO_x–NbO_x) device for cross-point resistive memory applications. *Nanotechnology*, 22(47):475702, 2011.

[197] M. Son, J. Lee, J. Park, J. Shin, G. Choi, S. Jung, W. Lee, S. Kim, S. Park, and H. Hwang. Excellent selector characteristics of nanoscale VO_2 for high-density bipolar reram applications. *IEEE Electron Device Lett.*, 32(11):1579–1581, Nov 2011.

[198] Sanjoy Kumar Nandi, Xinjun Liu, Dinesh Kumar Venkatachalam, and Robert Glen Elliman. Threshold current reduction for the metal–insulator transition in NbO_{2-x}-selector devices: the effect of reram integration. *J. Phys. D: Appl. Phys.*, 48(19):195105, 2015.

[199] Euijun Cha, Jaehyuk Park, Jiyong Woo, Daeseok Lee, Amit Prakash, and Hyunsang Hwang. Comprehensive scaling study of NbO_2 insulator-metal-transition selector for cross point array application. *Appl. Phys. Lett.*, 108(15):153502, 2016.

[200] Xiang Yuan Li, Xing Long Shao, Yi Chuan Wang, Hao Jiang, Cheol Seong Hwang, and Jin Shi Zhao. Thin TiO_x layer as a voltage divider layer located at the quasi-ohmic junction in the $Pt/Ta_2O_5/Ta$ resistance switching memory. *Nanoscale*, 9:2358–2368, 2017.

[201] Y. Lu, B. Gao, Y. Fu, B. Chen, L. Liu, X. Liu, and J. Kang. A simplified model for resistive switching of oxide-based resistive random access memory devices. *IEEE Electron Device Lett.*, 33(3):306–308, March 2012.

[202] X. Liu, S. K. Nandi, D. K. Venkatachalam, K. Belay, S. Song, and R. G. Elliman. Reduced threshold current in NbO_2 selector by engineering device structure. *IEEE Electron Device Lett.*, 35(10):1055–1057, Oct 2014.

[203] Sieu D. Ha, Jian Shi, Yasmine Meroz, L. Mahadevan, and Shriram Ramanathan. Neuromimetic circuits with synaptic devices based on strongly correlated electron systems. *Phys. Rev. Applied*, 2:064003, Dec 2014.

[204] T. C. Jackson, A. A. Sharma, J. A. Bain, J. A. Weldon, and L. Pileggi. Oscillatory neural networks based on tmo nano-oscillators and multi-level rram cells. *IEEE Trans. Emerg. Sel. Topics Circuits Syst.*, 5(2):230–241, June 2015.

[205] Sanjoy Kumar Nandi, Shuai Li, Xinjun Liu, and Robert G Elliman. Temperature dependent frequency tuning of NbO_x relaxation oscillators. *Appl. Phys. Lett.*, 111(20):202901, 2017.

[206] K. L. Chopra. Current-controlled negative resistance in thin niobium oxide films. *Proceedings of the IEEE*, 51(6):941–942, June 1963.

[207] B. Lalevic and M. Shoga. Relaxation oscillations in NbO_2 thin film switching devices. *Thin Solid Films*, 75(2):199 – 204, 1981.

[208] X. Liu, S. Md. Sadaf, M. Son, J. Park, J. Shin, W. Lee, K. Seo, D. Lee, and H. Hwang. Co-occurrence of threshold switching and memory switching in $Pt/NbO_x/Pt$ cells for crosspoint memory applications. *IEEE Electron Device Letters*, 33(2):236–238, Feb 2012.

[209] Y. Wang, R. B. Comes, S. A. Wolf, and J. Lu. Threshold switching characteristics of $Nb/NbO_2/TiN$ vertical devices. *IEEE Journal of the Electron Devices Society*, 4(1):11–14, Jan 2016.

[210] M. Vos, X. Liu, P.L. Grande, S.K. Nandi, D.K. Venkatachalam, and R.G. Elliman. The use of electron rutherford backscattering to characterize novel electronic materials as illustrated by a case study of sputter-deposited NbO_x films. *Nucl. Instrum. Methods Phys. Res., Sect. B*, 340:58 – 62, 2014.

[211] S O Pearson and H St G Anson. The neon tube as a means of producing intermittent currents. *Proceedings of the Physical Society of London*, 34(1):204, 1921.

[212] Pierre E. Schmidt and Roberto C. Callarotti. Theoretical and experimental study of the operation of ovonic switches in the relaxation oscillation mode.

i. the charging characteristic during the off state. *J. Appl. Phys.*, 55(8):3144–3147, 1984.

[213] A. Zimmers, L. Aigouy, M. Mortier, A. Sharoni, Siming Wang, K. G. West, J. G. Ramirez, and Ivan K. Schuller. Role of thermal heating on the voltage induced insulator-metal transition in VO_2. *Phys. Rev. Lett.*, 110:056601, Jan 2013.

[214] A.L. Pergament, P.P. Boriskov, A.A. Velichko, and N.A. Kuldin. Switching effect and the metal–insulator transition in electric field. *J. Phys. Chem. Solids*, 71(6):874 – 879, 2010.

[215] B. J. Kim, G. Seo, Y. W. Lee, S. Choi, and H. T. Kim. Linear characteristics of a metal-insulator transition voltage and oscillation frequency in VO_2 devices. *IEEE Electron Device Letters*, 31(11):1314–1316, Nov 2010.

[216] C. Hermes, M. Wimmer, S. Menzel, K. Fleck, G. Bruns, M. Salinga, U. Bottger, R. Bruchhaus, T. Schmitz-Kempen, M. Wuttig, and R. Waser. Analysis of transient currents during ultrafast switching of TiO_2 nanocrossbar devices. *IEEE Electron Device Lett.*, 32(8):1116–1118, Aug 2011.

[217] X. Liu, S. K. Nandi, D. K. Venkatachalam, S. Li, K. Belay, and R. G. Elliman. Finite element modeling of resistive switching in Nb_2O_5-based memory device. In *2014 Conference on Optoelectronic and Microelectronic Materials Devices*, pages 280–282, Dec 2014.

[218] Suhas Kumar, Matthew D. Pickett, John Paul Strachan, Gary Gibson, Yoshio Nishi, and R. Stanley Williams. Local temperature redistribution and structural transition during joule-heating-driven conductance switching in VO_2. *Adv. Mater.*, 25(42):6128–6132, 2013.

[219] Helge Wylezich, Hannes Mähne, Jura Rensberg, Carsten Ronning, Peter Zahn, Stefan Slesazeck, and Thomas Mikolajick. Local ion irradiation-induced resist-

ive threshold and memory switching in Nb_2O_5/NbO_x films. *ACS Appl. Mater. Interfaces*, 6(20):17474–17480, 2014.

[220] Qian Gu, Abram Falk, Junqiao Wu, Lian Ouyang, and Hongkun Park. Current-driven phase oscillation and domain-wall propagation in $W_xV_{1-x}O_2$ nanobeams. *Nano Lett.*, 7(2):363–366, 2007.

[221] S. Lavizzari, D. Ielmini, and A. L. Lacaita. A new transient model for recovery and relaxation oscillations in phase-change memories. *IEEE Trans. Electron Devices*, 57(8):1838–1845, Aug 2010.

[222] A. Cywar, F. Dirisaglik, M. Akbulut, G. Bakan, S. Steen, H. Silva, and A. Gokirmak. Scaling of silicon phase-change oscillators. *IEEE Electron Device Lett.*, 32(11):1486–1488, Nov 2011.

[223] Juan A. Acebrón, L. L. Bonilla, Conrad J. Pérez Vicente, Félix Ritort, and Renato Spigler. The kuramoto model: A simple paradigm for synchronization phenomena. *Rev. Mod. Phys.*, 77:137–185, Apr 2005.

[224] Arkady Pikovsky, Michael Rosenblum, and Jürgen Kurths. *Synchronization: A Universal Concept in Nonlinear Sciences*. The Cambridge nonlinear science series. Cambridge University Press, Cambridge, 2001.

[225] Arthur T. Winfree. Biological rhythms and the behavior of populations of coupled oscillators. *J. Theor. Biol.*, 16(1):15 – 42, 1967.

[226] Robert C. Elson, Allen I. Selverston, Ramon Huerta, Nikolai F. Rulkov, Mikhail I. Rabinovich, and Henry D. I. Abarbanel. Synchronous behavior of two coupled biological neurons. *Phys. Rev. Lett.*, 81:5692–5695, Dec 1998.

[227] Steven H. Strogatz. Human sleep and circadian rhythms: a simple model based on two coupled oscillators. *J. Math. Biol.*, 25(3):327–347, 1987.

[228] Charles M. Gray. Synchronous oscillations in neuronal systems: Mechanisms and functions. *J. Comput. Neurosci.*, 1(1):11–38, 1994.

[229] Mian Zhang, Gustavo S. Wiederhecker, Sasikanth Manipatruni, Arthur Barnard, Paul McEuen, and Michal Lipson. Synchronization of micromechanical oscillators using light. *Phys. Rev. Lett.*, 109:233906, Dec 2012.

[230] N. Locatelli, V. Cros, and J. Grollier. Spin-torque building blocks. *Nat. Mater.*, 13:11–20, 2014.

[231] S. P. Levitan, Y. Fang, D. H. Dash, T. Shibata, D. E. Nikonov, and G. I. Bourianoff. Non-boolean associative architectures based on nano-oscillators. In *2012 13th International Workshop on Cellular Nanoscale Networks and their Applications*, pages 1–6, Aug 2012.

[232] Hyungkwang Lim, Hyung-Woo Ahn, Vladimir Kornijcuk, Guhyun Kim, Jun Yeong Seok, Inho Kim, Cheol Seong Hwang, and Doo Seok Jeong. Relaxation oscillator-realized artificial electronic neurons, their responses, and noise. *Nanoscale*, 8:9629–9640, 2016.

[233] S. Kaka, M. R. Pufall, W. H. Rippard, T. J. Silva, S. E. Russek, and J. A. Katine. Mutual phase-locking of microwave spin torque nano-oscillators. *Nature*, 437:389–392, September 2005.